UNIVERSITÀ DEGLI STUDI DI TRIESTE

XXX CICLO DEL DOTTORATO DI RICERCA IN INGEGNERIA E ARCHITETTURA

THE FERMI FREE ELECTRON LASER: A HIGH GRADIENT SOLUTION FOR INCREASING THE LINEAR ACCELERATOR ENERGY

Settore scientifico-disciplinare: ING-INF/02

DOTTORANDO
CLAUDIO SERPICO

COORDINATORE
PROF. DIEGO MICHELI

SUPERVISORE DI TESI
PROF. ROBERTO VESCOVO

ANNO ACCADEMICO 2016-2017

II

THE FERMI FREE ELECTRON LASER: A HIGH GRADIENT SOLUTION FOR INCREASING THE LINEAR ACCELERATOR ENERGY

Claudio Serpico

December 16, 2017

II

Acknowledgements

I would like to thank Prof. R. Vescovo for the great opportunity of this Ph.D., and for his effort in supervising my work.

I am in debt with Dr. Alexej Grudiev, at CERN: it has been a privilege, a great honor and an amazing opportunity for me collaborating with you.

I arrived to the production of this thesis only in virtue of the support of the Elettra Sincrotrone Trieste management, the Coordinator of the Accelerator Group, A. Fabris, and the FERMI Project Director, M. Svandrlik, who strongly supported this research activity.

Thanks also to Dr. W. Wuensch, at CERN, for having given to me the opportunity of collaborating with the CLIC group.

I also want to thank my colleagues in Elettra, S. Di Mitri and N. Shafqat, who have directly contributed to this work.

Voglio infine ringraziare mia moglie Mary, che mi ha sempre sostenuto ed incoraggiato nel conseguimento dei miei obiettivi e dei miei sogni, ed il mio piccolo, grande Matteo.... nonostante la tua tenera età, sei disposto a sacrificarti con gioia affinchè il tuo papà possa continuare ad imparare, anche se questo ci tiene lontani. Spero che la tua voglia di imparare, di viaggiare e di scoprire non ti abbandoni mai e ti guidi nelle tue scelte future.

Contents

List of Figures

List of Tables

To my wife Mary, and my son Matteo

Abstract

The principle of operation of the Free-Electron Lasers (FELs) was invented in 1971, but only in recent years it has become clear that these devices are very powerful light sources in the X-ray regime. Their high pulse energy, the femtosecond duration of the X-ray pulses, as well as their coherence, open new fields of research, which were inaccessible in the present third generation light sources. The main components of a FEL are a linear accelerator (Linac), providing a bunched relativistic electron beam, and a chain of undulator magnets, where the electrons move along sinusoidal trajectories and emit an undulator radiation concentrated in a narrow angular cone along the undulator axis. The fundamental wavelength emitted is proportional to the relativistic Lorentz factor of the electrons, which typically reaches values of several thousands for X-ray emission.

The free-electron laser FERMI is the seeded FEL user facility at the Elettra laboratory in Trieste, operating in the VUV to EUV and soft X-rays spectral range. The electron bunches are produced in a laser-driven photo-injector and accelerated to energies up to 1.5 GeV in the Linac.

In order to extend the FEL spectral range to shorter wavelengths, a feasibility study aimed to increase the Linac energy from 1.5 GeV to 1.8 GeV is currently ongoing. A proposal to replace the existing Backward Traveling Wave sections with new S-band accelerating structures tailored for high gradient operation, low breakdown rates and low wakefield contribution is presented and discussed in this thesis.

The complete radiofrequency (RF) design of the new structure is presented. Particular care has been given to the minimization of the electric and magnetic surface fields, in order to reduce the breakdown probability, and to the reduction of the residual quadrupole component of the fields in the RF coupler. A compact solution for an RF pulse compressor system, aimed to enhance the peak power delivered to the structure, is also discussed.

In order to prove the feasibility and the reliability of operating at the high gradient that would be required to achieve 1.8 GeV, a first short prototype of the new accelerating structure is now under construction, in collaboration with the Paul Scherrer Institut (PSI),

and will be tested at very high power in the upgraded FERMI Test Facility, starting from May 2018.

1 The FERMI Free Electron Laser

1.1 Overview

The principle of operation of the Free-Electron Laser (FEL) was invented in 1971 [1]. For many years, FELs have played a marginal role in comparison with conventional lasers. Only in recent years it has become clear that these devices are very powerful light sources in the X-ray regime [2, 3]. Their high pulse energy and the femtosecond duration ($1\ fs = 10^{-15}\ s$) of the X-ray pulses, as well as their coherence, open entirely new fields of research, for example structural analysis of individual bio-molecules and dynamics of processes in complex materials and molecules, which were inaccessible in present third generation light sources [4].

The main components of a FEL are a linear accelerator, providing a bunched relativistic electron beam, and a chain of undulator magnets [5]. An undulator magnet is a periodic arrangement of many short dipole magnets of alternating polarity. The electrons move along sinusoidal trajectories through the magnet (see Figure 1.1), so that the overall deflection of the beam is zero, and they emit an *undulator radiation* concentrated in a narrow angular cone along the undulator axis, which consists of narrow spectral lines.

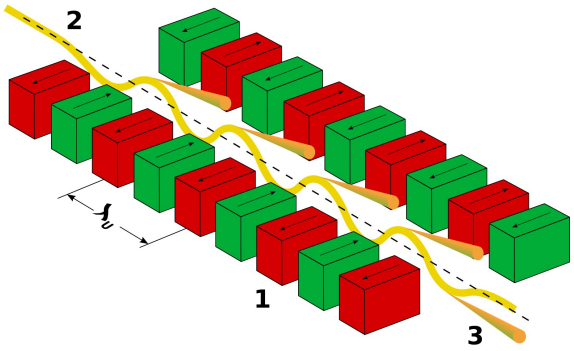

FIGURE 1.1: Schematic representation of the electron motion in a planar undulator and of the emission of undulator radiation.

The fundamental wavelength emitted is proportional to λ_u/γ^2 , where λ_u is the undulator period, typically a few centimeters long, and γ is the relativistic Lorentz factor of the electrons, which typically reaches several thousand for X-ray emission. So, the radiation wavelength can be more than a million times shorter than the undulator period.

In a FEL a huge number of electrons radiate coherently, due to a process of self-organization on the scale of the light wavelength, the so-called microbunching [5]. As a consequence, the radiation power scales quadratically with the number of the particles.

High-gain FELs are often considered as the fourth generation of accelerator-based light sources. In contrast to existing synchrotron radiation light sources (referred to as third generation machines), which are mostly storage rings equipped with undulators, the FEL requirements on the electron beam quality, in terms of small beam cross section, high charge density and low energy spread, are so demanding that presently only linear accelerators (Linacs) can be used to provide the drive beam.

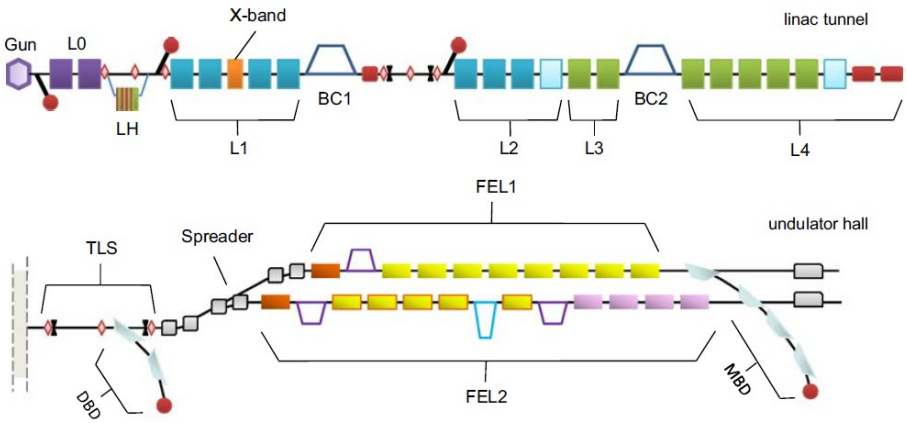

FIGURE 1.2: FERMI electron and photon beam delivery system: in the Linac Tunnel area, right after the gun, the beam is injected in a linear accelerator. The beam then passes through the Undulator Hall where two undulator chains (FEL1 and FEL2) can be used to produce photon beams at the required wavelength.

The free-electron laser FERMI installed at *Elettra Sincrotrone Trieste* (Trieste, IT) [6] is shown schematically in Figure 1.2. The electron bunches are produced in a laser-driven photo-injector and accelerated to energies up to 1.5 GeV in the Linac. The electron bunch, typically with a charge of 800 nC, is injected in the main Linac, where the acceleration to high energy takes place in normal-conducting, travelling-wave structures operating at 3 GHz (represented by the blocks in the Linac Tunnel area of Figure 1.2).

A fourth-harmonic structure with a resonance frequency of about 12 GHz (X-Band in Figure 1.2) is used for a linearization of the longitudinal phase space distribution. The electron bunches are longitudinally compressed in two magnetic bunch compressor chicanes (namely BC1 and BC2) and then accelerated to their final energy. The FERMI nominal compression factor of 10 can be implemented with either a two stage compression (using both BC1 and BC2) or with BC1 only.

As illustrated in Figure 1.2, the undulator system is composed by two distinct undulator lines (namely FEL1 and FEL2) covering, respectively, the fundamental wavelength range 20-100 nm (FEL1) and 4-20 nm (FEL2). In both lines, the amplification of the FEL signal occurs along APPLE-II-type undulators (out-of-vacuum planar undulators of movable gap), which allow tuning of the FEL wavelength in the aforementioned ranges, as well as of the polarization [7].

The photon beams from the FELs are then transported downstream to the Experimental Hall.

1.2 The FERMI Linac

1.2.1 The RF gun

The high bunch charge needed in a high-gain FEL can be accomplished by photocathodes illuminated with short ultraviolet laser pulses. The electron source at FERMI consists of a laser-driven photocathode which is mounted inside a radio-frequency (RF) cavity (see Figure 1.3). The photocathode is located at the backplane of the half-cell where the accelerating field assumes its peak value.

A static magnetic solenoid field is superimposed and provides focusing in order to ensure that the beam cross section remains small.

It is not possible to generate a high peak current of several hundreds of Ampere in the gun because, in this case, huge space charge forces would arise and would immediately disrupt the bunch. For this reason, bunches with a modest current (tens of Ampere) are produced by laser pulses of 10 ps duration. However, even in this case, the particles must be accelerated as quickly as possible to relativistic energies. In the relativistic regime, the repulsive electric forces between the electrons are largely canceled by the attractive magnetic forces between the parallel currents.

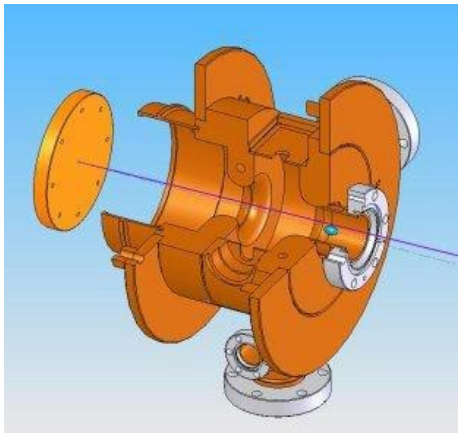

FIGURE 1.3: Sketch of the FERMI radio-frequency gun

1.2.2 The Linac

After the gun, the electron beam is boosted to 100 MeV with two, dual-feed accelerating structures, both 3 meters long. These dual-feed structures have been recently installed, replacing the old ones (S0A and S0B) [8], equipped with single-feed RF couplers: due to this, a head-tail kick was affecting the beam, worsening the beam emittance in the injector region.

After the replacement of S0A and S0B with the two new structures (RI), a reduction of the transverse kick induced by the input coupler was observed, with an important benefit to the beam emittance: with a 700 pC bunch charge, normalized emittances of 0.7 and 0.9 $mm\ mrad$ in the horizontal and vertical plane, respectively, were measured at 100 MeV. These values resulted to be 10-15 $\%$ smaller than the ones with the previous sections.

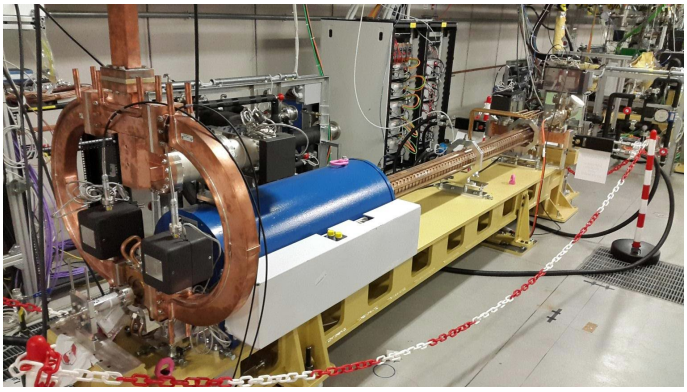

FIGURE 1.4: RI structure in the Test Facility for RF conditioning

The single-feed structures S0A and S0B were then moved in the high energy part of the Linac (see Figure 1.5) where the beam is more energetic and the head-tail kick, imposed by the field asymmetries in the coupler region, is less relevant.

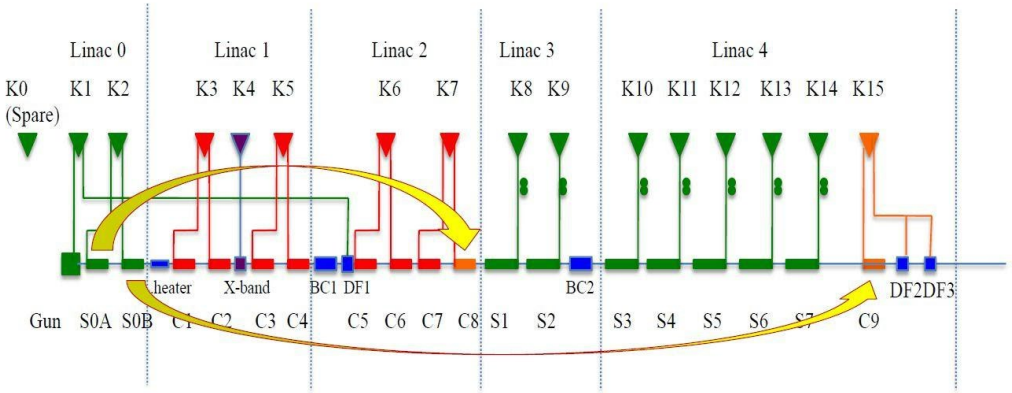

FIGURE 1.5: Relocation of S0A and S0B in the high energy part of the machine

Seven CERN-type (C1-C7) and one 3 meter long (S0A) accelerating structures, L1 and L2 in Figure 1.2, are located upstream and downstream of BC1, respectively. The four accelerating structures of L1 (C1-C4) are operated off-crest (i.e. the electron beam is not injected on the crest of the sinusoidal accelerating field) to impose the needed *linear energy chirp* (i.e. a linear energy variation between the head and the tail of the bunch) required for the bunch compression in the magnetic chicane BC1.

Linac3 (L3) and Linac4 (L4), located upstream and downstream of BC2 respectively, are composed by seven Elettra-type accelerating structures (S1-S7), 6.4 meters long, and by one 3 meter long (S0B) section.

All the accelerating structures up to L2 are forward travelling wave (FTW) sections, on-axis coupled, and operated at a modest gradient of 15 MV/m. The Elettra-type structures, coming from the previous injector of the Elettra synchrotron, are instead backward travelling wave (BTW), magnetically coupled structures: their nose-cone geometry and small beam apertures provide a very high shunt impedance and higher operating gradient, up to 25 MV/m. Unfortunately, the smaller iris radius of 5 mm, compared to the radius of 9 mm in the FTW structures, leads to a higher wakefield contribution that induces a higher electron beam energy loss and emittance dilution.

Table 1.1 summarizes all the relevant parameters for the FERMI accelerating structures.

TABLE 1.1: RF parameters for the FERMI structures

	Injector	S0A-S0B	C1-C7	S1-S7	
Length	3.2	3.2	4.5	6.1	[m]
Average Beam Aperture	10.55	9.73	9.73	5	[mm]
Type	FTW	FTW	FTW	BTW	
Shunt Impedance	60.5	67	65	70	$[M\Omega/m]$
Filling Time	870	900	1250	770	[ns]

1.2.3 The bunch compressor

We have seen that the high peak current (several hundreds of Ampere), needed in linac-based X-ray free electron lasers, cannot be produced directly in the electron gun, because huge space charge forces would disrupt the beam within short distance. Therefore, bunches with a modest peak current are created in the RF photo-injector, accelerated to higher energy and then compressed in length.

The electrons in the Linac have speeds very close to c, and the velocity differences are too small to allow a trailing electron in the bunch to have a chance to catch up with a leading electron if the particles move on a straight line. This chance is opened if the particles travel through a chicane consisting of bending magnets.

Longitudinal bunch compression is achieved in two steps [5] as shown in Figure 1.6: first, an energy slope is imprinted on the bunch by off-crest acceleration, with the particle at the tail of the bunch receiving a larger energy gain than those at the head. Afterwards, the particles are passed through a magnetic chicane where the trailing electrons, of larger energy, travel along a shorter distance than the leading ones of smaller energy, and are thus enabled to catch up with them.

1.3 The Linac upgrade plan

As we have seen before, the FEL resonance condition [4] establishes an inverse relationship between the radiation wavelength and the energy squared of the irradiating electron beam. In fact, the fundamental wavelength emitted in a FEL is proportional to λ_u/γ^2 , where γ is the relativistic Lorentz factor of the electrons, which is proportional to the electron beam energy. A higher beam energy allows either lasing at shorter wavelengths for a fixed undulator field, or lasing at a given wavelength with a higher flux, when the undulator field is re-tuned on resonance.

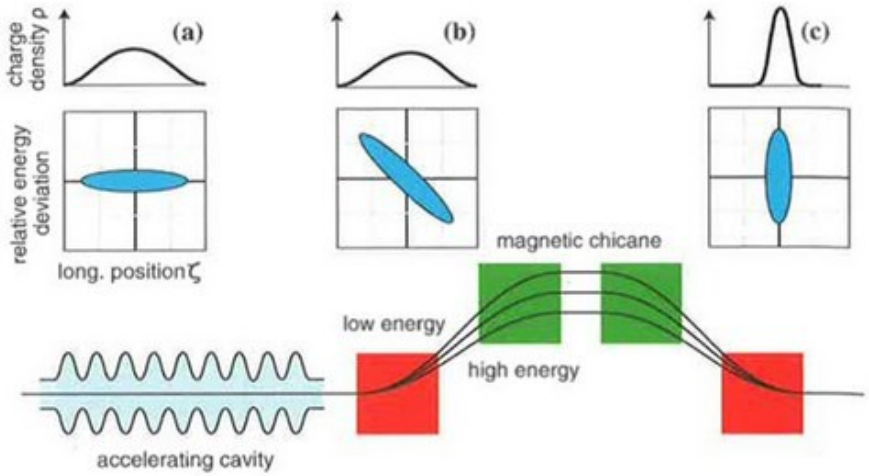

FIGURE 1.6: Principle of longitudinal bunch compression of a relativistic electron bunch. The bottom view shows an accelerating cavity and the four dipole magnets of the magnetic chicane. The top figures show the longitudinal bunch charge distribution and the correlation between the longitudinal position ς of an electron inside the bunch and its relative energy deviation, at three different locations: **(a)** In front of the cavity, **(b)** behind the cavity, **(c)** behind the magnetic chicane. In the RF cavity the trailing electrons receive a larger energy gain than the leading ones. In the magnetic chicane the electron at the tail of the bunch move on a shorter orbit than those at the head and catch up with them. Figure and caption from reference [5].

So, operating with high accelerating gradients, shorter wavelengths or higher flux can be achieved for a given length of the Linac.

As already illustrated in the previous section, L3 and L4, located upstream and downstream of the second bunch compressor BC2, are equipped with BTW accelerating structures designed for high gradient operation. Nonetheless, as it will be shown, peak surface fields and RF heating phenomena limit the attainable accelerating gradient.

The need for shorter radiation wavelength, together with the wish of a higher Linac reliability, suggest an upgrade of the FERMI Linac.

1.3.1 The backward travelling-wave accelerating structures

Each BTW accelerating section is a 6.4 m long structure comprised of 162 nose-cone cavities magnetically coupled [9, 10], as shown in Figure 1.7. The group velocity v_g is kept constant along the section by means of a constant geometry of the coupling slots; their

shapes and relative positioning have been chosen to get a v_g approximately equal to 2.6% of the speed of light, c. This translates in a filling time (the time needed for the radio-frequency power to propagate along the travelling-wave structure and completely fill it) of nearly 770 ns.

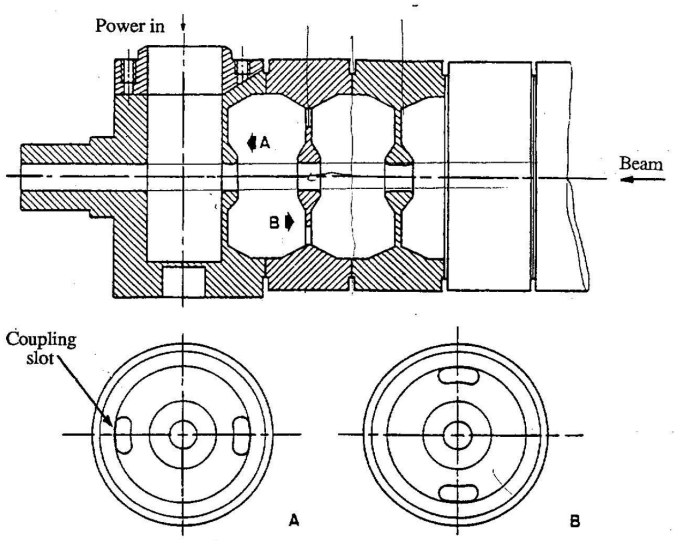

FIGURE 1.7: Sketch of the Backward Travelling Wave accelerating structure with nose cone geometry and magnetic coupling irises

Moreover, two different nose shape geometries have been used to maximize the axial electrical field: the last 109 cells have been designed for a higher shunt impedance value, in order to compensate the attenuation along the structure. Theoretically, an energy gain of nearly 200 MeV, corresponding to an accelerating gradient of 30 MV/m, should be achievable.

Each BTW is powered with a high peak power Klystron (45 MW) delivering up to 4.5 μs radio-frequency pulse width. Nonetheless, the amount of power available from the source would not be sufficient to reach the design gradient of 30 MV/m. So, each RF plant is equipped with a SLED pulse compressor.

The SLAC Energy Doubler (SLED) is a pulse compression system [11] consisting of a pair of resonant cavities excited symmetrically through a four-port 3 dB hybrid (see Figure 1.9), such that the power emitted from the resonators is directed to the accelerator, rather than back to the source. In the SLED network, the RF energy generated by the source (klystron), during most of the pulse's duration, is stored in the two high-Q resonators. The energy stored in then largely extracted during the last fraction of the pulse, increasing the peak power delivered to the accelerator (further details about SLED theory in

FIGURE 1.8: A Backward Travelling Wave accelerating structure equipped with a SLED type rf pulse compressor

following chapters).

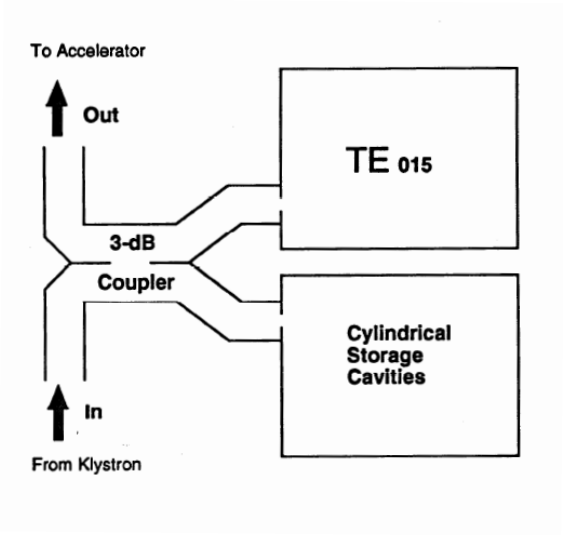

FIGURE 1.9: SLED pulse compression system

Though the BTW structures are designed for gradients up to 30 MV/m, routine operation showed that the operating gradient is actually limited to much lower values, since BTW structures suffer from increased breakdown rate even when operated at 24 MV/m.

As seen before, in the BTW structures, the RF power flows from one cell to the next

through coupling slots (see Figure 1.7 located in the area where the magnetic field is higher (magnetic coupling slot). Numerical simulations for a single cell [12] showed that surface electric field at the magnetic coupling slots becomes of the same magnitude and even higher than the surface electric field on the nose. As shown by the temperature distribution reported in Figure 1.10(a), high surface magnetic fields in the coupling slot region induce excessive pulse heating that limits the attainable gradient. Figure 1.10(b) shows the inner surface of the first cell of a BTW in proximity of the magnetic coupling slot: surface degradation, mostly due to high electric field and pulse heating effect, is evident.

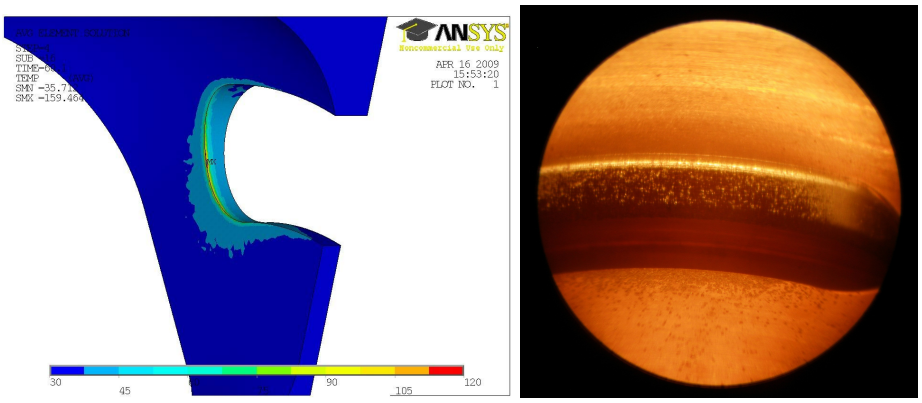

(a) Temperature profile for a BTW cell: evident pulse heating effects in proximity of the magnetic coupling slot

(b) Picture of the coupling slot of the first cell: visible surface degradation

FIGURE 1.10: Simulated thermal profile and picture of the coupling iris slot

So, even if a phase modulation [13] is introduced to obtain lower peak surface fields, the attainable accelerating gradient is limited to 24 MV/m at a repetition rate of 10 Hz, and to 18-20 MV/m at 50 Hz.

1.3.2 The new accelerating module

FERMI has achieved its nominal performance goals by the production of photon energies above 300 eV. However, there is great demand from scientific community to cover the whole water window by reaching both the nitrogen and oxygen K-edges. This will require the extension of the photon energy up to 600 eV.

FEL simulations show that this goal can be achieved by increasing the electron beam energy from the present value of 1.5 GeV up to 1.8 GeV, while the beam peak current should be pushed up to 1 kA.

As shown before, the BTW structures are limited in gradient, because of the high electric field values and the pulse heating phenomena in proximity of the magnetic coupling slots. For this reason, the goal energy of 1.8 GeV is not achievable in the present configuration. Also, the small beam aperture (5 mm radius) produces significant longitudinal and transverse wakefields which would strongly affect the beam dynamics at higher bunch charge.

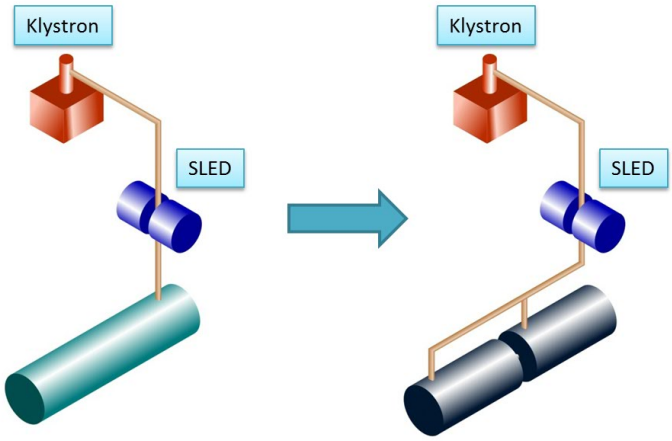

FIGURE 1.11: Layout of the new accelerating module: two 3.2 meters long structures will be installed in place of each BTW

Due to the above mentioned reasons, an upgrade plan for the FERMI Linac is currently under evaluation in order to extend the energy spectrum to higher values within the same space and RF power constraints. This plan will consist in replacing each BTW structure by a new accelerating module, which should guarantee a reliable operation at 30 MV/m and at 50 Hz repetition rate. Each module will consist of two 3 meter long accelerating structures with a larger iris aperture to reduce longitudinal and transverse wakefield contributions.

In the following chapters, the radio-frequency design of the final structure will be presented in detail. The wakefield analysis will also be discussed, as well as the impact of the replacement on the beam dynamics. The construction of a first short prototype of the new structure started in April 2017, and will be tested in the first half of 2018, at the FERMI Test Facility currently being upgraded.

2 FERMI Linac Novel Accelerating Structures

2.1 Electromagnetic waves and cavities

2.1.1 Propagation in free space

Maxwell's equations describe all (classical) electromagnetic phenomena [14]. In free space and in absence of sources (charge and current densities), Maxwell's equations are given by:

$$\nabla \times \vec{E} = -\frac{\partial \vec{B}}{\partial t} \tag{2.1a}$$

$$\nabla \times \vec{H} = \frac{\partial \vec{D}}{\partial t} \tag{2.1b}$$

$$\nabla \cdot \vec{D} = 0 \tag{2.1c}$$

$$\nabla \cdot \vec{B} = 0 \tag{2.1d}$$

The quantities $\vec{E}$ and $\vec{H}$ are the electric and magnetic *field intensities* and are measured in units of V/m and A/m, respectively. The quantities $\vec{D}$ and $\vec{B}$ are the electric and magnetic *flux intensities* and are in units of $coulomb/m^2$ and $weber/m^2$.

Considering the constitutive relations $\vec{D} = \epsilon\vec{E}$ and $\vec{B} = \mu\vec{H}$, where ϵ and μ are the *permittivity* and *permeability* of the medium respectively, and assuming a harmonic time dependance of the form $e^{j\omega t}$, Maxwell's equations reduce to:

$$\nabla \times \vec{E} + j\omega\vec{B} = 0 \tag{2.2a}$$
$$\nabla \times \vec{B} - j\omega\mu\epsilon\vec{E} = 0 \tag{2.2b}$$

For $\omega \neq 0$, the divergence equations can be found taking the divergences of equations 2.2a and 2.2b. Combining the equations 2.2a and 2.2b we get the Helmholtz wave equations:

$$\nabla^2\vec{E} + \mu\epsilon\omega^2\vec{E} = 0 \tag{2.3a}$$
$$\nabla^2\vec{B} + \mu\epsilon\omega^2\vec{B} = 0 \tag{2.3b}$$
$$\nabla \cdot \vec{D} = 0 \tag{2.3c}$$
$$\nabla \cdot \vec{B} = 0 \tag{2.3d}$$

A uniform plane wave, solution to equations of this form is a transverse electromagnetic (TEM) wave for which both the electric and magnetic field vectors are perpendicular to the direction of propagation of the wave. Assuming the z-axis as the direction of propagation, a form of the solution will be then:

$$\vec{E} = \vec{E}_0 e^{j(\omega t - kz)} \tag{2.4a}$$
$$\vec{H} = \vec{H}_0 e^{j(\omega t - kz)} \tag{2.4b}$$

where

$$k = \omega\sqrt{\mu\epsilon} \tag{2.5}$$

The equation 2.5 relates the wave number, $k = 2\pi/\lambda$, to the angular frequency. In particular, the equation shows that the phase velocity of the wave is given by:

$$v_{ph} = \frac{\omega}{k} = \frac{1}{\sqrt{\mu\epsilon}} \tag{2.6}$$

In vacuum, $v_{ph} = 1/\sqrt{\mu_0\epsilon_0} = c$, so the solution is a wave which propagates in the z-direction at the speed of light. It can also be easily shown that the group velocity (the velocity of propagation of the electromagnetic energy), $v_g = \partial\omega/\partial k$, is also $1/\sqrt{\mu\epsilon}$.

2.1.2 Propagation in bounded media

In bounded media, such as waveguides or resonators with conducting walls, TEM wave type is not always possible. Since a perfect electric conductor (as a first approximation, conducting walls can be considered as perfect conductors) allows no field penetration into the surface, the fields at the surface of the perfect conductor must satisfy the following conditions:

$$\widehat{n} \times \vec{E} = 0 \tag{2.7a}$$

$$\widehat{n} \cdot \vec{H} = 0 \tag{2.7b}$$

where $\widehat{n}$ is the vector normal to the conductor's surface. In case of bounded media, the propagation along the waveguide can be explained in terms of successive reflections from wall to wall [15]. For a wave with an oblique incidence on a conducting plane, the incident and reflected wave can in fact combine in such a way as to cancel the tangential component E_t of the electric field, and the normal component B_n of the magnetic field. The resulting wave will have a field component in the direction of propagation: this can be either the electric field component (*transverse-magnetic*, TM wave), or the magnetic field (*transverse-electric*, TE wave).

Observing an incident wave as shown in Figure 2.1, one sees that in the direction of propagation (z-direction), the distance between two adjacent wave crests, λ_p, is longer than the actual wavelength λ. This means that the wave moves in the z-direction with a phase velocity v_{ph} given by:

$$v_{ph} = \frac{\lambda_p}{\lambda} c = \frac{c}{\sin\alpha} > c \tag{2.8}$$

Physically, the phase velocity v_{ph} is the velocity at which the phase of the wave propagates in space. As shown in equation 2.8, in case of an oblique incidence, the resulting wave can have phase velocity (in the direction of propagation) grater than the velocity of light c.

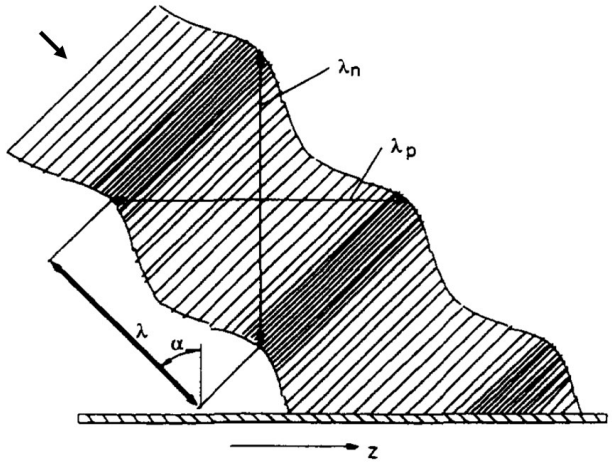

FIGURE 2.1: Oblique incidence of a wave with wavelength λ; λ_p and λ_n are the wavelengths parallel and perpendicular to the boundary, respectively

With one conducting wall, as in Figure 2.1, the angle of incidence can have any value. With two walls, as shown in Figure 2.2, only certain angles are allowed if boundary conditions are to be satisfied at both walls. For a given wave type (either transverse-electric or transverse-magnetic) one can therefore have only certain wave modes which present an integer number of half wavelengths between the walls. The wave in the longitudinal (or z-direction) is a travelling wave with the wavelength λ_p, and in the transverse direction (or x-direction), between the walls, has a standing wave pattern with the wavelength λ_n.

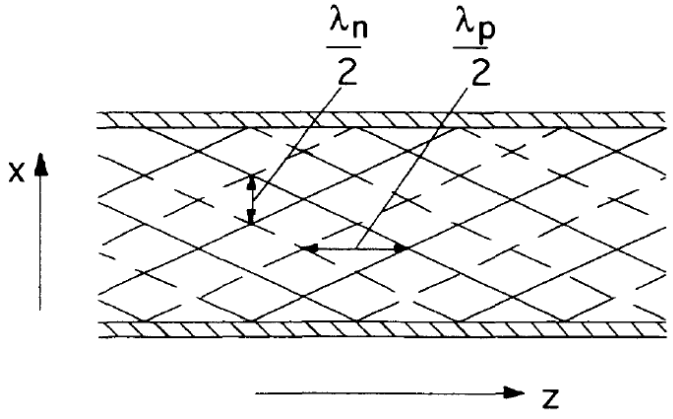

FIGURE 2.2: Waves between two perfectly conducting planes; λ_p is the wavelength of the travelling wave; λ_n is the wavelength of the standing wave

For accelerating a beam, we would need an electric field with a component along the direction of propagation of the particles. In a circular waveguide, the simplest solution having an axial electric field is the so-called TM_{01} mode, which consists of radial and longitudinal electric field components and an azimuthal magnetic field. In a cylindrical coordinate system (r, φ, z) the fields of such a TM_{01} wave travelling in the positive z-direction are [16]:

$$E_r = j\frac{k_z}{k_c}E_0 J_1(k_c r)\, e^{-jk_z z} e^{j\omega t} \tag{2.9a}$$

$$E_z = E_0 J_0(k_c r)\, e^{-jk_z z} e^{j\omega t} \tag{2.9b}$$

$$H_\varphi = j\frac{k}{Z_0 k_c}E_0 J_1(k_c r)\, e^{-jk_z z} e^{j\omega t} \tag{2.9c}$$

where E_0 is the amplitude of the electric field, J_0 and J_1 are the Bessel functions of the first kind of zero and first order respectively, $k = 2\pi/\lambda = \omega/c$ is the wave number, k_z the wave propagation constant, and Z_0 the wave-impedance in free space. As it is known, $k_z = k\sqrt{1-\omega_c^2/\omega^2}$, where ω_c is the cutoff angular frequency of the TM_{01} mode, and $Z_0 = \eta\sqrt{1-\omega_c^2/\omega^2}$, with $\eta = \sqrt{\mu/\epsilon}$.

If we consider a circular waveguide of radius b (we assume perfectly conducting walls), the boundary condition forces $E_z = 0$ at $r = b$, which means $J_0(k_c b) = 0$ and leads to a certain cut-off wavelength λ_c, or equivalently to a cut-off angular frequency ω_c. Below this frequency the wave will be damped exponentially. The relations between cut-off wavelength, cut-off wave-number k_c and the propagation constant k_z are given by:

$$\lambda_c \approx 2.61 b \tag{2.10a}$$

$$k_z^2 = k^2 - k_c^2 \tag{2.10b}$$

$$k_c = \frac{2\pi}{\lambda_c} = \frac{\omega_c}{c} \tag{2.10c}$$

Using the phase velocity $v_{ph} = \omega/k_z$ and the propagation constant we can write:

$$v_{ph}^2 = c^2\frac{\omega^2}{\omega^2 - \omega_c^2} \tag{2.11}$$

From equation 2.11 we see that $v_{ph} > c$. So, it is clear that a uniform waveguide is not suitable for accelerating particles, because synchronism between the wave and the particles (approximately travelling with the speed of light, in case of electrons) is not possible.

In order to use electromagnetic waves for the acceleration of particles one must first slow the waves down.

2.2 Periodic accelerating structures

2.2.1 Waves in loaded cavities

As discussed above, the waves in an empty waveguide always have $v_{ph} > c$. In order to slow down the phase of the wave, we have to load the cavity by introducing some periodic obstacles into it [15]. Figure 2.3 shows a disc-loaded cavity with a period (or cell length) L.

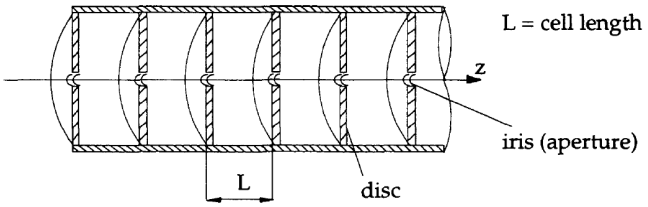

FIGURE 2.3: Disc-loaded cavity

The Floquet's theorem for periodic structures states that, in a given mode of oscillation and at a given frequency, at the same locations in different periods the amplitudes of the propagated fields are the same but their phases differ by a factor e^{-jk_0L} (for lossy structures the constant k_0 is complex). So, we can write:

$$E_z(r,z,t) = E(r)\, e^{j(\omega t - k_0 z)} \tag{2.12}$$

Since the amplitude is a periodic function, we can express $E(r)$ as a Fourier series in z. We have:

$$E_z(r,z,t) = \sum^{n} E_n J_0(k_n r)\, e^{j(\omega t - k_n z)} \tag{2.13}$$

where $k_n = k_0 + 2\pi n/L$ is the wave-number of the n^{th} space harmonic, which has a phase velocity given by:

$$v_{ph} = \frac{\omega}{k_n} = \frac{\omega}{k_0\left(1 + 2\pi n/k_0 L\right)} \leq c \tag{2.14}$$

For each n we have a travelling wave with its own phase velocity

$$v_{ph,n} = \frac{\omega}{k_0 + 2\pi n/L} = \frac{\omega}{k_n}. \tag{2.15}$$

From above expressions we see that a travelling wave consists of infinite space harmonics waves: since the various space harmonic waves have different phase velocities, only one of them can be used resonantly to accelerate particles. The fundamental mode ($n = 0$) generally has the largest amplitude and hence is used for acceleration.

2.2.2 Travelling-wave linear accelerators

In a disc-loaded cavity, a wave will propagate through the cavity with a phase velocity $v_{ph} = \omega/k$ (where k is the propagation constant of the selected harmonic) and a group velocity (the velocity of propagation of the energy) given by $v_{ph} = d\omega/dk$ [17].

At the end of the cavity this energy can be dissipated into a matched load. In this case the cavity is, in a certain sense, a waveguide, and RF accelerators working this way are called travelling-wave linear accelerators. Figure 2.4 shows schematically a travelling-wave accelerating structure, with its input and output couplers. These couplers are in fact waveguides, matched to the characteristic impedance of the structure, by which the RF power is fed into the cavity, and the output RF power transferred to the matched load.

2.2.2.1 Essential parameters for a linear accelerator

In dealing with accelerators, some important design parameters have to be defined:

1. The Shunt impedance R_{sh} per unit length:

$$R_{sh} = \frac{E_z^2}{-dP/dz} \tag{2.16}$$

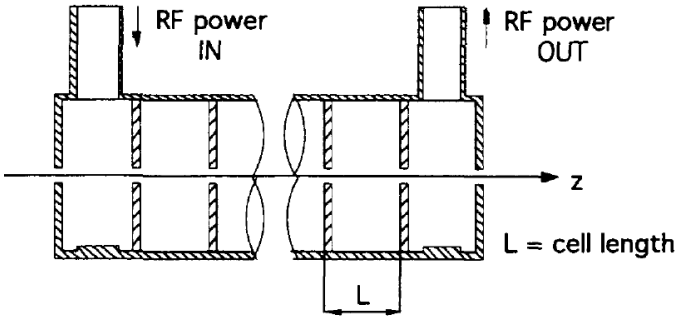

FIGURE 2.4: Schematics of a travelling-wave linear accelerator with input and output couplers

where E_z is the axial electric field synchronous with the particle, and $-dP/dz$ is the RF power dissipated in the walls of the accelerator per unit length. The shunt impedance is a measure of the ability of a structure to accelerate particles, and is usually expressed in $M\Omega/m$. A high R_{sh} means an efficient acceleration for a given dissipated RF power.

2. The Quality Factor Q_0, defined as the ratio of the energy stored in the cavity to the energy lost due to RF dissipation in the cavity per radian of the RF cycle:

$$Q_0 = \frac{\omega w}{-dP/dz} \tag{2.17}$$

where ω is the RF angular frequency, and w is the stored energy per unit length.

3. The Group Velocity v_g

$$v_g = \frac{P}{w} \tag{2.18}$$

where P is the power flowing in the structure. The group velocity is the velocity at which the RF energy flows through the accelerator. The group velocity v_g depends strongly upon the ratio of the diameter of the disk aperture $2a$, to the diameter of the accelerator cavity $2b$.

4. The Filling Time

$$t_F = \int_0^l \frac{dz}{v_g\,(z)} \tag{2.19}$$

where l is the length of the accelerating structure.

The filling time is the time needed for the electromagnetic energy to fill the accelerator, prior to the acceleration of particles.

2.2.3 Constant-impedance vs constant-gradient structures

Accelerating sections could be either *constant-impedance* (CI) or *constant-gradient* (CG) type; in a constant impedance design, all accelerating cells are identical and the shunt impedance remains constant along the whole structure. However, the flowing power is attenuated along the structure and the resulting accelerating gradient (the rate of change of the beam energy, per meter and unit charge, measured in MV/m) decreases as well. Instead, in a constant gradient solution, the geometrical parameters are changed cell by cell to compensate for the ohmic losses: this solution provides a more efficient acceleration, since it keeps the surface field values constant over the whole structures.

As stated above, along the accelerator a fraction of the power is dissipated in the cavity walls and the electric field is attenuated according to the following equation [15]:

$$\frac{dE_z(z)}{dz} = -\alpha(z) E_z(z) \tag{2.20}$$

where $\alpha(z)$ is the attenuation constant of the accelerator. Correspondingly:

$$\frac{dP(z)}{dz} = -2\alpha(z) P(z) \tag{2.21}$$

Using the expressions of Q_0 and w given in equations 2.17 and 2.18 respectively, we also have:

$$\frac{dP(z)}{dz} = -\frac{\omega}{Q_0}\frac{P(z)}{v_g(z)} \tag{2.22}$$

Comparing equations 2.21 and 2.22 it follows that:

$$\alpha(z) = \frac{\omega}{2Q_0 v_g(z)} \tag{2.23}$$

In a *constant-impedance* accelerator we have:

$$\alpha(z) = const = \alpha \tag{2.24}$$

$$E_z(z) = E_z(0)\, e^{-\alpha z} \tag{2.25}$$

Therefore, the energy gain of a particle of charge q, sitting on the crest of the wave in a constant-impedance accelerating structure of length l is:

$$qV = q\int_0^l E_z(0)\, e^{-\alpha z} dz = qE_z(0)\, l \frac{1 - e^{-\alpha l}}{\alpha l} \tag{2.26}$$

In the case of a *constant-gradient* accelerator, and assuming that variations in the dimensions practically do not affect the shunt impedance R_{sh}, we have:

$$E_z = const \tag{2.27}$$

$$R_{sh} = \frac{E_z^2}{-dP(z)/dz} = const \tag{2.28}$$

From equations 2.27 and 2.28 it follows that the variation of P along the accelerator is also constant:

$$-\frac{dP(z)}{dz} = const = \frac{d}{dz}\left(P(0) + \frac{P(l) - P(0)}{l} z\right). \tag{2.29}$$

With

$$P(l) = P(0)\, e^{-2\int_0^l \alpha(z) dz} = P(0)\, e^{-2\tau}, \tag{2.30}$$

one can write

$$\frac{dP(z)}{dz} = -P(0)\frac{1 - e^{-2\tau}}{l} = const \tag{2.31}$$

where τ is the total attenuation along the accelerating structure, given by:

$$\tau = \int_0^l \alpha(z)\, dz. \tag{2.32}$$

Since $dP(z)/dz = const$, the group velocity in a constant-gradient accelerator is not constant, but decreases linearly as $P(z)$:

$$v_g(z) = -\frac{\omega P(z)}{Q_0 dP(z)/dz} \propto P(z) \tag{2.33}$$

Comparing constant-impedance (CI) and constant-gradient (CG) accelerators, it can be verified that the ratio of maximum-to-average axial electric field strength is unity in the CG structure, whereas in the CI structure is given by:

$$\frac{E_0}{V_0/L} = \frac{\tau}{1-e^{-\tau}} \tag{2.34}$$

where τ is the RF attenuation parameter, which can be shown to be equal to $\omega t_F/2Q_0$. The dependence of τ upon the filling time t_F emphasizes the importance of comparing the CG and CI structures assuming the same value of τ. For equal τ, in fact, the two structures have the same filling time, the same stored energies and the same ratios of input-to-output RF powers.

The ratios of maximum-to-average axial electric field strength vs τ are shown in Figure 2.5. Thus it is clear that the CG structure can produce higher electron energies than an optimized CI structure when both are operating at the breakdown limit of the electric field strength. As indicated in Figure 2.5, the relative advantage of the CG accelerator in achieving high gradients without breakdown depends upon the value of τ.

2.2.4 RF breakdown

The limitations coming from RF breakdown in vacuum strongly influence the design of high gradient accelerating structures. Even though these structures are operated under vacuum, electromagnetic fields are high enough to cause arcs. In the framework of Compact LInear Collider (CLIC) study [18, 19], a significant effort has been made to derive the high gradient limit due to RF breakdown and to collect all available experimental data.

The surface electric field was long considered to be the main quantity which limits accelerating gradient because of its direct role in field emission. However, as more data became available, it was clear that the maximum surface electric field does not serve as an ultimate constraint in the RF design of high gradient structures.

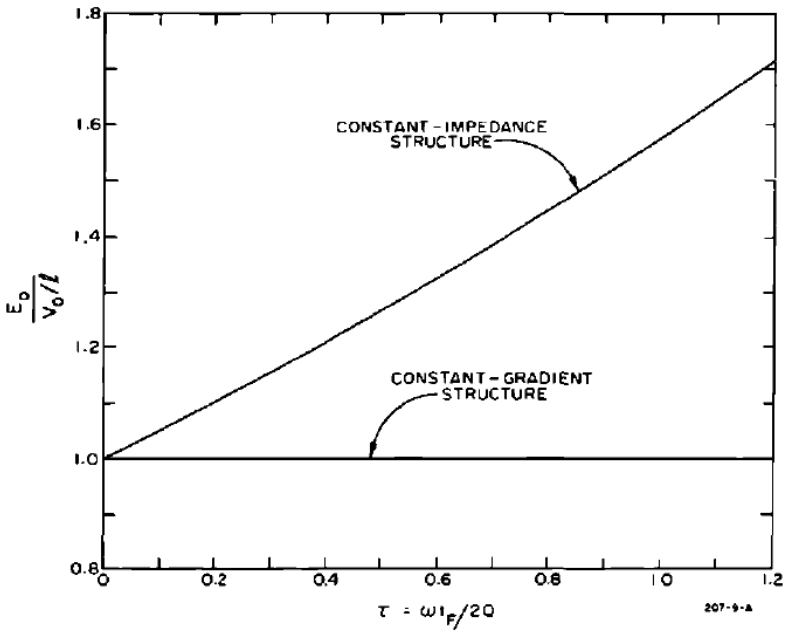

FIGURE 2.5: Ratios of maximum-to-average axial electric field strengths in CI and CG structures versus τ

The exact shape and nature of breakdown sites before breakdown is not known very well, and their size is an open question. Nevertheless, the assumption that there are small features on the surface which enhance surface electric fields and cause significant field emission is commonly used.

The simplest model of such a protrusion, a cylindrical tip of height h and radius r surmounted by a hemispherical cap, is shown in Figure 2.6. The electrical field distribution around the tip is strongly modified by the presence of the tip so that the field is enhanced, at the highest point of the tip, by the so-called field enhancement factor $\beta \cong h/r$. The local electric field is there βE, where E is the value of homogeneous electric field around the tip outside the region indicated in Figure 2.6 by the dashed line.

It is assumed that the field emission current flowing along the tip heats it so that the temperature at the end of the tip is the highest. It is found that only tips of rather small size (on the nanometer scale) can reach very high temperature in the time scale of interest for us.

It is obvious that any heating requires power and there is no other source of power than the electromagnetic power flow along the surface. A new quantity, the modified Poynting vector S_c has been then introduced [19] and used as the primary constraint for the

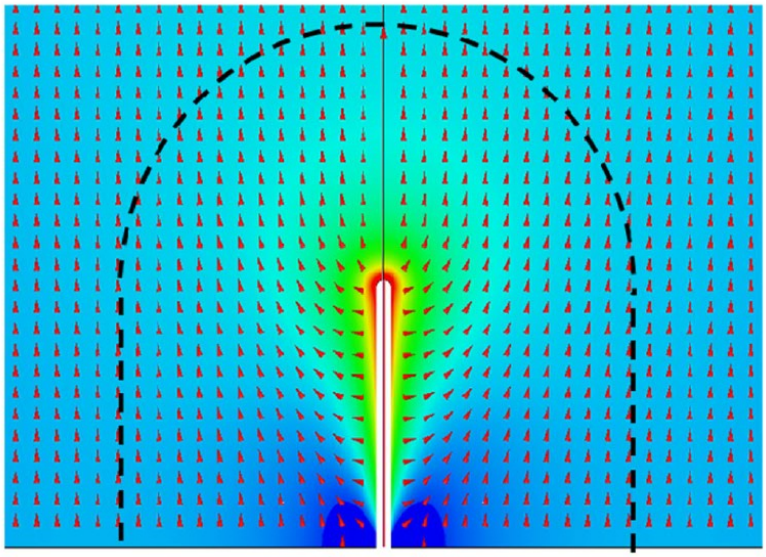

FIGURE 2.6: Geometry and electric field distribution near a cylindrical tip. Arrows show the direction and color code is proportional to the logarithm of its absolute value

breakdown rate (BDR). S_c is defined as:

$$S_c = \left|\Re\left\{\vec{S}\right\}\right| + g_c \left|\Im\left\{\vec{S}\right\}\right| \tag{2.35}$$

The real part $\Re\left\{\vec{S}\right\}$ of the Poynting vector $\vec{S} = \frac{1}{2}\vec{E} \times \vec{H}^*$ describes the active power surface density in a travelling wave structure; g_c is a weighting factor and the imaginary part $\Im\left\{\vec{S}\right\}$ represents instead the reactive power surface density, related to energy oscillations, on each cycle, back and forth from the region of the electric field to the region of the magnetic field.

The modified Poynting vector S_c has been shown to fit experimental data of both travelling and standing wave cavities over a broad frequency range. This quantity, scaled to the 3 GHz case, will be used in the present work to predict the expected breakdown rate of the novel accelerating structure for the FERMI Linac upgrade plan.

2.3 Novel accelerating structures

As already described in Chapter 1, the high energy part of the FERMI Linac is equipped with seven, 6.4 meter long, BTW structures: each structure consists of nearly 160 cells,

magnetically coupled with a nose cone geometry.

Each BTW, powered with a 45 MW and 4.5 μs klystron, is equipped with a Slac Energy Doubler (SLED) for pulse compression (pulse compression theory and RF pulse compressor systems will be described in a following chapter) in order to attain high gradient at the expense of RF pulse length to achieve higher electron beam energy.

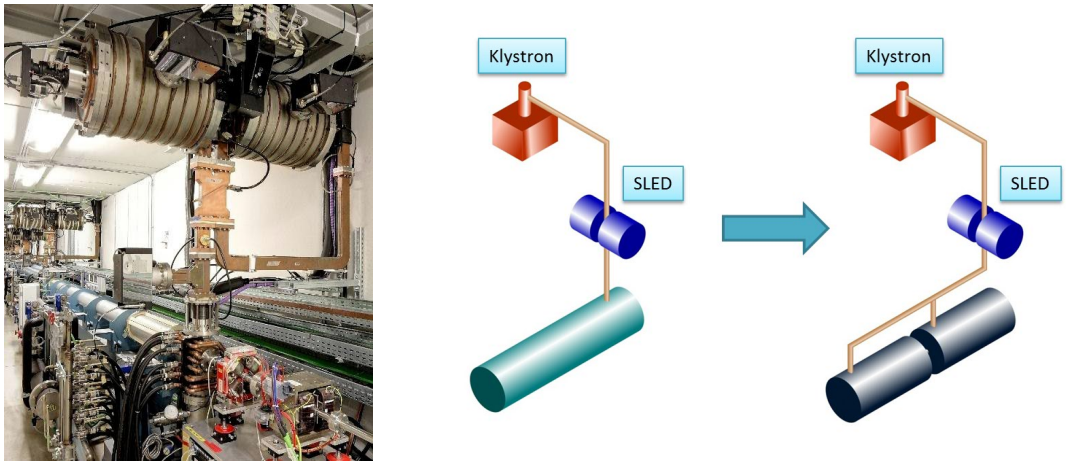

(a) FERMI Linac BTW (b) FERMI novel accelerating module

FIGURE 2.7: A picture of the BTW structures presently installed in the Linac tunnel and a sketch of the new accelerating module

Theoretically an accelerating gradient of nearly 30 MV/m should be achievable [9] but routine operation showed that operating gradient is limited to 24 MV/m due to increased breakdown rate in BTW. Also, as we will see in the following, the small beam aperture (5 mm radius) produces significant longitudinal and transverse wakefields which affect the beam dynamics at high bunch charge. Higher charges and beam currents are in fact necessary to improve the FEL performances at shorter wavelengths.

All the limitations coming from surface electromagnetic fields and wakefields effects, suggested to plan an upgrade for the FERMI Linac. The upgrade will consist in the replacement of each BTW with a new accelerating module consisting of two, newly designed, 3.2 meter long structures, as shown in Figure 2.7. In the following sections the design of input and output power couplers as well as the design of the full structure will be presented and discussed in detail.

2.3.1 RF couplers design

RF power couplers are passive components designed to efficiently transfer the power from an RF power source (klystron) to the accelerating cavity. Power couplers have to match the impedance of the klystron and RF distribution system to the beam-loaded cavity, dealing with very high power level in pulsed or continuous-wave operation.

As confirmed by recent experimental results with X-band accelerator structures [20, 21], the RF power coupler is the region most prone to RF breakdown and surface degradation. Furthermore, geometric asymmetries in the coupler can generate dipole and quadrupole electromagnetic field components and, consequently, induce a head-tail kick on the e-beam, causing an unacceptable emittance degradation.

In the following, after an introduction about the analysis of electromagnetic field asymmetries, two different solutions for RF power couplers will be investigated and the corresponding RF performances will be compared [22, 23, 24].

2.3.1.1 Field asymmetry analysis

Field asymmetries in the coupler cell and the minimization of the residual quadrupole components have been widely studied in the past years [25, 26, 24, 27].

While providing good matching, the coupling slots may in fact produce non-axial symmetric field distribution in the coupler region. As stated above, the residual asymmetries can worsen beam quality and generate undesired emittance growth. This is particularly detrimental for low emittance beams at low energies, and in the injector accelerators for light sources.

The actual impact on the electron beam dynamics produced by field asymmetries in the coupler region can be studied by analyzing the transverse momentum change experienced by the particles passing through the RF coupler.

A particle of charge q, moving with velocity $\vec{v}$ through an electromagnetic field, experiences the Lorentz force:

$$\vec{F} = q\left[\vec{E} + \vec{v} \times \vec{B}\right] \tag{2.36}$$

where $\vec{E}$ is the electric field and $\vec{B}$ is the magnetic flux density acting on the particle.

For an ultra-relativistic particle of charge q and momentum p, passing through an RF quadrupole, the transverse kick is given by:

$$\Delta\vec{p}_{\perp} = pk_2\,(x\hat{u}_x - y\hat{u}_y)\,cos\omega t \tag{2.37}$$

where ω is the operating angular frequency, $\hat{u}_x$ and $\hat{u}_y$ are the unit vectors of the x and y axis respectively, and k_2 is the amplitude of the normalized integrated quadrupolar strength [26].

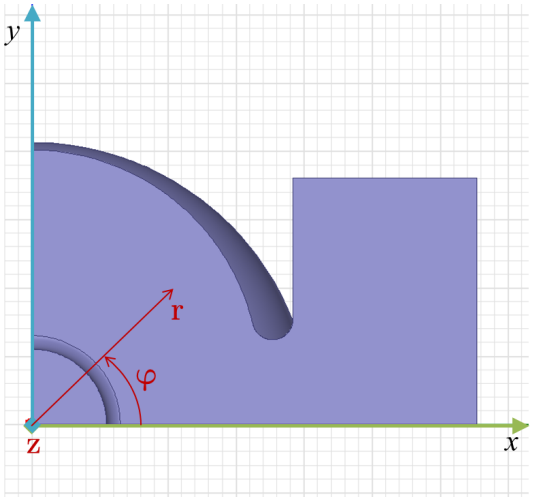

FIGURE 2.8: Transverse section of the structure and circular cylindrical coordinates

The focusing strength of the quadrupolar field can be calculated by equation 2.38; the corresponding defocusing strength is instead calculated according to equation 2.39.

$$k_{2,x} = \frac{q}{pc}\frac{1}{\pi r}\int_0^{2\pi}\left\|\int_0^L F_x\,(r,\varphi,z)\,e^{j\frac{\omega z}{c}}\,dz\right\|cos\varphi d\varphi \tag{2.38}$$

$$k_{2,y} = \frac{q}{pc}\frac{1}{\pi r}\int_0^{2\pi}\left\|\int_0^L F_y\,(r,\varphi,z)\,e^{j\frac{\omega z}{c}}\,dz\right\|sin\varphi d\varphi \tag{2.39}$$

In equations 2.38 and 2.39, the integration point is expressed in the circular cylindrical coordinates (r,φ,z), as shown in Figure 2.8; F_x and F_y are the x and y components, respectively, of the Lorentz force, and c is the velocity of light in vacuum.

For any ideal quadrupole, $k_{2,x} = -k_{2,y}$. In particular, along the line (r, $\varphi = 45°$, z=constant) (see Figure 2.8), the components of the Lorentz force along the x and y axes are equal.

Due to the symmetry of the dual feed coupler setup, certain multipolar components cannot be excited in the structure: dipolar, sextupolar, etc. are not allowed. Nonetheless, there is a residual octupolar component in addition to the quadrupolar one. In order to fully evaluate the residual field asymmetries in the coupler region, the following function $F_\varphi(z)$ is introduced [28]:

$$F_\varphi(z) = [F_x(r = 5\,mm, \varphi = 45^\circ, z) - F_y(r = 5\,mm, \varphi = 45^\circ, z)] \tag{2.40}$$

This function is integrated along a line of length L, contained in the coupler region, parallel with the z-axis and specified by the cylindrical coordinates $r = 5\,mm$ and $\varphi = 45^\circ$. This yields the quantity:

$$k_q = \frac{1}{qr}\left|\int_0^L F_\varphi(z) e^{\pm j\frac{\omega}{c}z} dz\right| \tag{2.41}$$

In equation 2.41, the factor $e^{\pm j\frac{\omega}{c}z}$ takes into account the transit time effect, while the propagation velocity of the wave in the z-direction is intrinsic in the z-dependence of the phase of $F_\varphi(z)$. The values of k_q are also normalized to r in order to obtain a quantity that is no longer dependent on r (the integrand function is linear with respect to r).

2.3.1.2 Magnetic-coupled RF coupler

In the case of a magnetic-coupled RF coupler, the radio frequency power is transferred from a rectangular waveguide to an accelerating structure (operating on the TM_{01} mode) through a slot aperture between the wall of the rectangular waveguide and the coupling cell. In this case, the magnetic field in the waveguide is coupled to the magnetic field lines in the coupling cell [23, 29].

The RF coupler is matched to the accelerating structure by adjusting both the slot aperture and the radius of the coupling cell (respectively a and r in Figure 2.9). The coupling slot introduces a distortion in the field distribution, resulting in multi-pole field components which affect the beam dynamics. Using symmetric feeding, with two input waveguides on opposite sides of the coupling cell as indicated in Figure 2.10, the odd magnetic field components are suppressed, but there could still be even components like quadrupoles, octupoles, etc. [29]

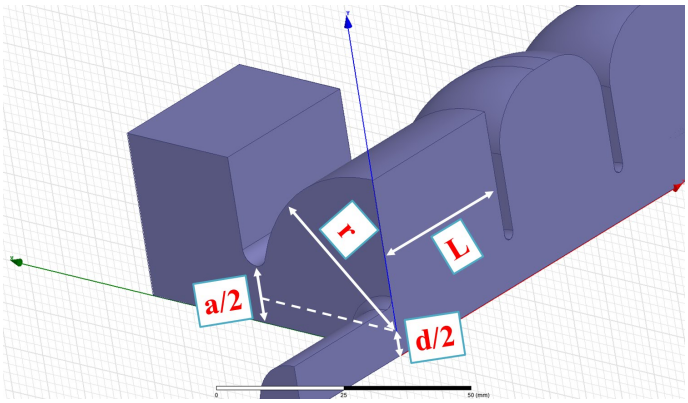

FIGURE 2.9: Geometrical parameters for the magnetic coupled RF coupler: a is the coupling slot aperture, d is the racetrack parameter and r is the coupling cell radius

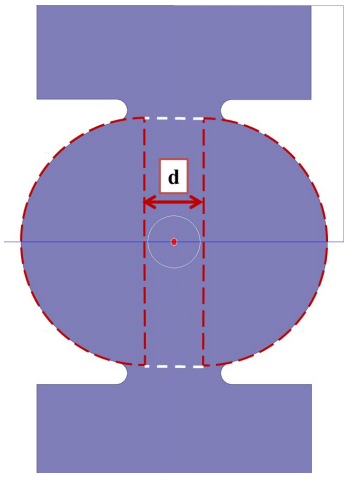

FIGURE 2.10: Racetrack profile for the magnetic coupled RF coupler

A racetrack profile of the coupler cell reduces the residual quadrupole component of the field [30, 31] by optimizing the distance d between the two half-circles, as shown in Figure 2.10.

In our case, the length of the coupler cell L is $34.036\,mm$ (Figure 2.9), exactly matching the short dimension of a WR284 rectangular waveguide. The residual quadrupole component has been calculated [32] as a function of the racetrack parameter d.

Figure 2.11 shows a plot of $G(z) = \Re\left[F_\varphi(z)e^{\pm j\frac{\omega}{c}z}\right]$ and $H(z) = \Im\left[F_\varphi(z)e^{\pm j\frac{\omega}{c}z}\right]$, respectively the real and imaginary parts of the integrand function of equation 2.41, for a structure consisting of three regular cells terminated with two RF couplers. Figure 2.11 shows that the major contribution to the quadrupolar kick acting on the beam comes from

the regions of the RF couplers, while no field asymmetry appears in the regular cells.

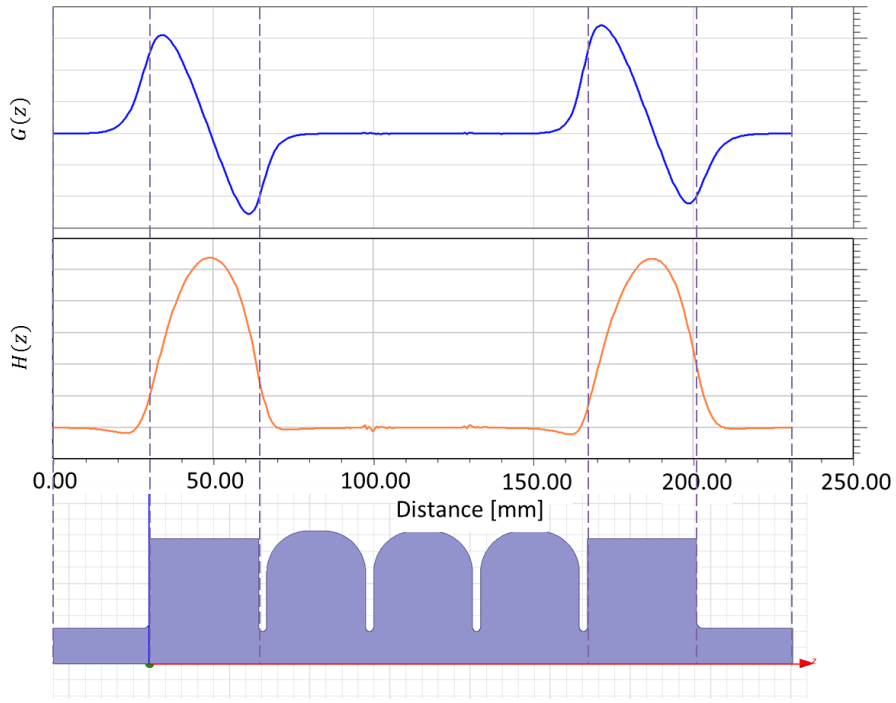

FIGURE 2.11: Plot of $G\,(z)$ and $H\,(z)$, the real and imaginary part, respectively, of the integrand function in equation 2.41

The racetrack parameters d, a and r are adjusted to obtain a reflection coefficient s_{11} at the input port of the coupler lower than *-30 dB*: couplers' geometric parameters have been tuned to match into the travelling wave structure by varying the number of regular cells between the two couplers [23]. Using this technique, we can verify that the results are not affected by any standing wave component still present in the structure.

Figure 2.12 shows the value of k_q as a function of the racetrack parameter d. In our case, the integration line extends from the entrance of the beam-pipe up to the end of the first regular cell. Note that the minimum of k_q is reached for $d = 13.5\,mm$.

After optimizing the racetrack geometry in terms of the residual quadrupole component, the surface electric and magnetic fields have been evaluated assuming an input power of $65\,MW$. This is, in fact, the power required to attain an overall accelerating gradient of $30\,MV/m$.

As it is evident from HFSS simulations (see Figure 2.13), the axial electric field is slightly higher in the coupler region than in the regular cells for such a coupler.

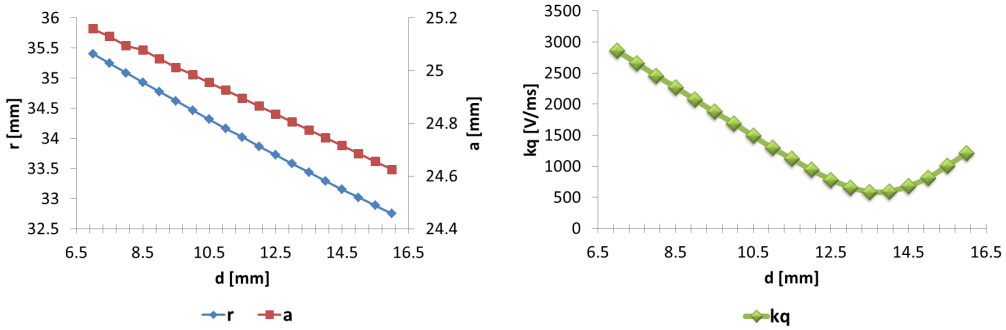

(a) Slot Aperture a and Coupler Cell Radius r vs Racetrack Parameter d

(b) k_q vs Racetrack Parameter d

FIGURE 2.12: Parameters of an MC-Coupler as a function of the racetrack parameter

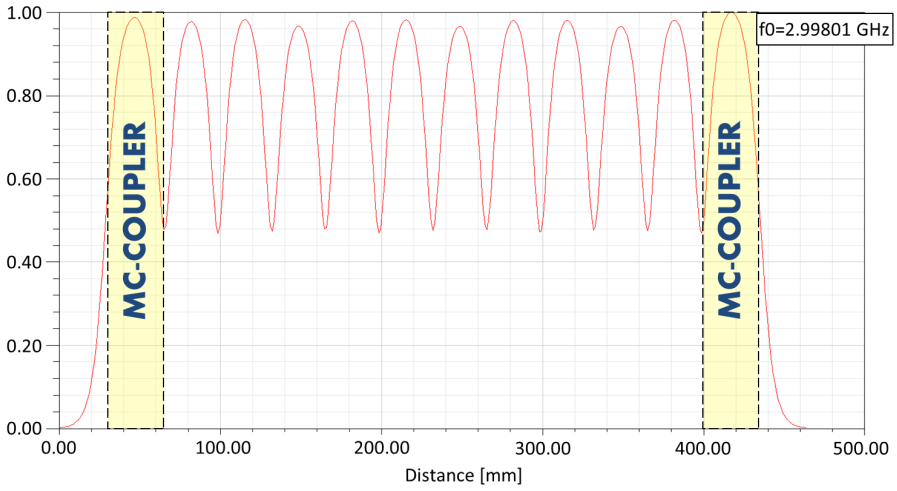

FIGURE 2.13: Axial electric field E_z for a 10 cells accelerating structure

The surface electric field achieves its maximum value of 93 MV/m on the first beam iris (see Figure 2.14). The surface magnetic field reaches its maximum value in the coupling slot region. By smoothing all the sharp edges connecting the waveguide to the coupler cell, it is possible to get a surface magnetic field H_{surf} as low as 175 kA/m, thus reducing the possible detrimental effects due to the pulse heating phenomena.

Limitations coming from RF breakdown in vacuum strongly influence the design of high gradient accelerating structures. As shown in the previous section, the so called modified Poynting vector has been introduced [19] to evaluate the high gradient performance limit of accelerating structures in the presence of vacuum RF breakdown.

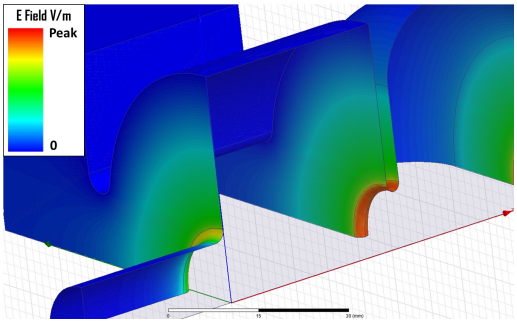

(a) Surface electric field

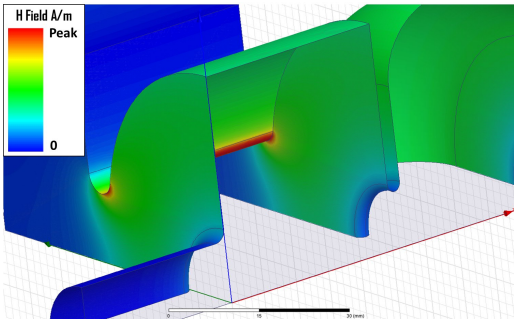

(b) Surface magnetic field

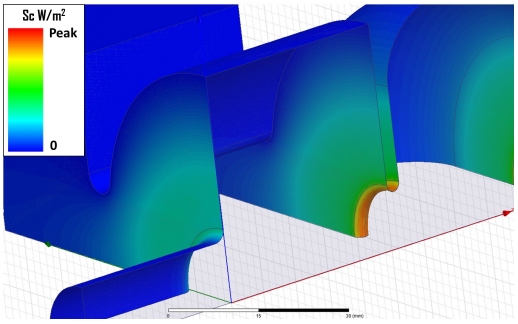

(c) Modified Poynting vector

FIGURE 2.14: Surface fields for an MC-coupler

According to the simulation results, for such an RF coupler the maximum value of $|S_c|$ is nearly $0.7\ MW/mm^2$. Considering the experimental data collected at CERN in the framework of the CLIC study [19], this value of S_c results in a breakdown rate (i.e. number of breakdowns per pulse per meter, measured in bpp/m) of nearly $10^{-15}\ bpp/m$ if operating with an RF pulse of $700\,ns$ and a gradient of $30\ MV/m$.

2.3.1.3 Electric-coupled RF coupler

Magnetic couplers presented above have been widely studied and used in accelerator design. However, in the development of high gradient accelerating structures, the high electromagnetic fields arising in magnetic-coupled couplers could indeed represent a bottleneck. To remove possible limitations to the achievable values of the gradients, novel changes in the couplers'design have been introduced and different solutions have been studied in depth [22, 23]. Among all the modifications explored, waveguide couplers showed a clear and significant reduction of coupler surfaces fields.

As clearly explained in [22, 23], for a waveguide coupler the input power coming from the source is directly coupled to the accelerator through a circular iris in the broad wall of the WR284 waveguide. The electric coupling requires a matching cell to match the input waveguide to the periodic structure (see Figure 2.15).

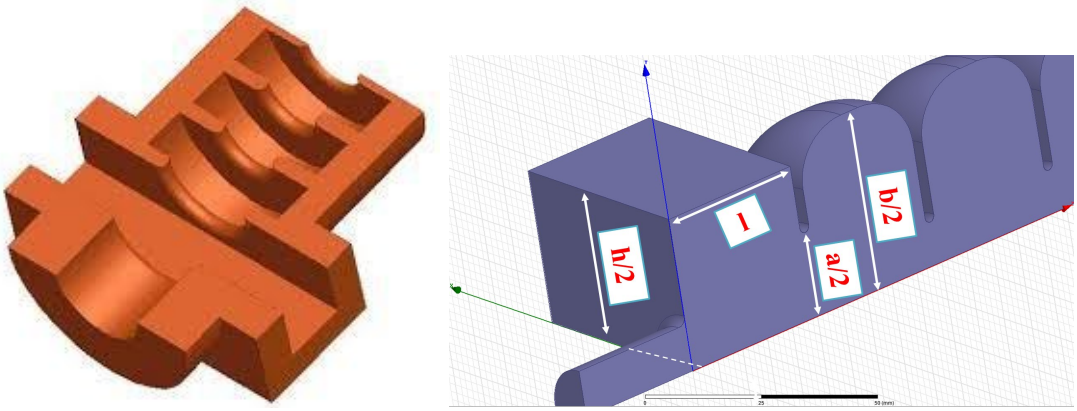

(a) Cut of an EC-coupler (b) Geometrical parameters of an EC-coupler

FIGURE 2.15: Layout of a waveguide coupler:h is the length of the waveguide broad wall, l is the length of the waveguide narrow wall, a is the diameter of the beam iris and b is the outer diameter of the matching cell

As it can be seen from Figure 2.16, the waveguide coupler (EC-coupler) sacrifices some acceleration efficiency. In the waveguide region the E_z field component is very low (see Figure 2.16 where a 10 cells accelerating structure has been considered). Furthermore, in the matching cell the field may not be properly phased with the following accelerating cells. In our case, the accelerating efficiency has been partially improved by stepping down the narrow size l of the WR284 rectangular waveguide to 60% of its original length.

The value of the residual quadrupole component k_q, evaluated according to equation (2.41), has been then calculated by considering the exponential factor $e^{+j\frac{\omega}{c}z}$ and an integration line that extends from the entrance of the beam-pipe up to the end of the matching cell.

For a standard WR284 input waveguide, the resulting k_q is higher if compared to the residual head-tail kick achievable with an optimized MC-coupler. An improvement can be obtained by varying the geometric parameter h, and analyzing the effect on the head-tail kick. Such analysis has been carried out by using the commercial software HFSS: of course, for each value of the parameter h, the optimal values of a and b have been found in order to guarantee a value of the $|s_{11}|$ lower than $-30\,dB$.

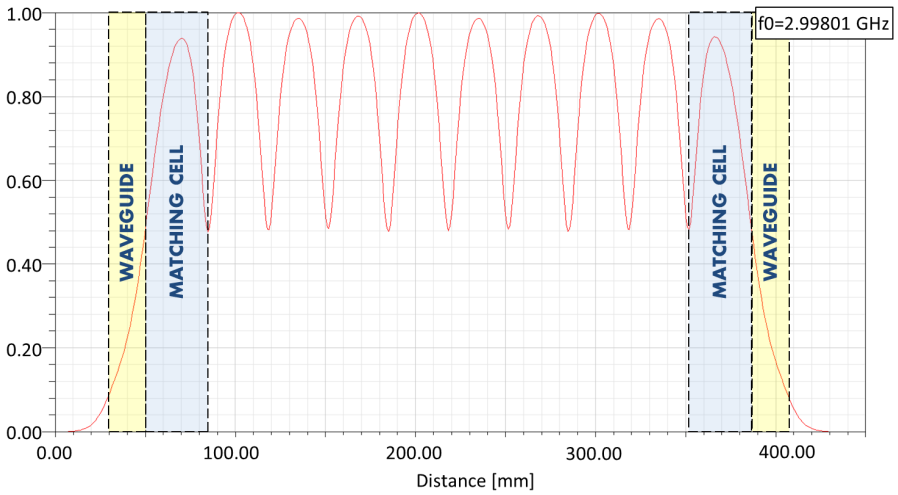

FIGURE 2.16: Axial electric field E_z for the considered accelerating structure composed of 10 cells

As illustrated in Figure 2.17, by tuning the length of the waveguide broad wall h, the residual quadrupole strength k_q can be slightly reduced. The optimal value is attained when h is approximately equal to $100\,mm$. Nonetheless, such a value is still nearly four times the optimal value that could be attained with an optimized MC-coupler.

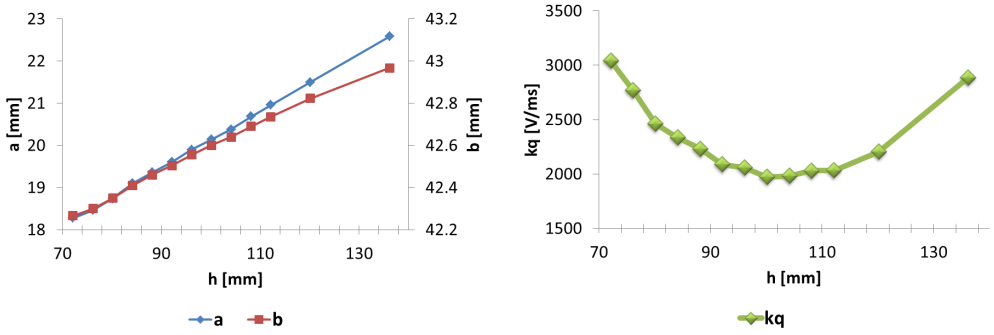

(a) Slot Aperture a and Coupler Cell Radius r vs waveguide width h

(b) k_q vs waveguide width h

FIGURE 2.17: Parameters of an EC-Coupler as a function of the waveguide width

The surface fields, as well as the modified Poynting vector, have also been evaluated in the EC-coupler for an input power of $65\,MW$.

The surface electric field has its maximum value, of about $81\,MV/m$, on the first beam iris. Also, as illustrated in Figure 2.18, the surface magnetic field H_{surf} in the coupler

region is much lower than the one in the successive cells, where the maximum value is about $78\,kA/m$.

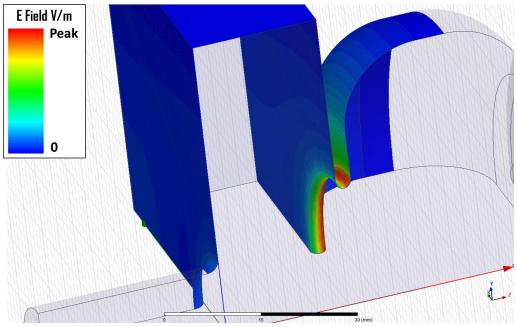

(a) Surface electric field

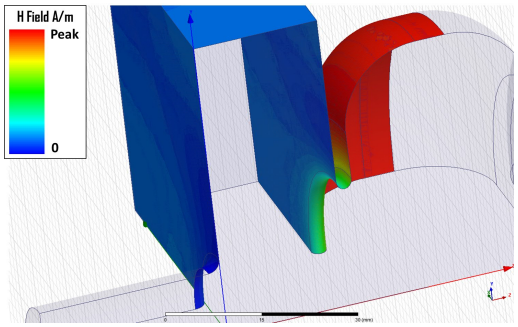

(b) Surface magnetic field

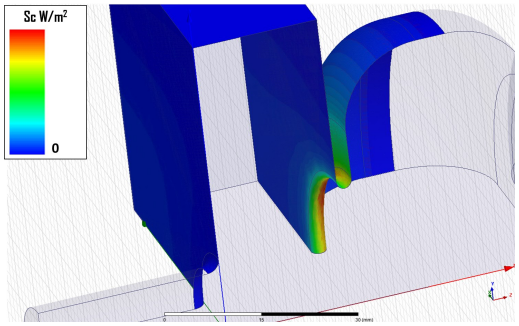

(c) Modified Poynting vector

FIGURE 2.18: Surface fields for an EC-coupler

Considering that for the previously considered MC-coupler the surface magnetic field in the coupling slot region was approximately $175\ kA/m$, it is quite evident that the limitations to high gradient operation due to RF pulse heating phenomena can be easily reduced.

Also, the value of the modified Poynting vector is a bit lower compared to the one obtained for an MC-coupler. For our EC-coupler, the maximum value of $|S_c|$ is in fact nearly $0.57\ MW/mm^2$. Based on experimental evidence, this results in a breakdown rate probability of approximately $10^{-16}\ bpp/m$ if operating with an RF pulse of $700\ ns$.

Table 5.1 summarizes and compares the performances of electric-coupled and magnetic-coupled RF coupler. As it can be seen, electric-coupled RF couplers show a lower value for S_c and the expected breakdown rate. EC-couplers show also a significant reduction of the magnetic surface fields, and therefore no limitation would arise due to field enhancement or RF pulse heating.

TABLE 2.1: Summary of RF parameters for both Electric Coupled and Magnetic Coupled RF couplers. All the field values are calculated for 65 MW of input power

	E_{surf} $[MV/m]$	H_{surf} $[kA/m]$	S_c $[MW/mm^2]$	BDR $[bpp/m]$	k_q $[V/ms]$	Pros	Cons
MC Couplers	93	175	0.7	10^{-15}	582	Lower residual quadrupole field components. Acceleration efficiency.	High magnetic field at the coupling slot.
EC Couplers	81	78	0.57	10^{-16}	1973	Very low surface magnetic field. Easy to machine. Cost reduction.	Higher residual quadrupole field components. Slightly reduced acceleration efficiency.

Nonetheless, a drawback of EC-couplers is in general a reduction of the acceleration efficiency. Even stepping down the narrow size of the WR284 rectangular waveguide, the acceleration efficiency in the coupler region for a particle travelling on-crest is reduced by about 40% compared to the MC-coupler. Of course, considering the whole length of the structure, the total energy loss over $3m$ is less than 1% and can generally be compensated by operating at slightly higher power without reaching any breakdown limitations.

It must also be considered that the residual quadrupole field component is not as low as in the MC-couplers case. This makes the EC-couplers more suitable for use in the high energy part of a linear accelerator, where the e-beam is already compressed and its longitudinal momentum is high enough to not be affected by the quadrupolar kicks coming from the couplers' region.

Based on all the previous considerations, the electric-coupled solution was adopted for the design of the novel accelerating structures.

2.3.2 Accelerating cells design

Since the accelerating module has to replace an existing BTW, the most stringent requirement comes from the available space for each module [33]. The available length for acceleration (not including input and output couplers) is 3.0 meters, and the target is a reliable accelerating gradient of 30 MV/m. Real challenge in the design was that of having the required accelerating gradient given a fixed length and RF power, and with lower wakefields compared to the BTW structures. These constraints indirectly fixed all RF parameters of the accelerating structure thus making the design process quite tricky. It was

calculated that 90 accelerating cells, each of 33.332 mm length, can be accommodated in 3.0 meters space.

Each regular accelerating cell (shown in Figure 2.19), with a phase advance of $2\pi/3$, has a disk thickness *t* of 2.5 mm and a rounded geometry, with the outer bending radius *or* of 13 mm. This allowed to achieve higher shunt impedance and quality factor of 15800 [34]. A constant accelerating gradient along the structure is maintained by designing the cells according to the following condition [35]:

$$v_{g,i} = \frac{\omega_0 L_{structure}}{Q_0} \frac{\left[1 - \left(1 - e^{-2\tau}\right) \frac{(i-1)L}{L_{structure}}\right]}{(1 - e^{-2\tau})} \tag{2.42}$$

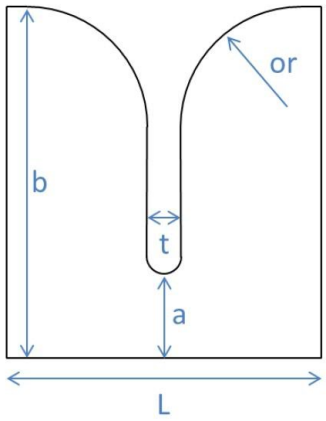

FIGURE 2.19: Sketch of a regular cell

where $v_{g,i}$ is the group velocity for the *i*-th cell, Q_0 the average quality factor of the structure, L the length of a regular cell, $L_{structure}$ the length of the structure and τ the structure's attenuation parameter.

The attenuation parameter τ for the structure is 0.385 Neper. This value was dictated by the requirement of a short filling time of 650 ns for an efficient RF pulse compression. Once τ is known, the group velocity for each cell is calculated by equation 2.42. All other structure parameters, such as the iris radii *a*, and the outer radii *b* are numerically calculated by means of SUPERFISH [36], to match the desired resonant frequency. Figure 2.20 shows the group velocity and the shunt impedance along the structure.

To achieve a 1.8 GeV beam energy, the operating gradient shall be raised up to 30 MV/m, which is remarkably higher than the gradient of the BTW and of other typical S-band TW structures. Such high gradient, with μs pulse length, is not easy to realize because of RF breakdown phenomena.

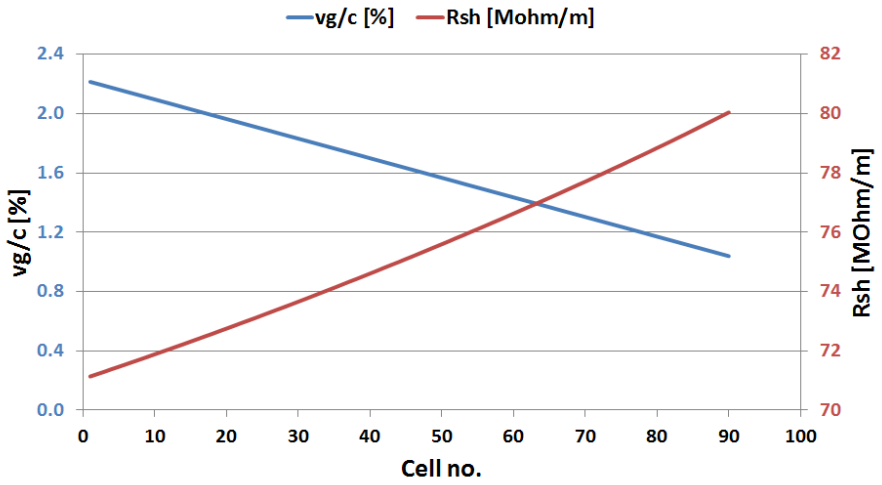

FIGURE 2.20: Group velocity and Shunt Impedance vs the cell number

In order to lower the peak electric field in the cell, an elliptical rounding at the iris has been introduced. HFSS [32] simulations have been performed and different iris shapes have been compared in terms of both peak electric field and modified Poynting vector, as shown in Figure 2.21: based on these results, a semi-major axis of 1.45 mm has been chosen while the semi-minor axis is 1.25 mm long, one-half of the disk thickness t. Table 5.2 summarizes the RF parameters of the new HG (High Gradient) structure.

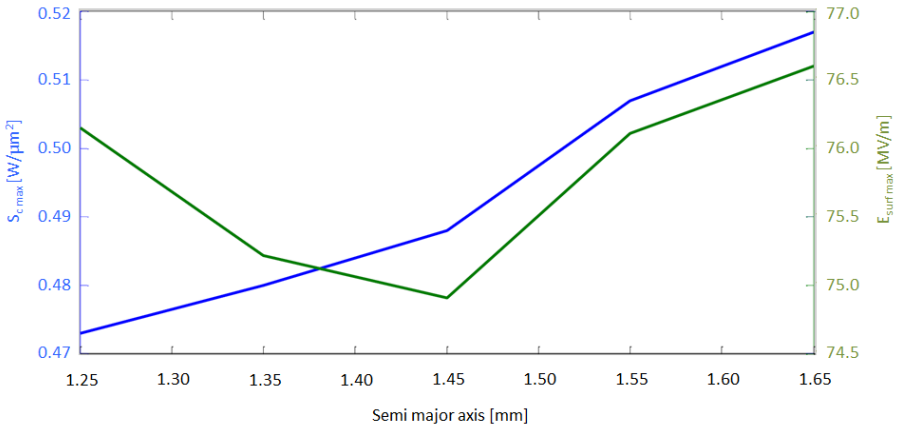

FIGURE 2.21: Maximum electric surface field (blue) and modified Poynting vector (green) at the iris of the first regular cell as a function of the elliptical shape

Cell surface fields and modified Poynting vector have also been calculated and compared with those of a BTW regular cell at a common gradient of 24 MV/m. In both cases, the

first regular cell has been considered. Field profiles are shown in Figures 2.22, 2.23 and 2.24, while numeric values are reported in Table 2.3.

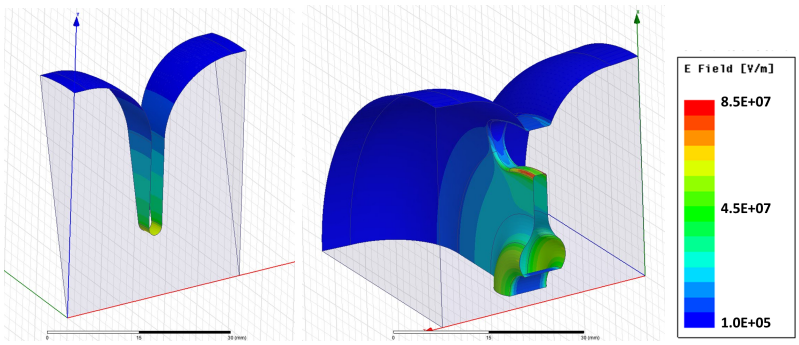

(a) HG cell (b) BTW cell

FIGURE 2.22: Surface electric field profile for the HG and the BTW first regular cell

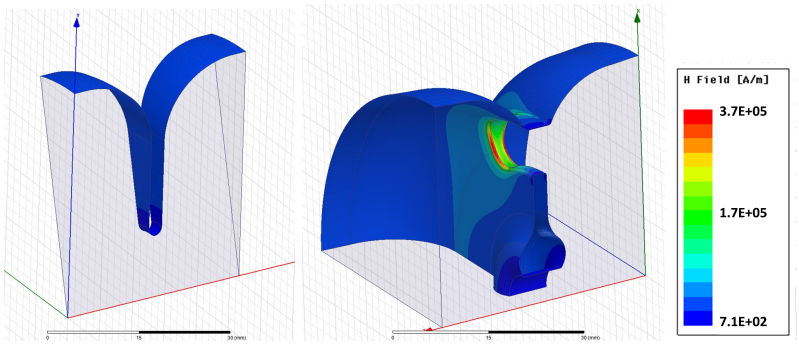

(a) HG cell (b) BTW cell

FIGURE 2.23: Surface magnetic field profile for the HG and the BTW first regular cell

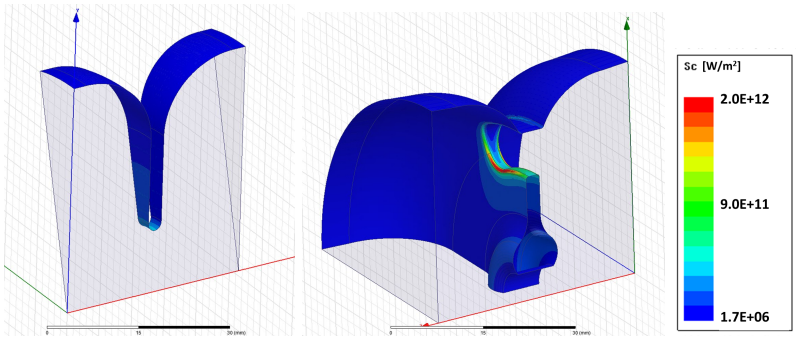

(a) HG cell (b) BTW cell

FIGURE 2.24: Modified Poynting vector profile for the HG and the BTW first regular cell

TABLE 2.2: RF parameters of the accelerating structure

f_0	2998.01	MHz
$Mode$	$2\pi/3$	
$L_{structure}$	3175	mm
L_{cell}	33.332	mm
N_{cell}	90	
$a\ (iris)$	$11.38 \rightarrow 8.98$	mm
$b\ (cell\ outer\ radius)$	$41.61 \rightarrow 41.11$	mm
$t\ (disk\ thickness)$	2.5	mm
$or\ (outer\ bending\ radius)$	13	mm
R_{sh}	$71 \rightarrow 80$	$M\Omega/m$
Q_0	≈ 15850	
v_g/c	$2.21 \rightarrow 1.04$	
t_f	645	ns
τ	0.38	$Neper$

TABLE 2.3: RF parameters for the first regular cells

	HG	BTW	
$Acc.\ Gradient$	24	24	MV/m
$RF\ Pulse\ length$	670	770	ns
$E_{surf,\ Max}$	62	85	MV/m
$H_{surf,\ Max}$	54	368	kA/m
$S_{c,\ Max}$	0.36	2.1	MW/mm^2
BDR	$8.7 \cdot 10^{-20}$	$5.4 \cdot 10^{-8}$	bpp/m

As it is evident, for the BTW structure both the electric and the magnetic fields are enhanced in the coupling slot region. In particular, surface magnetic field rises up to 368 kA/m, thus resulting in an excessive pulse heating which degraded the cavity surface quality [12], as shown in Figure 2.25.

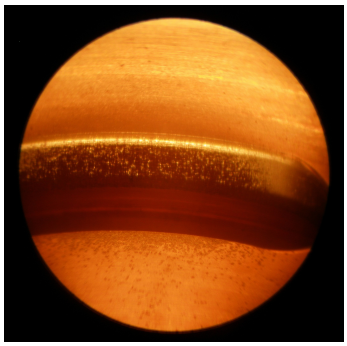

FIGURE 2.25: Surface degradation around the coupling slot of a BTW

As reported in Table 2.3, in the new design the surface magnetic field will be approximately 7 times lower, so no limitation due to pulse heating phenomena will occur. According to the criterion defined in the frame of the CLIC X-band high gradient program by CERN-SLAC-KEK [19], the expected breakdown rate has also been evaluated: in particular, the value of $|S_c|$ will result in a breakdown rate probability of nearly $8.7 \cdot 10^{-20} bpp/m$ at 24 MV/m and $1.4 \cdot 10^{-16} bpp/m$ at a gradient of 30 MV/m.

2.3.3 Input and output couplers matching

As already explained, the RF coupler is the region most prone to RF breakdown [20, 21]. So, in the previous section, two possible solutions for RF power couplers have been investigated. An electric coupled solution (EC-coupler) [22, 23] presents very low surface fields at the cost of a reduced acceleration efficiency. Lower surface currents produce lower pulse heating, thus improving its reliability and power handling capability. Loss of acceleration efficiency can be instead compensated by 60% reduction in dimensions of the narrow size of WR284 rectangular waveguide. For the above mentioned reasons, the EC solution has been adopted.

Matching cells for both input and output couplers are designed to maintain nearly a constant gradient throughout the structure. So the iris size is varied to modify the group velocity, in order to have constant gradient and proper matching conditions. Usually, the coupler design requires a simulation of the whole structure, which is computationally

TABLE 2.4: Geometric and RF parameters of the input coupler for the symmetrized model

a_m	20.143	mm
b_m	42.758	mm
s_{11}	-62	dB
$Bandwidth\ BW$	± 2	MHz
$ReturnLoss\ in\ BW$	≥ 30	dB

very expensive. An alternative way to solve this problem is to artificially symmetrize the model [23], to match input and output coupler separately as shown in Figure 2.26.

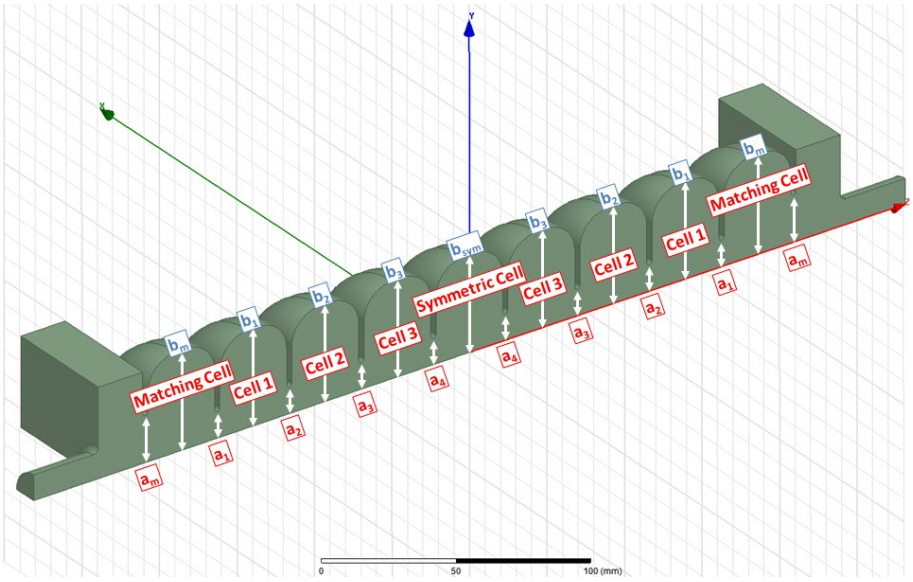

FIGURE 2.26: Symmetrized model for coupler matching

The symmetrized model in Figure 2.26 for input coupler design consists of first three regular cells, which are mirrored by using one *symmetric cell* and two matching cells. The irises of the *symmetric cell* are matched with the regular cells while outer diameter is adjusted to compensate for frequency. The number of *symmetric cells* is varied from one to three to make sure that no standing wave component arises in the traveling-wave structure after the matching of the coupler. Geometric parameters for matching cells, calculated to minimize $|s_{11}|$, and RF parameters for the input coupler are listed in table 2.4.

Matching parameters for the output coupler are found using the same procedure but with an additional condition of field flatness. In fact, as it is evident from Figure 2.27,

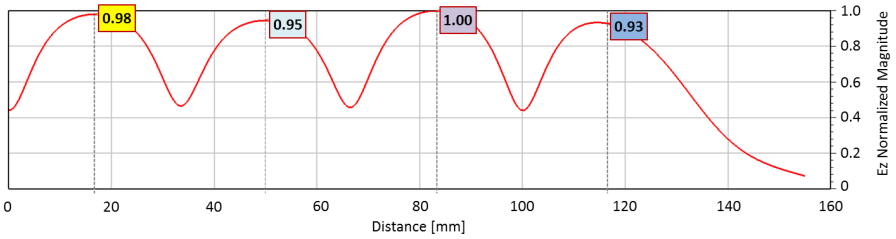

FIGURE 2.27: Normalized amplitude of the longitudinal electric field $|E_z|$ in the last cells

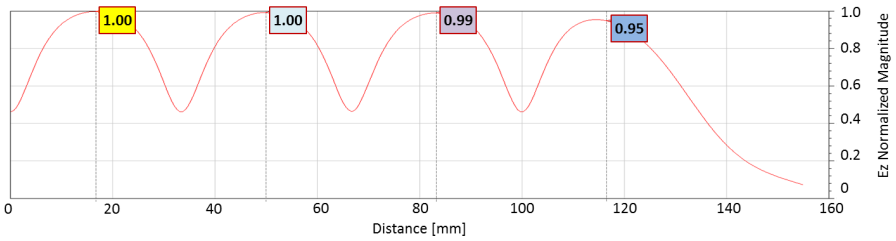

FIGURE 2.28: Normalized amplitude of the longitudinal electric field $|E_z|$ in the last cells after VSWR optimization

the reduction of $|s_{11}|$ at the output port is not sufficient to assure an acceptable matching: the poor field flatness shows that a standing wave pattern is still present in the structure and needs to be minimized. A rather better matching (and improved field flatness) can instead be attained by minimizing the standing wave ratio (VSWR) as shown in Figure 2.28.

TABLE 2.5: Geometric parameters for the output coupler

a_m	17.607	mm
b_m	42.062	mm

Geometric parameters of the output matching cell are listed in table 2.5.

3 Beam Dynamics Study

3.1 Interaction of beams with surroundings

The core of an accelerator, the part which is in the closest proximity to the beam of accelerated particles, is the vacuum vessel. Its design and materials may be quite different in various accelerators, but the main components are usually the same: beam pipes with expansion bellows, connection flanges and pumping ports, accelerating RF cavities, collimators, monitors and similar beam handling equipments.

A charged particle beam generates electromagnetic fields at any cross-section variation of the vacuum vessel, whether it is abrupt or a gradual transition, only the strength of the interaction will be different [37, 38]. These fields may be trapped or propagated in the vacuum chamber but, in any case, they react back on the beam and interact with the elements of the vacuum chamber.

Generally the electromagnetic fields generated by the beam contain three spatial components. These are usually classified as longitudinal (i.e. directed along the particle motion), and transverse (horizontal and vertical, or radial and azimuthal). The longitudinal component of the electric field may change the effective amplitude and phase of the applied accelerating field, and thereby the rate of acceleration, as well as the energy distribution in the bunch and its effective length. Similarly, transverse field components may increase the cross section of a bunch. These effects become more severe at higher beam currents.

The interaction of an electromagnetic field with charged particles is most effective when one of the field components has a phase velocity v_{ph} close to the particle velocity. Such a field component is called *synchronous* and the strength of the interaction can be characterized by the *coupling impedance* [37, 38]. Other important considerations are the effects of the induced electromagnetic fields on elements of the vacuum chamber. High intensity fields can excessively heat sensitive elements close to the beam, and this may even destroy them, in some cases, or produce undesirable increase in vacuum pressure. The

generation of electromagnetic fields by the beam also increases the required power output of the RF generators.

Particles which are lost from the beam due to induced fields may hit the walls of the vacuum chamber and thereby produce excessive radiation.

For all these reasons, the elements of the vacuum chamber should be designed to *minimize* their coupling impedance.

3.2 Wakefields

When traversed by charged particles, cross section variations of the vacuum chamber generate electromagnetic fields which are called *wakefields* since they remain usually behind the (ultra-relativistic) exciting particles [37]. These wakefields can influence the motion of trailing particles, in the longitudinal and in one or both transverse directions. This may lead to *energy loss*, to *beam instabilities*, or produce undesirable secondary effects such as excessive heating of sensitive components at or near the chamber wall. Without a knowledge of these wakefields and of their interactions, an accelerator can therefore hardly be operated at the desired top performances.

The normalized integral of the electromagnetic force due to fields excited by a point charge or *delta function distribution* is called the *wake function*. It is a function of the distance between the exciting and test charges. Since it is the response to a delta function excitation, it is also a *Green function* for the structure investigated. In the limit $v \to c$, the *wake function* depends only on the surrounding structure. The *longitudinal wake function* is defined as:

$$G_{\parallel}\left(r_b, r_e, z\right) = \frac{1}{q}\int_{-\infty}^{s} E_z\left(r_b, r_e, z\right) dz, \tag{3.1}$$

where r_e and r_b are the lateral deviation of the test charge and the exciting charge, respectively, from the structure electric axis.

The *transverse wake function* is the integral of the transverse electromagnetic forces along a straight path at the distance s behind an exciting point charge and divided by the value of the charge:

$$G_{\perp}\left(r_b, r_e, z\right) = \frac{1}{q}\int_{-\infty}^{s} \left(E\left(r_b, r_e, z\right) + v \times B\left(r_b, r_e, z\right)\right)_{\perp} dz, \tag{3.2}$$

On the other hand, the integrated effect over a finite distribution of charged particles is described by the *wake potential*. Using the superposition property of the (linear) Maxwell equations, the wake potential can be determined by the convolution of the wake function with the charge distribution in the bunch. Consequently, the wake potential depends not only on the structure, but also on the charge distribution which excites it.

The longitudinal wake potential $W_{\parallel}(s)$, measured in V/C, of the longitudinal wake function $G_{\parallel}(s)$ with the (arbitrary) longitudinal charge distribution $\lambda(s)$ is:

$$W_{\parallel}(s) = \frac{1}{Q}\int_{-\infty}^{s} G_{\parallel}(s-s')\lambda(s')ds', \tag{3.3}$$

where Q is the total bunch charge in units of C:

$$Q = \int_{-\infty}^{\infty} \lambda(s)ds \tag{3.4}$$

The bunch energy loss induced by the longitudinal wakefield is called loss factor k, and is measured in V/C:

$$k = \frac{1}{Q}\int_{-\infty}^{\infty} \lambda(s)W_{\parallel}(s)ds \tag{3.5}$$

In an analogous way, and with symmetric notation for the transverse planes of motion in a cylindrically-symmetric RF structure, the transverse wake potential $W_{\perp}(s)$, measured in V/Cm, is given by:

$$W_{\perp}(s) = \frac{1}{Q}\int_{-\infty}^{s} G_{\perp}(s-s')\lambda(s')ds' \tag{3.6}$$

The kick factor $k_{\perp}$, measured in V/Cm, is defined as:

$$k_{\perp} = \frac{1}{Q}\int_{-\infty}^{\infty} \lambda(s)W_{\perp}(s)ds \tag{3.7}$$

The structure impedance is the Fourier transform of the wake potential normalized to the Fourier transform of the bunch charge distribution function. For the longitudinal and the

transverse impedance, measured in Ω, we have, respectively:

$$Z_{\parallel(\omega)} = \frac{\int_{-\infty}^{\infty} W_{\parallel}(s)e^{-j\omega s}ds}{\int_{-\infty}^{\infty} \lambda(s)e^{-j\omega s}ds} \tag{3.8}$$

and

$$Z_{\perp(\omega)} = \frac{\int_{-\infty}^{\infty} W_{\perp}(s)e^{-j\omega s}ds}{\int_{-\infty}^{\infty} \lambda(s)e^{-j\omega s}ds} \tag{3.9}$$

For most practical purposes, the charges are measured in pC instead of C, and the wake potentials are normalized with the wake integration length resulting in V/pCm units for the longitudinal wake potential, and V/pCm^2 for the transverse wake potential.

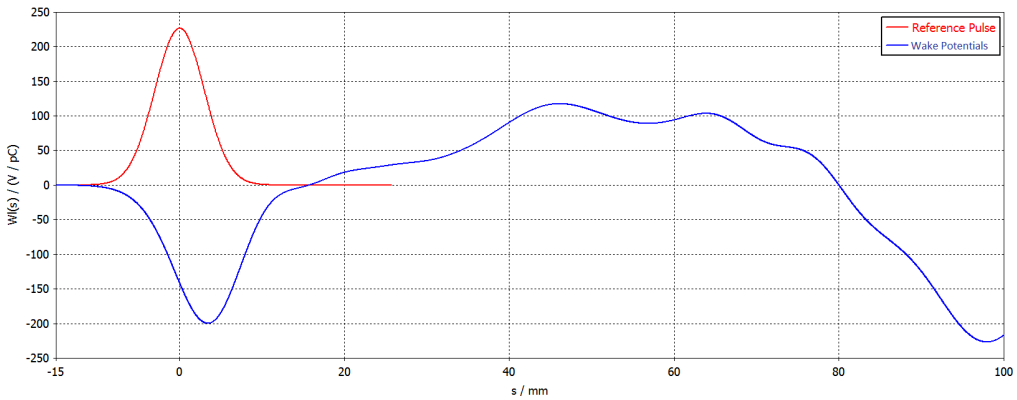

FIGURE 3.1: Longitudinal wake potential of the new high gradient accelerating structure for FERMI linac upgrade, evaluated for a 3 mm long Gaussian bunch. The bunch (in red) is superimposed to the wake, the bunch head is on the left.

3.2.1 Numerical evaluation

In order to determine a wake function one needs solutions for the propagation, diffraction and interference of the electromagnetic fields radiated by the beam, which requires solving the inhomogeneous Maxwell equations involving the source terms with the appropriate initial and boundary conditions [37]. Analytical solutions are possible only for a very limited number of simple geometries, such as closed cylindrical cavities. In most practical cases, one has to employ numerical methods using computers. One can distinguish between codes working directly in the time domain, and those which first compute

resonant modes in the frequency domain, from which the wakefields can be subsequently obtained.

Computer codes which solve the Maxwell equations in the time domain can only calculate fields excited by distributions of finite length (i.e. bunches of particles). In all these codes the bunch length must be a multiple (typically 5 times or more) of the longitudinal mesh size, and hence the wake functions of point charges cannot be computed exactly. One can obtain a rough approximation of the wake function by determining the wake potential of a very short bunch. This requires correspondingly small mesh sizes, but the number of mesh points is usually limited by the computer memory available, and this may be a serious problem for large structures. Thus, the computation of the wake function just behind the point charge can only be obtained with different procedures.

In the frequency domain the wake functions can be approximated by computing a sufficiently large number of resonances of a structure. However, this technique has the drawback that only a finite number of resonances can be computed in any given time.

Wake potentials are convolutions of wake functions with the particle distribution, hence it is worth trying to obtain the wake functions simply by a deconvolution. Unfortunately, this cannot be performed without severe loss of accuracy in the regions outside the bunch [37].

Nonetheless, there are few well established techniques to solve the above mentioned problems, and to estimate the wake functions in the range where simulations are not possible due to mesh limitation. One of such numerical approaches was adopted for the new FERMI structures, calculating first the wake potential, and then the wake function. The results are also compared with an analytical model [39] well-established in the literature.

3.2.2 Numerical tools

Several well-developed codes are available for the numerical evaluation of the wakefields in the time domain: Gdfidl Echo [40], ABCI [41], and CST [42] are the most commonly used tools in the particle accelerator community [43].

ABCI is a $2D$ computer program which has wide acceptability in accelerator community, due to its high speed of execution, minimum use of computational resources, and different options available for Fourier transform and integration, such as the Napoly integration method. This method improves the calculation of wake potentials in structures,

such as collimators, where parts of the boundary extend below the beam pipe radius. The conventional integration method at the radius of the beam pipe breaks down when a part of the structure comes down below it, or when the radii of the two beam pipes at both ends are unequal. Napoly's integration method is a solution to this classical problem since it eliminates the contribution from the outgoing beam pipe [44].

A portion of the 90 cells structure entered in ABCI is shown in Figure 3.2. The parametrization of the single regular cell is shown in Figure 3.3. The choice of the bunch length is a critical parameter, since it is directly related to the mesh generation, which in turn affects computational time and resources, and stability of simulation. Due to the fact that the smaller the bunch length is, the denser the mesh is required, we found difficult to simulate bunch lengths in the range of micrometers. At the same time, the bunch length defines the range of frequencies that will be excited in the structure at its passage. As an example, it was found by convergence studies that the choice $\sigma_z = 3\ mm$, which translates to a frequency scale around 35 GHz, is sufficient for a reliable wakefield simulation in the whole structure.

Wake potentials were in fact calculated for rms bunch lengths in the range 0.4–5.0 mm, where the length of the bunch to pass through the new FERMI structures is of the order of 0.1 mm.

The CST wakefield solver is a $3D$ tool that is basically an extension of a time domain solver for special current excitations. One most important feature of CST is its robustness, which is due to different available integration techniques. A portion of the structure modelled in CST is shown in Figure 3.4. Also in this case the value $\sigma_z = 3\ mm$ allows to limit the number of mesh cells to a practical value, as shown in Figure 3.5. By exploring the $3D$ capabilities of this code, an *off-axis* beam was specified in the cavity, while an *on-axis*, wakefield integration line was selected. This allowed the study of both the longitudinal and the transverse wakefield with a single simulation set up.

In general, it is recommended to keep the length of the beam pipe, at both ends of the structure, at least as twice as the so called wakefield catch up distance D, which is the minimum length required for the field excited at the edge of a disk to affect the incoming particles, and can be estimated mathematically as $D \geq \frac{a^2}{2\sigma_z}$ [45], where a is the cell iris radius. The maximum value of a is 11.382 mm, so that D must be larger than 22 mm for $\sigma_z = 3\ mm$.

The beam pipe was extended to 80 mm at both ends of the structure accordingly. Open boundary (i.e., perfectly matched) conditions of CST were used at both ends for allowing the e.m. waves to be fully absorbed.

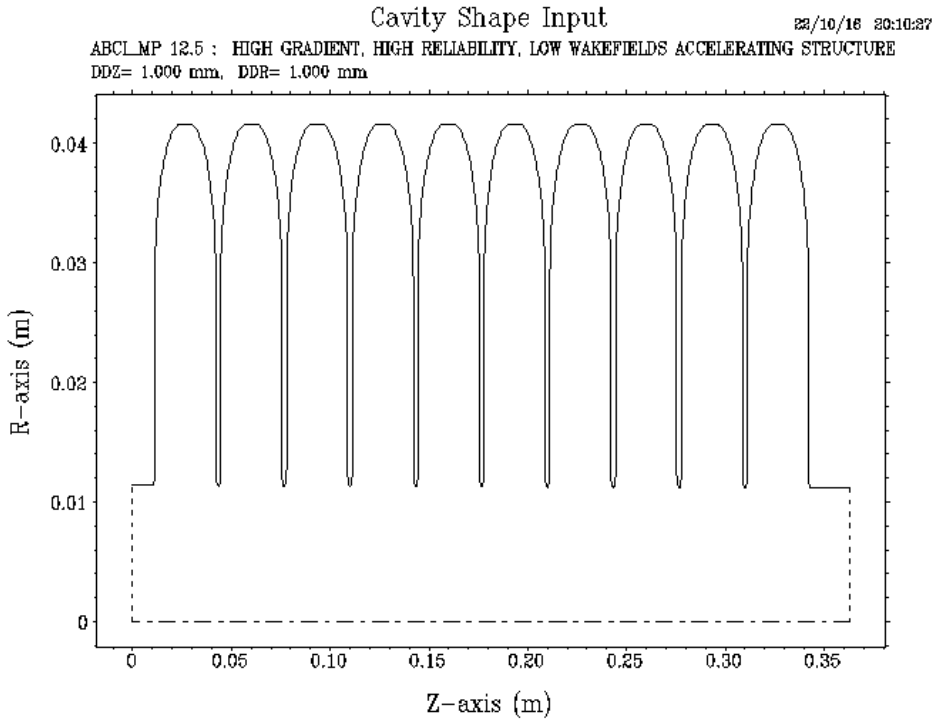

FIGURE 3.2: $2D$ modeling with ABCI of a portion of the new RF structure.

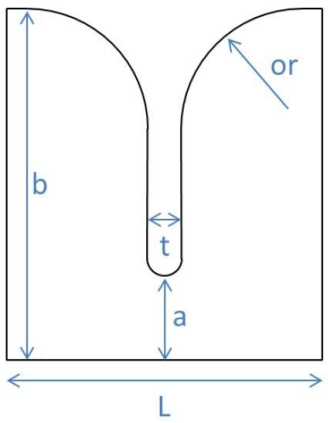

FIGURE 3.3: Single regular cell geometry.

The CST result was compared with that obtained by ABCI. From the computational point of view, a marked difference was found in both the simulation time and the RAM requirements of the two software products. For the simulation of the full 90 cells structure traversed by a 3 mm rms long bunch, ABCI simulation took 36 hours for both longitudinal and transverse wakefield simulation, CST required 194 hours.

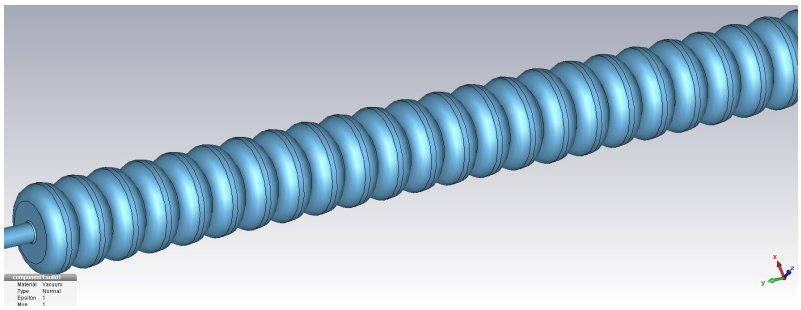

FIGURE 3.4: $3D$ modeling with CST of a portion of the new RF structure.

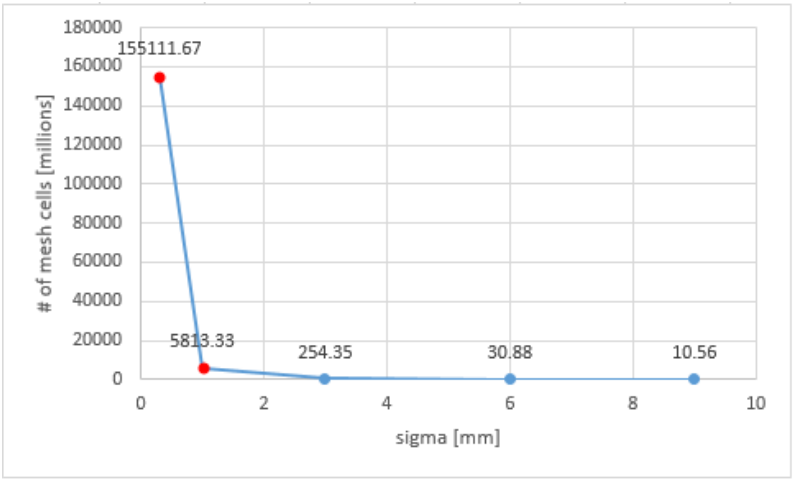

FIGURE 3.5: Number of mesh cells required by CST vs. rms bunch length.

Longitudinal and transverse wake potentials calculated with ABCI and CST are shown in Figures 3.6(a) and 3.6(b).

These figures show a good agreement between the transverse wake potentials calculated with the two software, along the whole structure and for $\sigma_z = 3\ mm$. The loss factor and the kick factor provided by the two codes are also sufficiently close to each other, as shown in Table 3.1.

Software	Loss Factor (V/pC)	Kick Factor $(V/pC/mm)$
CST	1.29×10^2	5.38
ABCI	1.38×10^2	5.68

TABLE 3.1: Wakefield Loss Factor and Kick Factor of the new RF structures, from ABCI and CST.

Figure 3.6(b) highlights the damping of the High Order Modes (HOMs) associated to

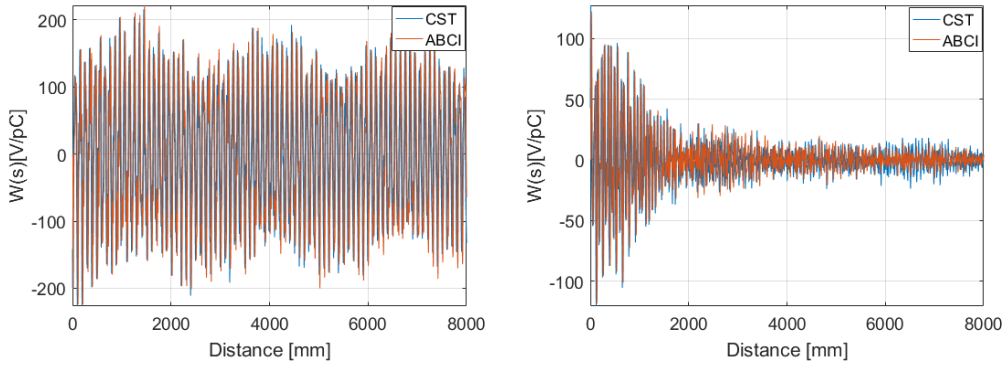

(a) Longitudinal wake potential. (b) Transverse wake potential.

FIGURE 3.6: Comparison of the wake potentials calculated with ABCI and CST

the transverse wake potential. Such a damping is not present in the longitudinal plane. Here, the accelerating fundamental mode at 2.998 GHz is the most strongly coupled one, as expected and shown in Figure 3.7.

In order to reveal the HOMs contribution to the longitudinal wake potential, the fundamental mode was filtered out, processing the wakefield data with MATLAB [46] and mathematically decoupling it from HOMs terms. As a result, the contribution of HOMs to the longitudinal wake potential is shown in Figure 3.8.

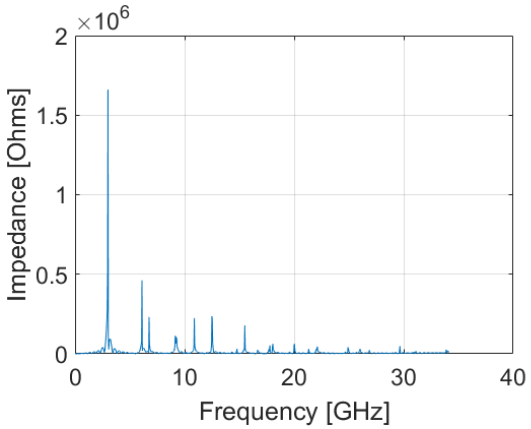

FIGURE 3.7: Longitudinal wakefield impedance.

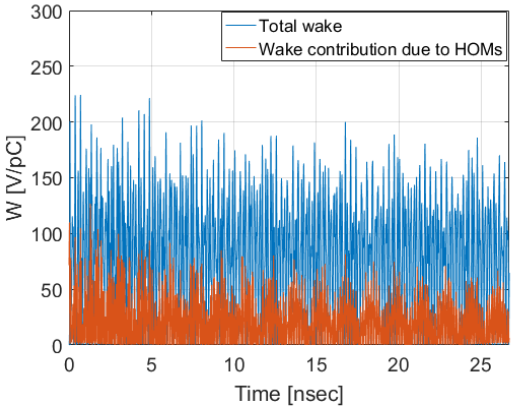

FIGURE 3.8: Contribution of HOMs to the longitudinal wake potential.

3.2.3 Analytical expression of wake functions

Two different techniques were investigated to determine the expression of the wake functions from the the wake potentials calculated with ABCI and CST [47]. First, the computation of the inverse Fourier transform of the wakefield impedance obtained from CST (see Equations 3.8 and 3.9) was attempted. Unfortunately, this approach suffers from a practical limit existing on the smallest usable rms bunch length, and it was not possible to extrapolate the data. As a second and successful approach, we relied on the observation that the wake functions have the same shape as the wake potentials, but with opposite sign [48], and that wake potentials associated to different bunch lengths tend to follow a common envelope after a certain distance from the bunch center. This envelope defines the wake function, which can therefore be evaluated from fitting, and in ranges of bunch length where the calculation of the wake potential in not computationally possible [49]. The wake potential was calculated for different rms bunch lengths in the range 0.4–5.0 mm.

Due to unrealizable mesh requirement by CST for the wake potential simulation in the whole 90 cells structure with short bunches, a comparison of ABCI and CST was done first for a single cell. Since an excellent agreement was found between the two codes for the single cell, as shown in Figures 3.9 and 3.10 for the longitudinal plane (the same applies to the transverse plane, not shown), ABCI only was then used for the whole structure.

The fitting of the longitudinal wake function to the envelope of wake potentials calculated for the whole structure is shown in Figure 3.11. The expression of the longitudinal

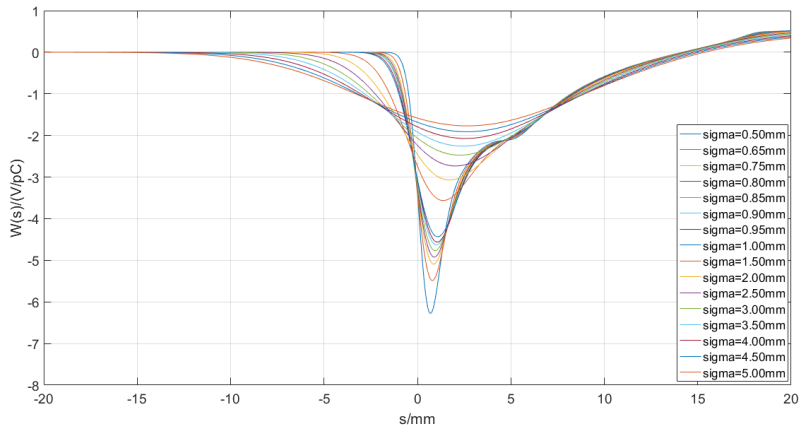

FIGURE 3.9: ABCI calculation of the longitudinal wake potential for different lengths of a Gaussian bunch, in a single cell.

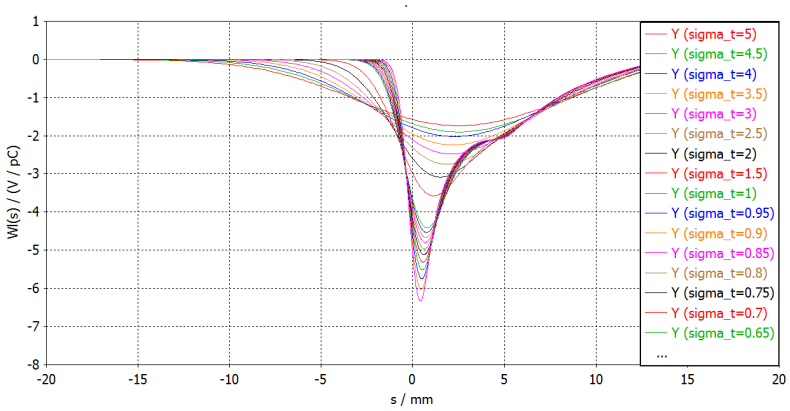

FIGURE 3.10: CST calculation of the longitudinal wake potential for different lengths of a Gaussian bunch, in a single cell. Compare with Figure 3.9.

wake function per unit length, in unit of $V/pC/m$ is:

$$G_{\parallel} = 260e^{-\sqrt{s/10^{-3}}} + 100e^{-\sqrt{s/(1.85\cdot 10^{-3})}} \tag{3.10}$$

A comparison of the fitting expression with the analytical model depicted in [39] is also shown in Figure 3.11.

The same technique was applied to the transverse plane, and provided the wake potentials in Figure 3.12. The analytical expression of the transverse wake function per unit

length, in unit of $V/pC/m^2$, which fits the envelope of curves, was found to be:

$$G_\perp = 0.4944\left[1-\left(2.787-1.787e^{\left(0.227\sqrt{s/10^{-3}}\right)}\right)\right]\cdot\left(1+\sqrt{\frac{s}{0.438\cdot 10^{-3}}}\right)e^{-\sqrt{s/(0.692\cdot 10^{-3})}} \tag{3.11}$$

A comparison of the fitting transverse wake function with the analytical model in [39] is also shown in Figure 3.12.

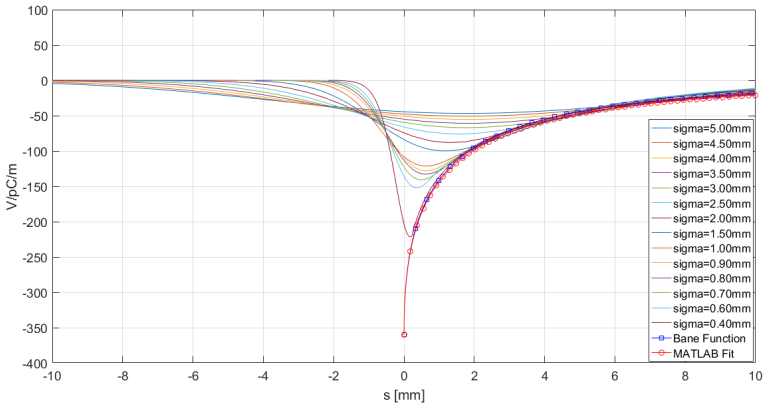

FIGURE 3.11: Longitudinal wake potential calculated for the whole structure with ABCI vs. rms length of a Gaussian bunch. The fitting wake function in Eq.3.10 and its analytical expression from Bane's model [39] are also shown for comparison.

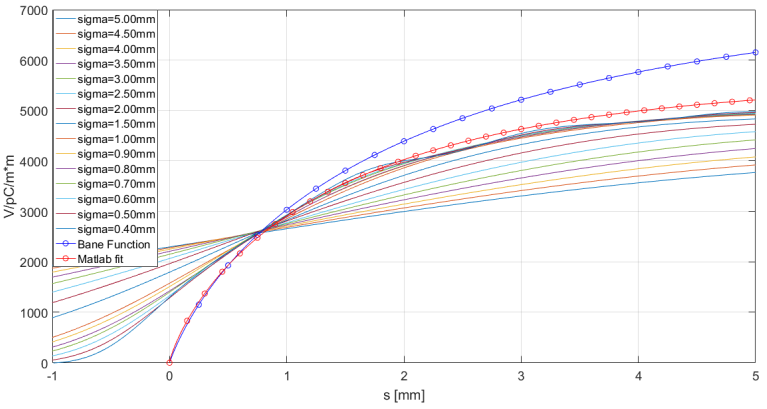

FIGURE 3.12: Transverse wake potential calculated for the whole structure with ABCI vs. rms length of a Gaussian bunch. The fitting wake function in Eq.3.11 and its analytical expression from Bane's model [39] are also shown for comparison.

3.3 Particle beam dynamics

3.3.1 Longitudinal phase space

If we consider a bunch of charged particles traveling down the accelerator along the axis of a vacuum chamber pipe, as we have seen before, the wakefield excited by the beam produces a longitudinal force on the particles of the beam itself. The main effect of this longitudinal force is a retarding voltage, causing energy changes of individual particles. However, not all the particles in the bunch lose the same amount of energy. The wakefield thus causes the beam to acquire an *energy spread* which is detrimental for the performances of the FEL.

The FERMI Linac provides nowadays an electron beam of 1.5 GeV mean energy, and a total relative energy spread $< 0.1\%$ (rms value). The energy of the particles is in correlation with their longitudinal position inside the bunch: the quantity that expresses this correlation is the linear energy chirp $h = \frac{dE}{E_0 dz}$, where E_0 is the beam mean energy, and its higher order components. The beam energy chirp in FERMI is strongly affected by the longitudinal wakefield excited in the BTW structures (the Linac sections L3 and L4 of Figure 3.13).

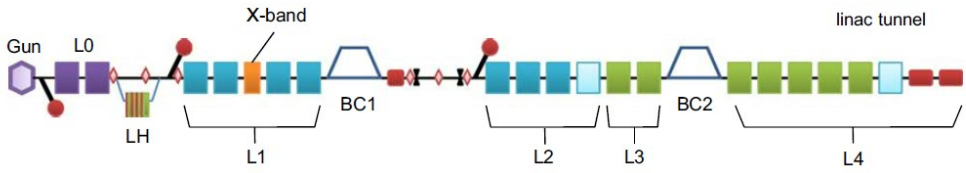

FIGURE 3.13: FERMI Linac layout.

One of the differences between the L0-L2 and the L3-L4 structures is the cell iris radius: the L0-L2 structures are built with iris radius of nearly ≈ 10 mm, while the BTW sections in L3-L4 have an iris radius of 5 mm. Due to such different geometry, the electron beam excites different transverse and longitudinal short-range wakefields at its passage through the cavities, which in turn affect the final beam transverse emittances and longitudinal phase space, respectively.

By renewing the L3-L4 accelerating structures, an energy up to 1.8 GeV is achievable [50, 33]. Lower wakefields are also expected by virtue of the inner geometry (i.e., larger iris radius) of the new RF structures. A comparison of the transverse and longitudinal wake functions in the present BTW structures and in the new ones is shown in Figure 3.14. The

wake amplitude of the new structures, evaluated at the center of the nominal bunch in FERMI, at a distance of approximately $s = 0.35mm$ from the bunch head, is smaller than in the present BTW by approximately a factor 3 for the longitudinal wake, and by a factor 10 for the transverse wake [47].

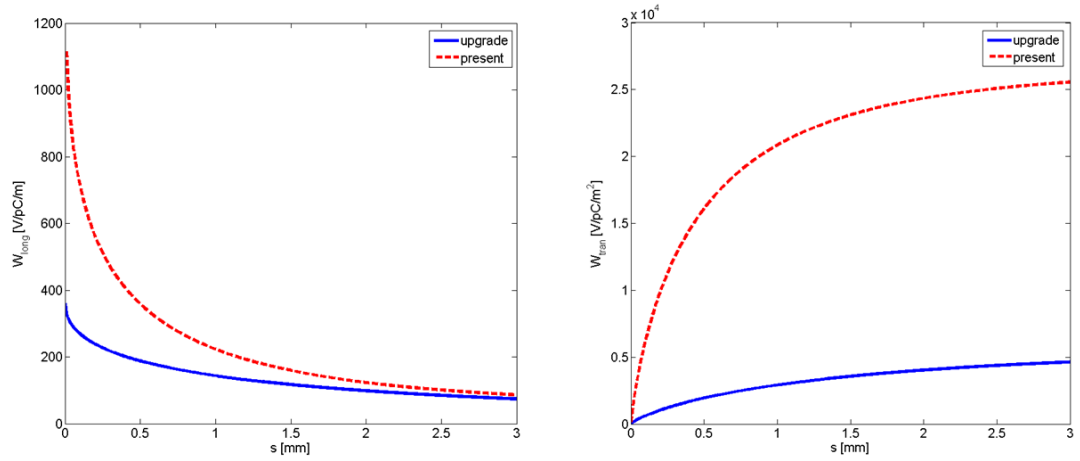

FIGURE 3.14: Longitudinal (left) and transverse wake function per unit length, evaluated over the whole structure, for the BTW ('present') [51], and for the new S-band structures ('upgrade').

While a weaker transverse wakefield is undoubtedly advantageous in order to get a smaller beam emittance, the impact of a weaker longitudinal wakefield on the beam dynamics is not obvious, and it needs evaluation of the final energy chirp content. Modeling of beam longitudinal dynamics with the $1D$ code LiTrack aimed at investigating the upgrade scenario while keeping the final energy spread $< 0.1\%$ and the energy chirp (up to the third order) lower than, or at most equal to, the present one.

The present layout (henceforth, Layout 1) was simulated first, aiming to reproduce the nominal longitudinal phase space at the Linac end. Then, modeling with LiTrack covered different upgrade scenarios, where the new S-band modules replace the seven BTW structures in L3-L4 [47]. At first, the new structures, characterized by the longitudinal wake function in Equation 3.10, were simulated considering the present accelerating gradient of 24 MV/m (Layout 2). Next, a higher gradient of 30 MV/m was considered (Layout 3). In all these configurations, all the cavities after BC1 (see Figure 3.13) are set at the RF phase of maximum acceleration ("on-crest"). Since this choice led to upgrade scenarios with a final relative energy spread $> 0.1\%$, variations of Layouts 2 and 3, respectively named Layout 2b and Layout 3b, were investigated, in which the new accelerating structures of L4 were run off-crest in order to fulfill the requirement of a total energy spread

$< 0.1\%$, while still maximizing the final beam energy.

Figure 3.15, obtained from a LiTrack run, shows the final bunch current profile for Layout 1. Since acceleration does not affect the electrons' longitudinal position inside the bunch, that current profile is common to all upgraded scenarios (no modification is foreseen for the compression stage). Figures 3.16 and 3.17 show the longitudinal phase space at the Linac end and its fit for, as an example, Layout 1 and 3b, respectively. A sixth-grade polynomial fit was then adopted for the present layout, a seventh-grade was chosen for all the upgraded ones.

Table 3.2 lists the final beam energy and energy spread, together with the structure's RF phase, and the energy chirp up to third order. In all upgrade scenarios, the energy chirp is equal to or lower than the one in Layout 1. We highlight how, owing to a minor contribution of longitudinal wakefields in the new structures, the linear energy chirp changes its sign in the upgrade. A mean energy reduction relative to the final beam energy of 1.6% (Layout 2b vs. 2) or 0.8% (Layout 3b vs. 3) is due to L4 cavities run off-crest with respect to the 'all on-crest' scenario.

Layout	$< E > [GeV]$	$\sigma_\delta[\%]$	$h_1\ [1/mm]$	$h_2\ [1/mm^2]$	$h_3\ [1/mm^3]$	$\Delta\phi_{L4}$
1	1.543	0.082	-1.395	1.08	35.2	0
2	1.551	0.174	1.232	1.00	-26.3	0
2b	1.526	0.098	0.485	1.00	-25.4	15
3	1.797	0.151	1.062	0.71	-20.8	0
3b	1.782	0.095	0.564	0.54	-30.3	10

TABLE 3.2: Longitudinal phase space features at the linac end (mean energy, rms relative energy spread, linear to cubic energy chirp) and L4 RF cavities phase shift from the point of maximum acceleration, for different linac settings (see context for details). Simulation results from LiTrack code.

3.3.2 Transverse emittance

In the previous section, the beam was considered to be centered in the vacuum chamber pipe, so there were no transverse wake forces. In case the beam is off axis, for example to its betatron oscillation (a stable oscillation about the equilibrium orbit in the horizontal and vertical planes), a dipole wakefield will be excited by the head of the bunch, which causes transverse deflection of its tail [52]. For high intensity beam, the betatron motion of the bunch tail can be seriously perturbed, leading to a transverse breakup of the beam.

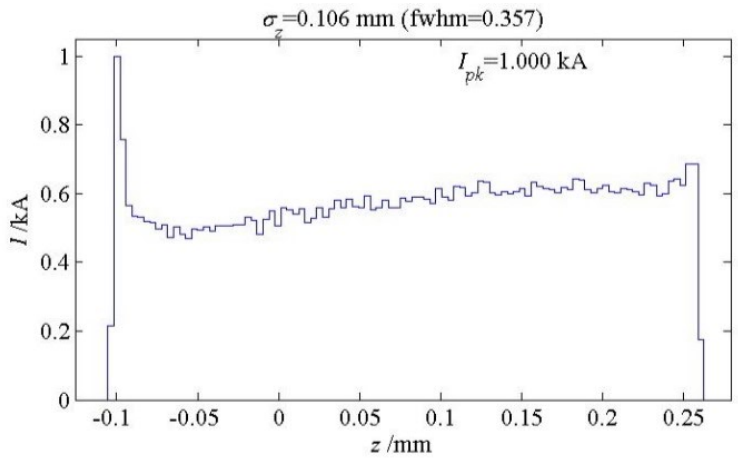

FIGURE 3.15: Beam current profile at the linac end in Layout 1, LiTrack simulation.

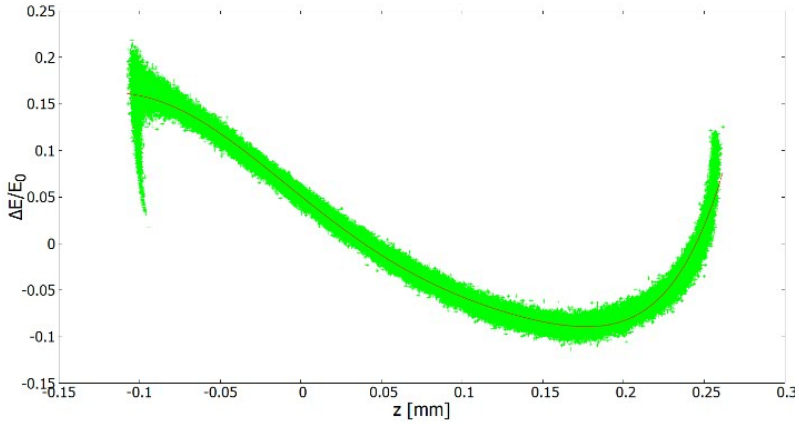

FIGURE 3.16: Longitudinal phase space at the linac end (LiTrack result) and its fit, Layout 1.

The emittance is a property of a charged particle beam in a particle accelerator and is a measure of the average spread of the particles in the *position-and-momentum* phase space. The emittance has the dimension of length (e.g., meters) or length times angle (meters times radians). A low-emittance particle beam is a beam where the particles are confined to a small distance and have nearly the same momentum and, for a FEL light source, this will result in higher brightness for the photon beam generated.

Since the wakefield kick is correlated along the bunch, the displaced bunch tail adds a contribution to the projection of the beam size on the transverse plane (same for the angular divergence), with the result that the projected emittance is increased. Opposite to longitudinal wake potential, the transverse one increases in strength with the bunch

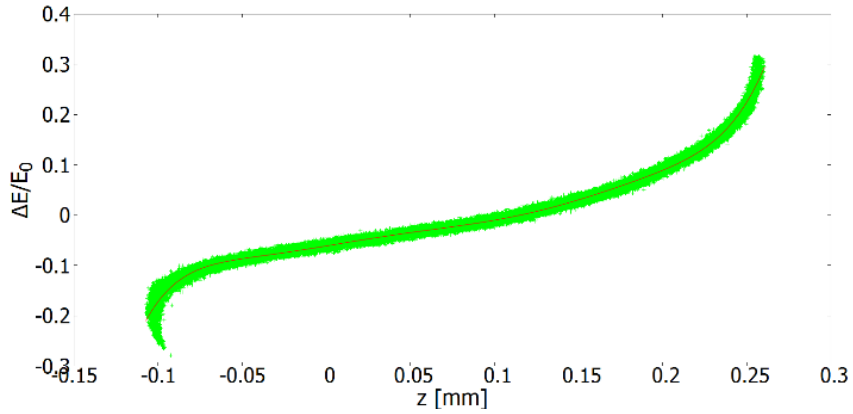

FIGURE 3.17: Longitudinal phase space at the linac end (LiTrack result) and its fit, Layout 3b.

length, driving particle oscillations with a force that, to first order in the particle coordinates, is linearly proportional to the relative distance of the leading particles from the electric axis of the accelerating structure (dipole mode approximation). This behavior leads to a positive feedback of the instability as trailing particles travelling off axis are pushed even farther from the Linac axis.

The mathematical description of single bunch beam break up is approached in the literature in at least two ways. One tries to analytically or numerically solve the single particle equation of motion in the presence of the wakefield driving term. A second method aims at estimating the final projected emittance growth in the assumption of full filamentation of the beam transverse phase space (emittance dilution). In the latter case, all details of the particles motion are lost, but rule-of-thumbs for the Linac misalignment budget can be attempted [53]. In the following, the second approach is adopted.

The particles betatron motion along the FERMI Linac, and in particular along the Linac sections L3 and L4, is periodic by design [54]. The lattice is made by one beam position monitor (BPM), corrector magnets and a quadrupole magnet in between consecutive accelerating structures.

Each lattice period is composed of a focusing (F) and a defocusing (D) quadrupole with a drift space (O) in between forming a FODO sequence. In the FERMI Linac, a FODO cell extends over two BTW structures, i.e., the cell length is approximately 13 m. While the beam mean energy increases linearly along the Linac, the average betatron function per cell is roughly proportional to the beam energy through a power coefficient $\alpha \approx 0.5$. The average betatron function along the whole L3 and L4 line is approximately 20 m. We assume that the optics configuration is not affected by the Linac upgrade.

With the FODO-cell lattice just introduced, the Linac-to-beam misalignment can be modeled by considering, for example, random misalignment of BPMs, random misalignment of individual structures, or random misalignment of paired structures. The latter case corresponds to random alignment errors of the structures about a smooth trajectory, but the error is systematic for two consecutive structures, as it may happen when consecutive quadrupoles are used for alignment reference. This kind of error can be shown to dominate over the two other scenarios for practical values of the misalignment [55], and the normalized emittance growth can be estimated as follows [53]:

$$\Delta(\gamma\epsilon) = \Delta_{str}^2[\pi\epsilon_0 r_e N_e G_\perp(2\sigma_z)]^2(\frac{L_{cell}\beta_{ave}}{4\alpha G_{acc}})[(\frac{\gamma_f}{\gamma_i})^{2\alpha} - 1] \tag{3.12}$$

The meaning of the symbols and their values for the L3 and L4 sections are depicted in Table 3.3. Figure 3.18 compares the final projected emittance growth induced by the transverse wakefield instability along L3 and L4 according to equation 3.12, for the present FERMI Linac and after replacement of the BTW structures. A final beam energy of 1.5 GeV is considered. An even smaller emittance growth is expected at the final energy of 1.8 GeV because of the higher beam rigidity. The contour plots show the wake-induced normalized emittance growth as a function of the beam-to-Linac misalignment (rms value of the structures' pairs) and of the bunch length. Different bunch lengths physically correspond to different compression factors at BC1, and thereby to a peak current in the range 0.2–1.2 kA. The nominal FERMI working point is for a bunch duration of 0.7 ps full width at half maximum (FWHM) and peak current of 0.6 kA, as indicated by the marker in both plots of Figure 3.18. By virtue of the scaling of the emittance growth with the square of the transverse wake function (see equation 3.12), and owing to the fact that the wake function of the new structures is approximately one order of magnitude smaller than that one of the BTW [51] for bunch lengths shorter than 1 mm (see Figure 3.14), the effect of the transverse wakefield instability on emittance is lowered by approximately two orders of magnitude.

Parameter	Symbol	Value	Units
Initial Mean Energy	$\gamma_i m_e c^2$	0.5	GeV
Final Mean Energy	$\gamma_f m_e c^2$	1.5	GeV
Bunch Charge	$N_e e$	0.7	nC
FODO Cell Length	L_{cell}	13	m
Accelerating Gradient	G_{acc}	24	MV/m
Average Betatron Function	β_{ave}	20	m
Optics Scaling Factor with Energy	α	0.5	

TABLE 3.3: Parameters of the electron beam and of the Linac sections L3 and L4, used for the estimation of the emittance growth induced by transverse wakefield instability, see Equation 3.12.

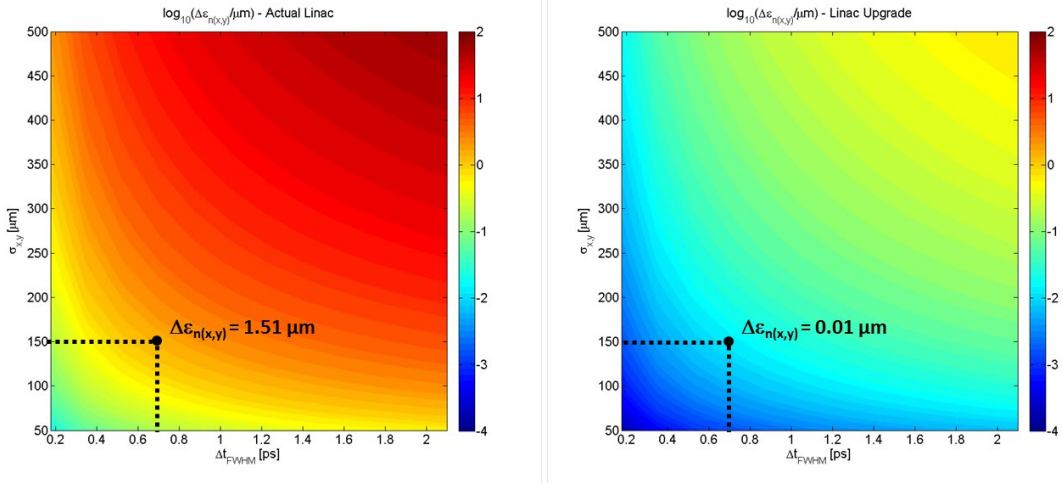

FIGURE 3.18: Transverse normalized emittance growth (either horizontal or vertical) through L3 and L4 as a function of the bunch duration (FWHM) and of the Linac-to-beam relative misalignment (rms), for the present FERMI Linac (left) and for the Linac upgrade. The markers identify the actual FERMI working point. Note the emittance is in the same log scale in the two plots. Beam and Linac parameters used for this analytical calculation are listed in Table 3.3

4 The RF Pulse Compressor

4.1 Introduction

The high energy part of the FERMI Linac is composed of seven accelerating structures, each one 6 meters long, that could theoretically achieve an accelerating gradient of $30MV/m$. Each structure is powered by an RF source (klystron) rated for $45MW$ peak power, and $4.5\mu s$ pulse width.

Since the peak power available from the klystron itself would not be sufficient to achieve the maximum gradient, each power plant is equipped with a pulse-compression system which allows, as it will be shown later on, to increase the peak power delivered to the accelerating structure at the expense of the pulse duration.

The current FERMI pulse-compression systems, named SLED (SLAC Energy Doubler), were installed in the injector of the Elettra synchrotron in 1990. After the decommissioning of the Elettra injector, in 2008 the SLED systems were moved from Elettra to the FERMI tunnel and installed in the high energy part of the linear accelerator.

Figure 4.1 shows the SLED system, made up of two cylindrical resonant cavities, just at the input of a BTW accelerating structure. Nowadays the SLED systems need a continuous maintenance. However, because of the weight and the position in the Linac tunnel, the resonant cavities are really difficult to maintain.

In the frame of the Linac upgrade program, it was decided to design a new, compact, RF pulse compressor. This pulse compression system is based on a single, spherical, resonant cavity in which two different modes, orthogonal each other are excited. Despite of its compactness, the new pulse compressor shows a compression efficiency similar to the present system.

FIGURE 4.1: A Backward Travelling Wave accelerating structure equipped with a SLED type rf pulse compressor

4.2 SLED

The SLED was invented in 1973 at the Stanford Linear Accelerator Center (SLAC) [56]. Since the accelerator energy is determined by the peak RF input power, it was felt that some method for enhancing the peak power at the expense of the RF pulse width might be the answer for increasing the SLAC energy, without increasing the average power consumption. An approach that seemed to hold this promise, came as the result of the experience with superconducting cavities, performed at SLAC. During the measurements on superconducting cavities, it was observed that the power radiated from a cavity that was heavily overcoupled approached four times the incident generator power, immediately after the generator was switched off [56]. However, normally the radiated power travels as a reverse wave back toward the generator: this problem was solved by using of a microwave network which could direct this radiated power into an external load. The RF network was made up of two identical cavities attached to a 3dB hybrid, as shown in Figure 4.2.

Using overcoupled cavities, it was obtained a power multiplication factor which enhanced the peak power by a factor of four. This was accomplished, of course, at the

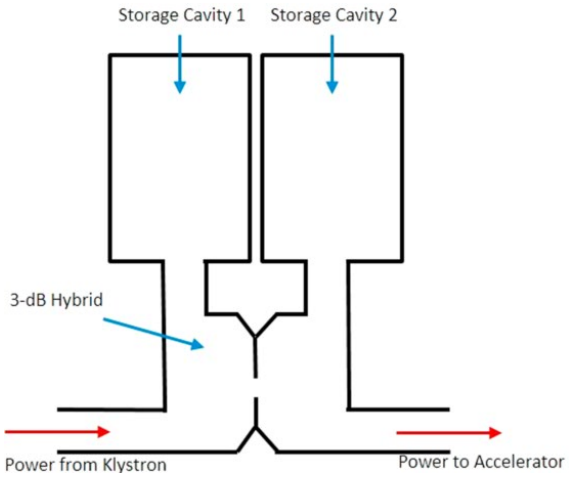

FIGURE 4.2: Schematic drawing of the SLED microwave network

expense of the pulse width, since the radiated power decays away in a time constant given by the cavity filling time. Furthermore, it was observed that if the RF source is reversed in phase rather than simply being switched off, the peak power can be increased by up to a factor of nine.

4.2.1 Qualitative description

Usually, the RF power generated by a klystron travels through a waveguide directly into the accelerating section as indicated schematically in Figure 4.3.

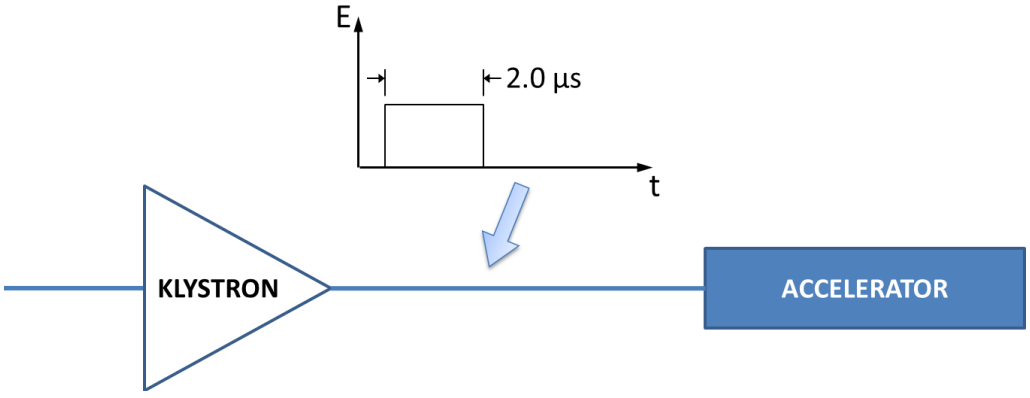

FIGURE 4.3: Schematic representation of a simple waveguide distribution system

In the case of a pulse compression scheme, the SLED microwave network, consisting of one 3dB hybrid and two cavities, is inserted between the klystron and the accelerating structure, as shown in Figure 4.4.

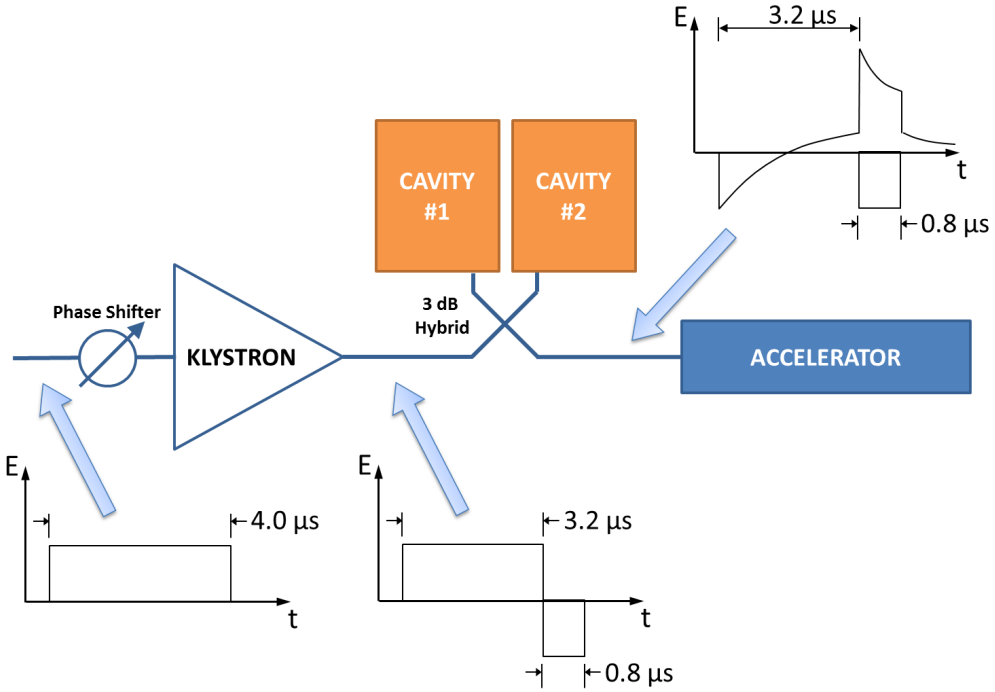

FIGURE 4.4: Schematic representation of a SLED RF system

The cavities are assumed to be identical and tuned to resonance. After the RF pulse is turned on, the fields in the cavities build up and a wave of increasing amplitude is radiated from the coupling apertures of each cavity [56]. The two emitted waves combine so as to add at the accelerator port of the 3dB hybrid, while they cancel each other at the klystron port. In addition to the wave emitted from the cavities, a wave travels directly from the klystron to the accelerator. This direct wave, which is just the wave that would appear at the accelerator if both the cavities were detuned, is opposite in phase to the combined emitted waves. If the cavities are overcoupled, the emitted wave grows in time to an amplitude which is larger than the direct wave.

The net field at the input of the accelerator is the sum of the direct and emitted waves. One accelerator filling time ($0.8\mu s$ in Figure 4.4) before the end of the RF pulse, the phase shifter at the input of the klystron reverses the phase of the output wave from the klystron as shown by the waveform at the bottom of Figure 4.4.

Immediately after this phase reversal, the emitted and direct waves add in phase at the

accelerator, since the emitted wave (which is proportional to the stored fields in the cavities) cannot change instantaneously. Therefore, when the klystron phase is reversed, the field at the input to the accelerator increases by $2E_{in}$, where E_{in} is the amplitude of the wave emitted by the klystron.

Following the phase reversal, the field in the cavities (and hence the emitted wave also) decrease rapidly as the cavities try to charge up to a new field level of opposite phase. The resultant wave at the accelerator decreases also, as it is shown qualitatively in Figure 4.4. At the end of the RF pulse, the direct wave goes to zero and the emitted wave only is present at the accelerator. It then decays to zero with a time constant given by the resonant cavity filling time.

4.2.2 SLED theory

An analytic description of the SLED mechanism [11] is obtained by appealing to the conservation of the power. Precisely, we can write:

$$P_{in} = P_{out} + P_c + \frac{dU_c}{dt} \tag{4.1}$$

where P_{in} is the power from the klystron, P_{out} is the power to the accelerator (see Figure 4.4), P_c is the power dissipated in the resonant cavity walls, and U_c is the electromagnetic energy stored in the cavity. Let k be the proportionality constant relating the square of the field amplitude to the power flow in the waveguide, that is:

$$P_{in} = kE_{in}^2 \tag{4.2}$$

Also, as seen before, the output wave is the superposition of the emitted wave E_e from the SLED cavity and the incident wave from the klystron E_{in}, opposite in phase to the field emitted from the cavity. So, P_{out} can be expressed as:

$$P_{out} = kE_{out}^2 = k\left(E_e + \Gamma E_{in}\right)^2 \tag{4.3}$$

where Γ is the reflection coefficient of the waveguide-cavity interface. From the definition of the cavity coupling coefficient, β, as the ratio of emitted to dissipated power (in absence of the incident wave), we can write:

$$P_c = \frac{kE_e^2}{\beta} \tag{4.4}$$

Finally, from the definition of the unloaded quality factor Q_0, we have:

$$U_c = \frac{Q_0}{\omega} P_c = \frac{Q_0}{\omega} \frac{kE_e^2}{\beta} \tag{4.5}$$

with ω the resonant frequency, assumed equal to the drive frequency, so that:

$$\frac{dU_c}{dt} = \frac{2kQ_0}{\omega\beta} E_e \frac{dE_e}{dt} \tag{4.6}$$

We define $t = 0$ as the instant when the input pulse reaches the cavity. At this time U_c is zero, as the cavity cannot fill instantaneously and, therefore, E_e is zero. Substituting the equations 4.2, 4.3, 4.4 and 4.6 into the equation 4.1, we have:

$$kE_{in}^2 = k\left(E_e + \Gamma E_{in}\right)^2 + \frac{kE_e^2}{\beta} + \frac{2kQ_0}{\omega\beta} E_e \frac{dE_e}{dt} \tag{4.7}$$

Considering that $E_e = 0$ at $t = 0$, E_e, we then have $|\Gamma| = 1$. To account for the π phase shift associated with the reflection from the waveguide-cavity interface, we set $\Gamma = -1$. We can then use the equation 4.1 to obtain:

$$E_{in}^2 = \left(E_e - E_{in}\right)^2 + \frac{1}{\beta} E_e^2 + \frac{2Q_0}{\omega\beta} E_e \frac{dE_e}{dt} \tag{4.8}$$

From equation 4.8 we have the following first order, non-homogeneous differential equation for the emitted wave:

$$\frac{dE_e}{dt} + \frac{\omega}{2Q_L} E_e = \frac{\omega\beta}{Q_0} E_{in} \tag{4.9}$$

where Q_L is the loaded Q, given by $Q_L = Q_0/(1+\beta)$. Defining $T_c = 2Q_L/\omega$ and $\alpha = 2\beta/(1+\beta)$, it is useful to rewrite equation 4.9 as:

$$T_c \frac{dE_e}{dt} + E_e = \alpha E_{in} \tag{4.10}$$

It is seen that T_c is the loaded cavity time constant and that α gives the steady-state emitted field.

As indicated before, the input to SLED is a constant amplitude pulse with the phase reversed towards the end. For simplicity let's use the unit field and redefine E_{in} as follows:

$$E_{in} = \begin{cases} 1 & 0 \le t < t_1 \\ -1 & t_1 \le t < t_2 \\ 0 & t_2 < t \end{cases} \tag{4.11}$$

With this piecewise-constant driving term and the condition $E_e = 0$ at $t = 0$, the solution to equation 4.10 is given by:

$$E_e\left(0 \le t < t_1\right) = \alpha\left(1 - e^{-t/T_c}\right) \tag{4.12a}$$

$$E_e\left(t_1 \le t < t_2\right) = \alpha\left[\left(2 - e^{-t_1/T_c}\right)e^{-(t-t_1)/T_c} - 1\right] \tag{4.12b}$$

$$E_e\left(t > t_2\right) = \alpha\left[\left(2 - e^{-t_1/T_c}\right)e^{-(t_2-t_1)/T_c} - 1\right]e^{-(t-t_2)/T_c} \tag{4.12c}$$

We can now express the normalized output, $E_{out} = E_e - E_{in}$, as

$$E_{out}\left(0 \le t < t_1\right) = \alpha\left(1 - e^{-t/T_c}\right) - 1 \tag{4.13a}$$

$$E_{out}\left(t_1 \le t < t_2\right) = \alpha\left[\left(2 - e^{-t_1/T_c}\right)e^{-(t-t_1)/T_c} - 1\right] + 1 \tag{4.13b}$$

$$E_{out}\left(t > t_2\right) = \alpha\left[\left(2 - e^{-t_1/T_c}\right)e^{-(t_2-t_1)/T_c} - 1\right]e^{-(t-t_2)/T_c} \tag{4.13c}$$

As it can be seen from equations 4.13, the output field initially builds up toward $\alpha - 1$. After the phase reversal and the accompanying amplitude jump, it begins falling exponentially toward $-(\alpha - 1)$ with a time constant T_c. The input and output waveforms are illustrated in Figure 4.5

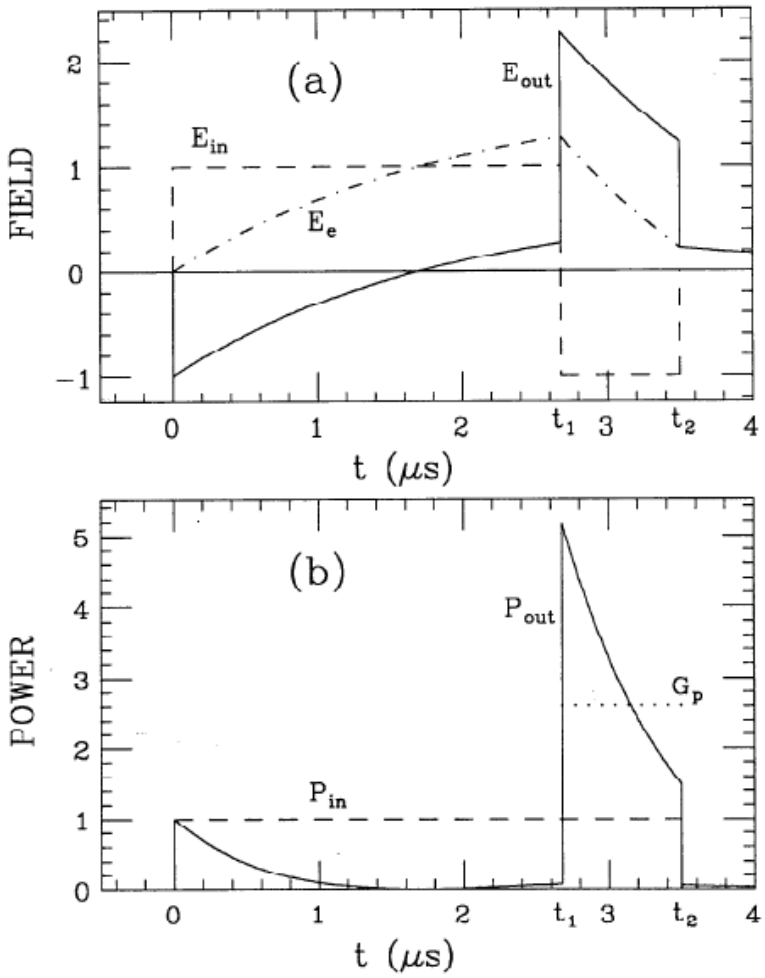

FIGURE 4.5: SLED field and power waveforms

From equations 4.13, we also see that the maximum field intensity with a SLED system is magnified by a factor given by:

$$E_{max} = E_{out}(t_1) = \alpha\left(1 - e^{-t_1/T_c}\right) + 1 \tag{4.14}$$

4.2.3 SLED in use

The energy gain of a particle beam which traverses an accelerating structure powered with a SLED is not as much as the one that would be given by the peak field seen by the structure. This is due to the exponential decay of the pulse's amplitude and the finite filling time of the structure, so we must take this into account in evaluating the benefit of a SLED system [11].

For a constant-impedance accelerating structure, the energy gain of a charged particle beam can be measured by the average across the compressed pulse of the field magnification weighted by the attenuation of the structure. So, the voltage across the structure filled with the compressed pulse is:

$$V_{ci} = \int_0^L E\left(z,t\right) dz = v_g e^{-\alpha v_g t_2} \int_{t_1}^{t_2} E_{out}\left(t\right) e^{\alpha v_g t} dt \tag{4.15}$$

where v_g is the group velocity and α the attenuation per unit length in the structure.

In a constant-gradient structure, the group velocity is linearly increasing from the input end to the output end, in order to maintain the field strength (for a flat input pulse) as the power is dissipated in the walls. Let us define g such that

$$v_g\left(z\right) = v_{g0}\left(1 - \frac{g}{L}z\right) \tag{4.16}$$

where L is the length of the accelerating section. If we consider a particle which enters the structure at a time $t = 0$, the accelerating voltage at a time t_i is given by:

$$V_{cg} = \int_0^L E\left(z,t_i\right) dz = \int_0^L E\left(t_i - \Delta t\left(z\right)\right) dz \tag{4.17}$$

where

$$\Delta t\left(z\right) = \int_0^z \frac{dz'}{v_g\left(z'\right)} = -\frac{L}{g v_{g0}} ln\left(1 - \frac{g}{L}z\right) \tag{4.18}$$

For a particle entering between t_1 and t_2, the accelerating voltage is given by [11, 56]:

$$V_{cg}\left(t_1 < t_i < t_2\right) = \frac{L}{g}\Bigg\{(\alpha-1)\left[g-2+2\left(1-g\right)^{(t_i-t_1)/T_f}\right] - \frac{\alpha e^{-t_i/T_c}}{C}\left[1-\left(1-g\right)^{C}\right] + \frac{2\alpha e^{-\left(-(t_i-t_1)/T_c\right)}}{C}\left[1-\left(1-g\right)^{C(t_i-t_1)/T_f}\right]\Bigg\} \tag{4.19}$$

Here T_f is the structure filling time, assumed equal to $t_2 - t_1$, and

$$C = 1 - \frac{L}{g v_{g0} T_c} = 1 + \frac{T_f}{T_c ln\left(1-g\right)} \tag{4.20}$$

Setting $L = 1$ normalizes the voltage to that of a structure filled with a unit-amplitude pulse, without any pulse compression. The accelerating voltage as a function of the injection time (the instant of beam injection into the structure) is shown in Figure 4.6, and its maximum, at $t_i = t_2$, when the compressed pulse fills the structure, is then

$$V_{cg\,max} = \frac{\alpha}{gC} e^{-T_f/T_c}\left(2 - e^{-t_1/T_c}\right)\left[1-\left(1-g\right)^{C}\right] - \alpha + 1 \tag{4.21}$$

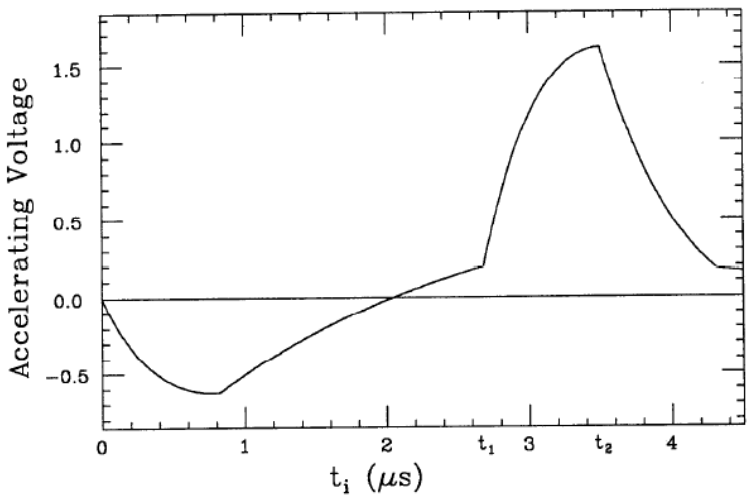

FIGURE 4.6: Acceleration versus injection time, normalized to the acceleration obtained without SLED

The theoretical limit of $V_{cg\,max}$ is seen to be three. However, in reality this limit cannot be approached with finite-Q SLED cavities because of the competing requirements of large β and large T_c.

4.3 The spherical Pulse Compressor

The SLED-type pulse compressor is based on two cylindrical cavities working on the TE_{015} mode and with an unloaded Q-factor of nearly 180000. This type of pulse compressor is easy to design and machine. However, due to its two big resonant cavities, its scale is quite large. In addition, the frequency difference of the two cavities must be less than $10kHz$ to generate a stable output RF power, which requires temperature fluctuation lower than $0.1°$. Since the two cavities are independent, this requires a dedicated and complicated cooling system.

The proposed pulse compressor [57] is instead based on only one spherical cavity, excited with two polarized TE_{113} modes, and a dual-mode coupler. Based on this design, the resonant frequencies of the two polarized modes can be easily tuned to the same frequency and, even more important, the frequency shift of the two modes is the same for any fluctuation of the temperature during operation. This pulse compressor is then very compact and requires a much simpler cooling system.

4.3.1 Spherical cavity theory

In a spherical cavity resonator, the solutions of the Maxwell's equations, in spherical coordinates and with axial symmetry ($\partial/\partial\phi = 0$), separate into electromagnetic fields with components E_r, E_θ, H_ϕ and electromagnetic fields with components H_r, H_θ, E_ϕ [58]. These are called *TM* and *TE* types, respectively, the spherical surface with constant *r* serving here as the transverse surface.

Let us consider a *TE* spherical mode with axial symmetry, by setting $\partial/\partial\phi = 0$ in Maxwell's equations in spherical coordinates. The three curl equations containing H_r, H_θ, E_ϕ are:

$$\frac{\partial}{\partial r}\left(rH_\theta\right) - \frac{\partial H_r}{\partial \theta} = j\omega\epsilon\left(rE_\phi\right) \tag{4.22}$$

$$\frac{1}{r\sin\theta}\frac{\partial}{\partial\theta}\left(E_\phi \sin\theta\right) = j\omega\mu E_r \tag{4.23}$$

$$\frac{\partial}{\partial r}\left(rE_\phi\right) = j\omega\mu\left(rH_\theta\right) \tag{4.24}$$

Equations 4.23 and 4.24 may be differentiated and substituted in 4.22, leading to the following equation in E_ϕ:

$$\frac{\partial^2}{\partial r^2}\left(rE_\phi\right) + \frac{1}{r^2}\frac{\partial}{\partial\theta}\left[\frac{1}{\sin\theta}\frac{\partial}{\partial\theta}\left(rE_\phi\sin\theta\right)\right] + k^2\left(rE_\phi\right) \tag{4.25}$$

To solve this partial differential equation, the product solution technique can be used [58]:

$$\left(rE_\phi\right) = R\Theta \tag{4.26}$$

where R is a function of r alone, and Θ is a function of θ alone. If this is substituted in 4.25, the function of r can be separated from the function of θ, and these must be separately equal to a constant. If we label this constant as $n\left(n+1\right)$, we get:

$$\frac{r^2}{R}\frac{d^2R}{dr^2} + k^2r^2 = -\frac{1}{\Theta}\frac{d}{d\theta}\left[\frac{1}{\sin\theta}\frac{d}{d\theta}\left(\Theta\sin\theta\right)\right] = n\left(n+1\right) \tag{4.27}$$

Thus we have two ordinary differential equations, one in r the other in θ.

Let us consider that in θ first. Making the substitutions:

$$u = \cos\theta, \qquad \sqrt{1-u^2} = \sin\theta, \qquad \frac{d}{d\theta} = -\sin\theta\frac{d}{du} \tag{4.28}$$

The differential equation can be written in the form:

$$\left(1-u^2\right)\frac{d^2\Theta}{du^2} - 2u\frac{d\Theta}{du} + \left[n\left(n+1\right) - \frac{1}{1-u^2}\right]\Theta = 0 \tag{4.29}$$

The differential equation 4.29 is reminiscent of Legendre's equation and is in fact a standard form. This form is:

$$\left(1-x^2\right)\frac{d^2y}{dx^2} - 2x\frac{dy}{dx} + \left[n\left(n+1\right) - \frac{m^2}{1-x^2}\right]y = 0 \tag{4.30}$$

One of the solutions is:

$$y = P_n^m(x) \tag{4.31}$$

and the function defined by this solution is called an associated Legendre function of the first kind, order n, degree m.

Let's now consider the r differential equation obtainable from 4.27. Making the substitution $R_1 = R/\sqrt{r}$, we get:

$$\frac{d^2R_1}{dr^2} - \frac{1}{r}\frac{dR_1}{dr} + \left[k^2 - \frac{\left(n+\frac{1}{2}\right)^2}{r^2}\right] R_1 = 0 \tag{4.32}$$

It is seen that this is a Bessel's differential equation of order $\left(n+\frac{1}{2}\right)$.

From the equations 4.30 and 4.32 the analytical expressions of the fields or, alternatively, the wave potentials can be derived (for more details, see [58]). For more convenience, in the following we report the analytical expression of the wave potentials for a TE_{mnp} mode:

$$(F_r)_{mnp} = \hat{J}_n\left(u_{np}\frac{r}{a}\right) P_n^m(\cos\theta) \begin{pmatrix}\cos m\varphi \\ \sin m\varphi\end{pmatrix} \qquad m \leq n \tag{4.33}$$

where $\hat{J}_n$ is the spherical Bessel function of order n, and u_{np} represents the zeros of the spherical Bessel function $\hat{J}_n$.

4.3.2 Spherical cavity for pulse compressor

The wave potential for the mode TE_{m1p} of a spherical cavity has the following expression:

$$(F_r)_{m1p} = \hat{J}_1\left(u_{1p}\frac{r}{a}\right) P_1^m(\cos\theta) \begin{pmatrix}\cos m\varphi \\ \sin m\varphi\end{pmatrix} \qquad m = 0, 1 \tag{4.34}$$

where

$$P_1^0(\cos\theta) = \cos\theta \tag{4.35a}$$
$$P_1^1(\cos\theta) = -\sin\theta \tag{4.35b}$$

Substituting equations 4.35 in equation 4.34, we have:

$$(F_r)_{01p} = \hat{J}_1\left(u_{1p}\frac{r}{a}\right)\cos\theta \tag{4.36a}$$
$$(F_r)_{11p} = -\hat{J}_1\left(u_{1p}\frac{r}{a}\right)\sin\theta\sin\varphi \tag{4.36b}$$
$$(F_r)_{11p} = -\hat{J}_1\left(u_{1p}\frac{r}{a}\right)\sin\theta\cos\varphi \tag{4.36c}$$

For TE modes, the boundary conditions impose that $E_\varphi = H_\theta = 0$ at the surface $r = a$, which means $\hat{J}_1(u_{1p}) = 0$. Therefore, given the resonant frequency f_0, the sphere radius a can be calculated as follows:

$$a = \frac{u_{1p}}{2\pi f_0\sqrt{\epsilon_0\mu_0}} \tag{4.37}$$

where u_{1p} represents the zeros of the spherical Bessel function $\hat{J}_1$.

As explained before, the SLED pulse compression principle is based on the use of a 3dB hybrid that split the incoming power in two, 90 degrees *out-of-phase* waves. These waves feed two identical, high-Q resonant cavities. The fields emitted by the cavities combine then *in-phase*, and the resulting wave is directed to the accelerating structure.

Looking at equation 4.36, it is clear that for a TE_{m1p} configuration, there are 3 modes with the same pattern, but rotated 90 degrees from each other, as it can be seen in Figure 4.7.

In a perfect sphere, these three modes have the same resonant frequency, but in reality they can be distinguished in frequencies due to the perturbation from the coupler port. As it will be shown later on, using a dual-mode coupler, named *E-rotator* in the following, we will be able to excite only the two TE_{11p} modes, while the TE_{01p} mode will be higher in frequency and very weakly coupled due to the field orientation.

Having two modes resonating at the same frequency and orthogonal to each other, the spherical resonator is suitable to be used for a pulse compression scheme, replacing the two cylindrical SLED cavities.

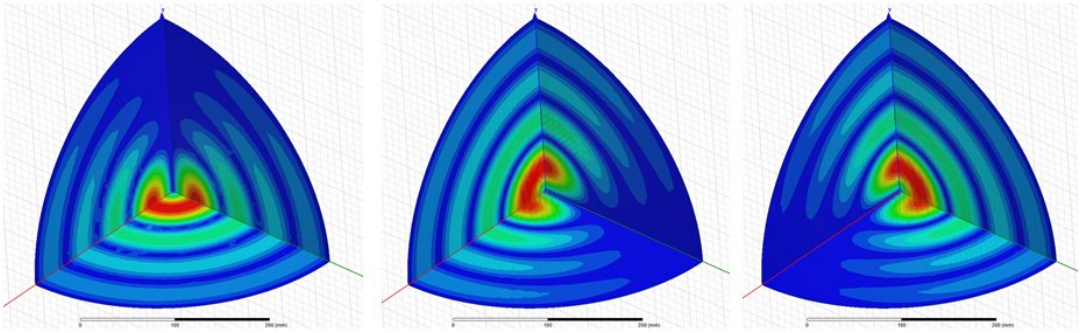

FIGURE 4.7: Three TE_{m1p} modes, with the same field pattern but rotated $90°$ in space from each other. In the figure the field pattern for $n = 4$ is showed

4.3.3 Choice of the RF parameters

For a spherical resonant cavity that works on the TE_{11p} mode, the unloaded quality factor Q_0 is given by:

$$Q_0 = \frac{a}{\delta} \tag{4.38}$$

where a is the radius of the sphere and $\delta = 1/\sqrt{\pi f \mu \sigma}$ is the skin depth. The previous equation indicates that the unloaded quality factor is solely defined by the radius of the spherical resonant cavity, and that a larger cavity produces a higher Q_0.

As seen in the previous paragraph, using a pulse compression scheme the maximum voltage multiplication factor is given by:

$$V_{cg\,max} = \frac{\alpha}{gC} e^{-T_f/T_c} \left(2 - e^{-t_1/T_c}\right) \left[1 - (1-g)^C\right] - \alpha + 1 \tag{4.39}$$

where $T_c = 2Q_L/\omega$, $Q_L = Q_0/(1+\beta)$, and $\alpha = 2\beta/(1+\beta)$.

Once the klystron pulse width and the filling time of the structure are fixed, from equation 4.39 it is evident that $V_{cg\,max}$ is a function of the unloaded quality factor Q_0 and of the coupling coefficient β of the resonant spherical cavity.

Table 4.1 shows the sphere radii, calculated according to equation 4.37, and the corresponding values of Q_0, given by 4.38, for different TE_{11p} modes. Using equation 4.39, for each value of Q_0 the corresponding optimal value of the coupling factor β can be obtained.

TABLE 4.1: Sphere radius a and Q_0 for different TE_{11p} mode

	a $[mm]$	Q_0
TE_{112}	123	102000
TE_{113}	174	144000
TE_{114}	224	185000
TE_{115}	274	227000

Figure 4.8 shows the maximum voltage multiplication factor as a function of the coupling factor for different values of Q_0

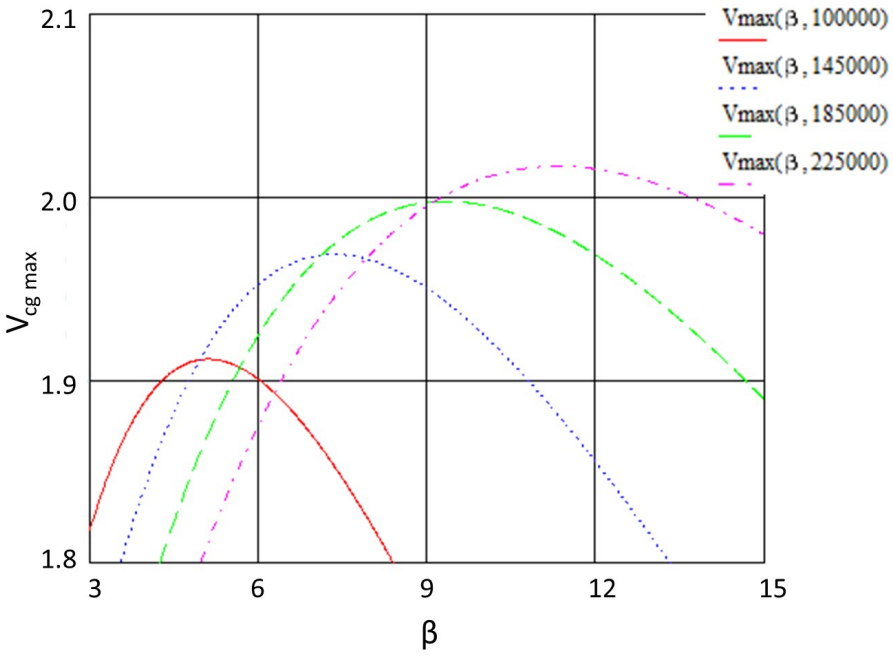

FIGURE 4.8: $V_{cg\,max}$ as a function of the coupling factor β for different values of Q_0

As it can be seen from Table 4.2 and Figure 4.9, for very high values of Q_0 the increment in the voltage multiplication factor is limited. For this reason, rather then pushing for very high values of the Q-factor, it was decided to find a trade-off between the accelerating efficiency and the size of the pulse compressor. A more compact size, in fact, results in a much lower cost.

So, the TE_{113} was selected as the operating mode: in this case, the sphere is still compact and we get a Q_0 of 144000, quite high if compared with commercial solutions of similar

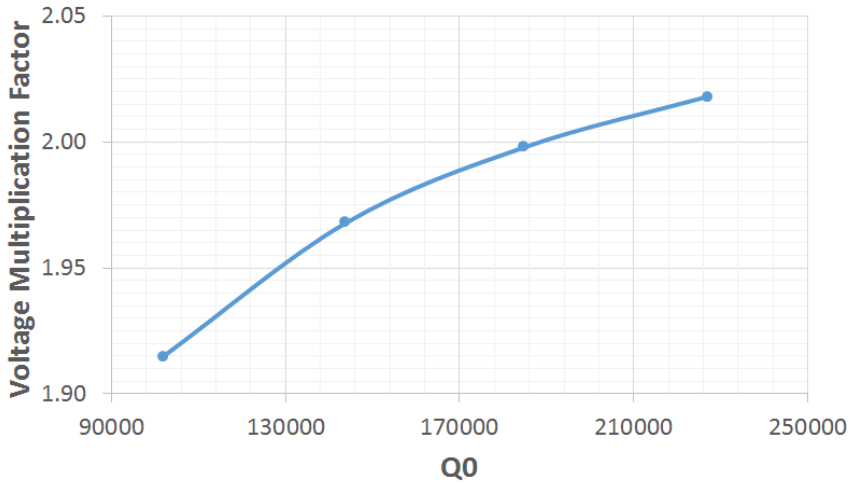

FIGURE 4.9: Maximum voltage multiplication factor as a function of Q_0

TABLE 4.2: Relevant RF parameters for the spherical pulse compressor

	a [mm]	Q_0	β	$V_{cg\,max}$
TE_{112}	123	102000	5.2	1.915
TE_{113}	174	144000	7.3	1.968
TE_{114}	224	185000	9.3	1.998
TE_{115}	274	227000	11.4	2.018

size, which usually have an unloaded Q-factor of nearly 90000.

Furthermore, if we compare the TE_{113} and TE_{114} modes, we see that in the first case the sphere is 10 cm smaller (in diameter) but the loss in accelerating voltage is just 1.5%.

4.3.4 Pulse compressor

4.3.4.1 Coupling to the sphere

Figure 5.3 shows the electric field magnitude for the two TE_{113} modes in the spherical resonator. As it is evident, the two modes have the same field pattern, but are rotated 90 degrees in space.

The vector representation of the electric field lines is reported in Figure 4.11: as it can be easily seen from the figure, in the highlighted position we have field lines for both the TE_{113} modes, so this one is the optimal position for the waveguide coupler. In order

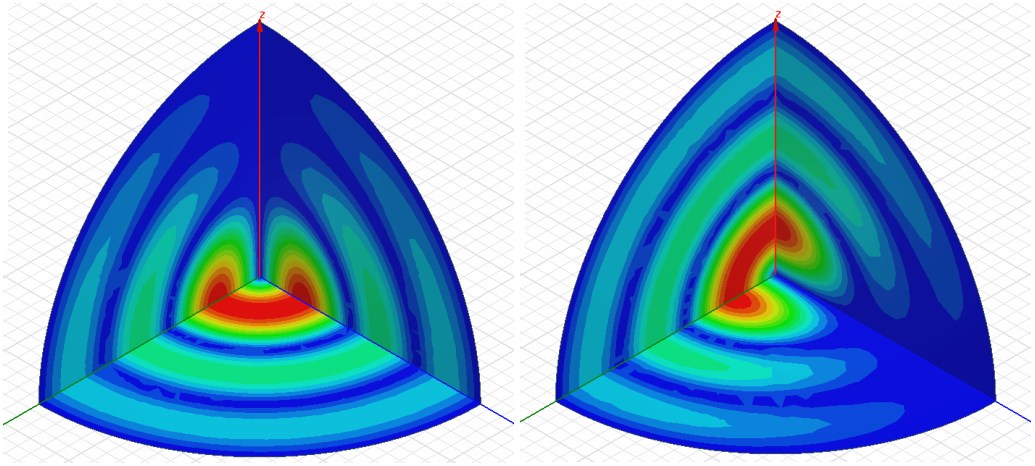

(a) (b)

FIGURE 4.10: Electric field magnitude for the two TE_{113} modes

to couple with the two fields, we will use a circular waveguide excited with two TE_{11} modes, orthogonal to each other and 90 degrees *out-of-phase*.

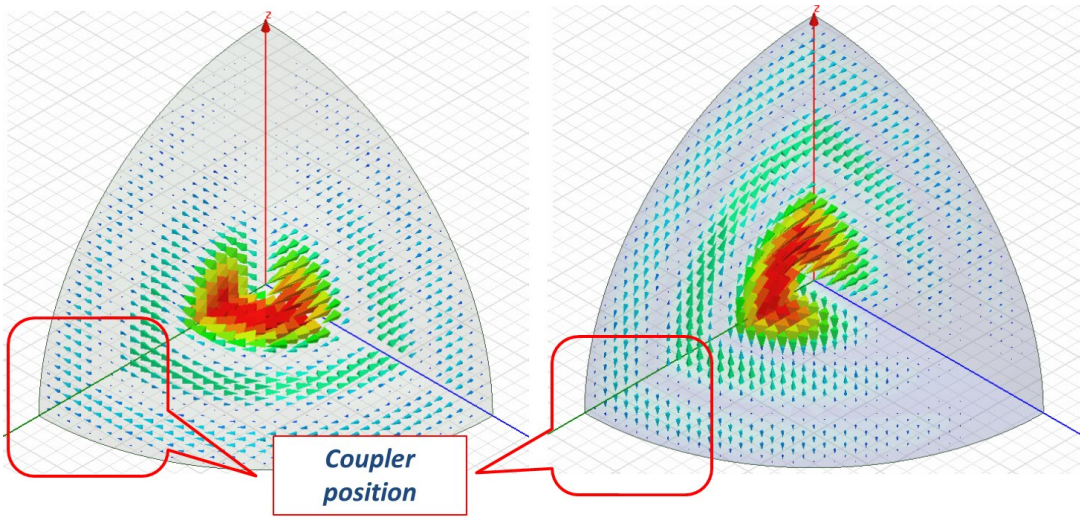

FIGURE 4.11: Electric field lines for the two TE_{113} modes. In the figure the optimal position for the coupler is also shown: in this region, the two resonant TE_{113} modes have electric field lines orthogonal to each other, with similar amplitude. Coupling a circular waveguide, carrying two orthogonal TE_{11} modes, to the sphere will excite the two resonant modes of interest

The sketch of the coupler is shown in Figure 4.12. The radius of the circular waveguide is assigned, and equal to 35.6 mm. This value assures that just the fundamental TE_{11} mode

propagates at the selected resonant frequency, while the first high order mode, the TM_{01}, is in cut-off.

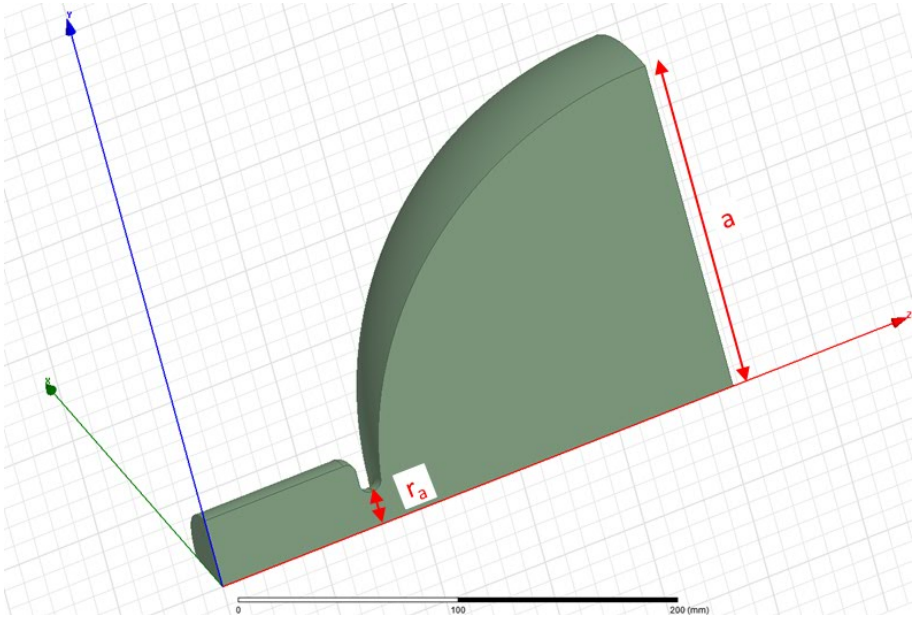

FIGURE 4.12: Sketch of the coupler

The radius of the aperture, r_a in Figure 4.12, is tuned to guarantee the desired coupling factor of 7.3. The radius of the spherical cavity, a, must be changed accordingly to compensate for the shift of the resonant frequency due to the presence of the coupling aperture.

The coupling factor and the resonant frequency can be easily found by making a frequency span and plotting the reflection at the waveguide port, $|s_{11}|$, versus the frequency. The minimum value of $|s_{11}|$ is located at the resonant frequency and its value defines the coupling factor β according to the formula:

$$\beta = \frac{1 + s_{11}}{1 - s_{11}} \tag{4.40}$$

It is important to observe that the coupling aperture to the spherical resonator is a very critical area for the system, since its small size can bring to electric and magnetic surface fields enhancement. To lower the field it was decided to increase the length of the neck, L_a in Figure 4.13, in order to introduce a radius of 20 mm between the coupling aperture and the sphere itself. This supplementary rounding helps to reduce the electric and the magnetic fields in that region.

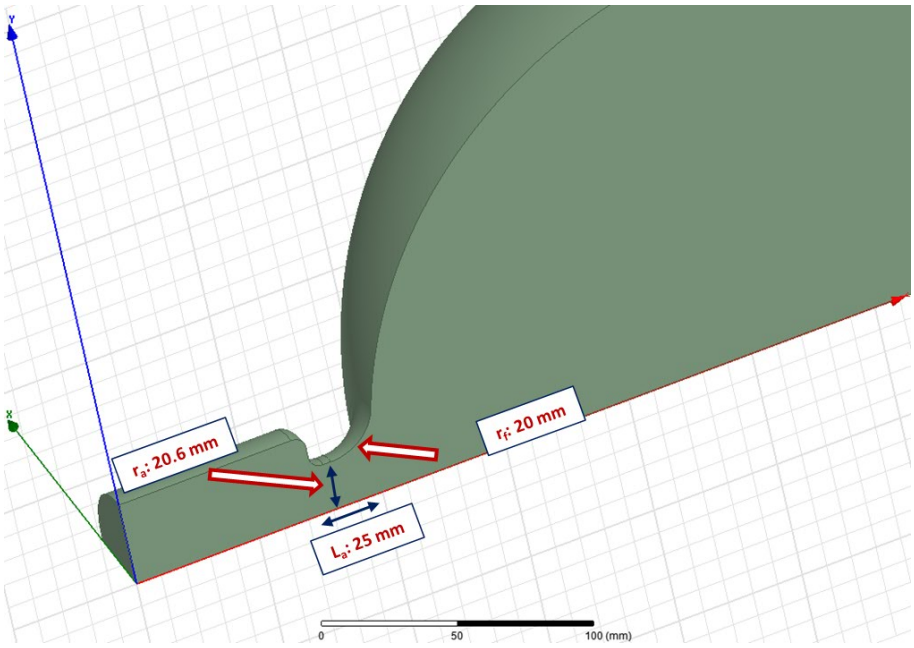

FIGURE 4.13: Sketch of the coupler with an increased length of the neck. A higher radius of 20 mm is used to connect the coupling aperture to the sphere itself in order to reduce the electric and magnetic surface fields

In Figure 4.14 the frequency sweep is shown, and the corresponding resonant frequency and coupling factor are reported: in particular, the resulting $|s_{11}|$ of -2.44 dB corresponds to a β of 7.1, quite close to the optimal target value.

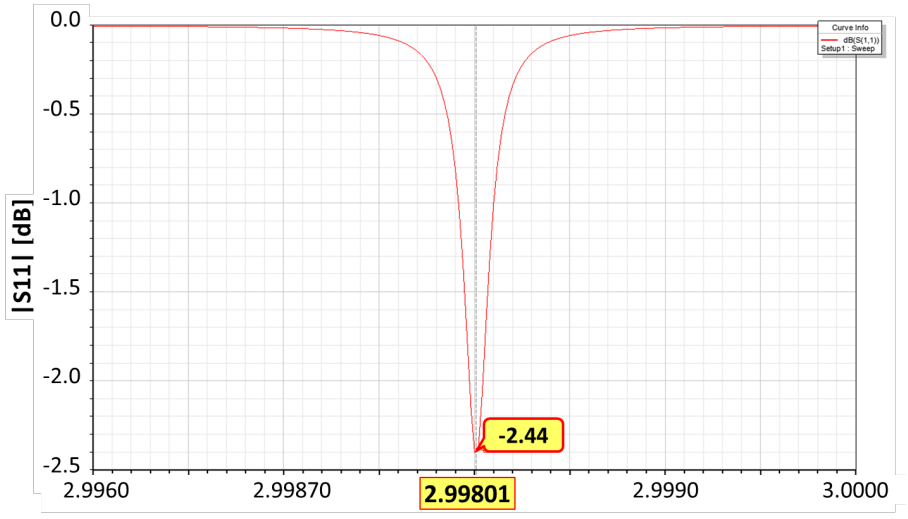

FIGURE 4.14: Plot of $|s_{11}|$ versus frequency. The resonant frequency and the coupling factor are highlighted

Figure 4.15 shows the surface electric field, the surface magnetic field and the value of the modified Poynting vector for 45 MW input power. As can be noticed, the value of the surface magnetic field across the coupling aperture is quite high ($162kA/m$) but, based on our actual experience with the BTW accelerating structure, it will still be reliable. However, further studies about pulse heating phenomena will be carried out and appropriate cooling channels will be designed to remove the heat generated.

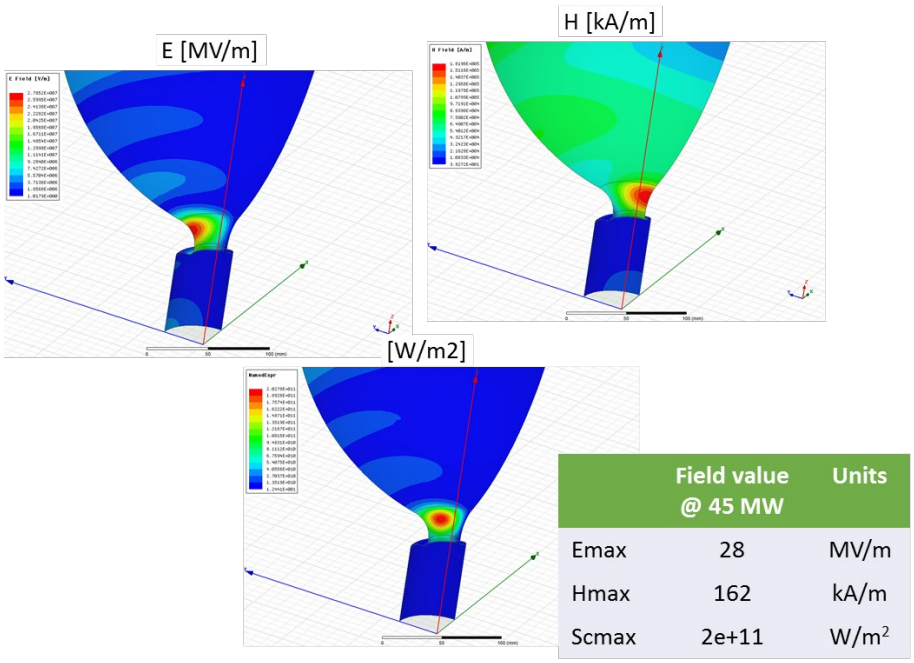

FIGURE 4.15: Surface electric field, magnetic field and modified Poynting vector for 45 MW input power

4.3.4.2 E-rotator

A compact, circular waveguide, TE_{11} rotating mode launcher (named *E-rotator* in the following) has been designed to excite the two orthogonal modes in the spherical resonant cavity. The starting point for designing the E-rotator is the 3-dB hybrid, shown in Figure 4.16, in which the input power, at port 1, is equally split between the two outgoing ports 3 and 4.

The E-rotator is obtained by short circuiting the forward branches and attaching a circular waveguide in the middle, as it is shown in Figure 4.17. The radius of the circular waveguide is set to 35.6 mm, the same value used for coupling to the spherical cavity.

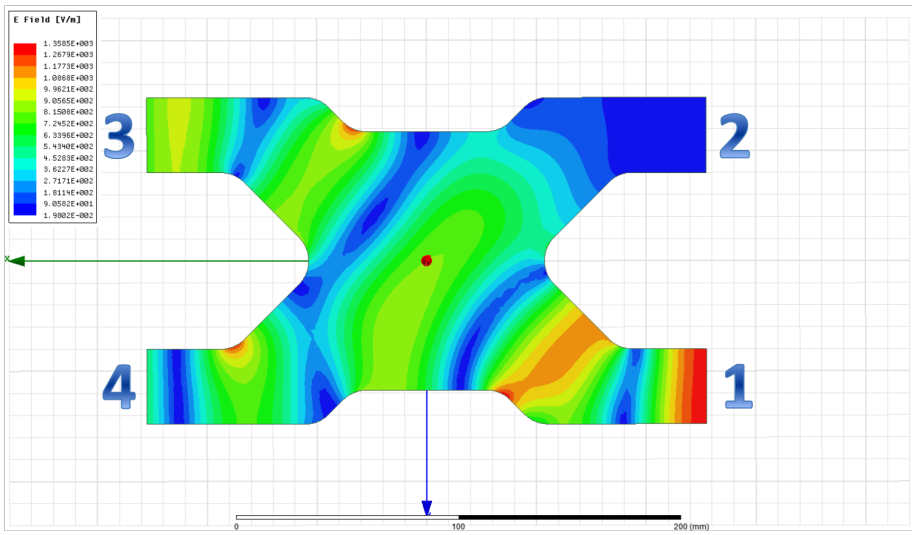

FIGURE 4.16: 3-dB hybrid geometry

Injecting the power from port 1 results in a circular polarized TE_{11} mode at port 3. Since the rotating mode in the port 3 is a superposition of two degenerate TE_{11} circular waveguide modes with vertical and horizontal polarization and 90 degree phase shift, from the simulation point of view the E-rotator can be considered as a 3 ports hybrid with a 4x4 S-matrix.

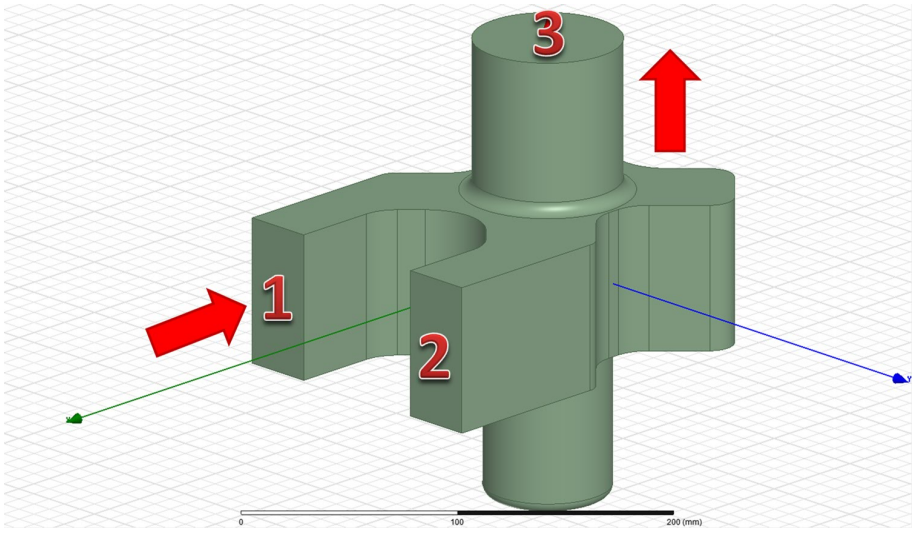

FIGURE 4.17: E-Rotator geometry

The optimization of such complex component has been performed using HFSS. More than ten geometric parameters have been carefully tuned to get the desired matching, an

optimal balance in the amplitude and a 90 degree phase shift between the two degenerate modes.

Since the optimization process was quite complex and time consuming, a special goal function, called *Conversion*, was introduced to use the semi-automatic optimization routine available in HFSS. The function *Conversion* was defined as [59]:

$$Conversion = |Re\{s_{13x}\} Im\{s_{13y}\} - Im\{s_{13x}\} Re\{s_{13y}\}| \tag{4.41}$$

where s_{13x} and s_{13y} are the s-parameters of the two degenerate modes. This goal function is equal to 0.5 in the case of an ideal E-rotator, for which three conditions are met:

$$|s_{13x}|^2 = 0.5 \tag{4.42a}$$

$$|s_{13y}|^2 = 0.5 \tag{4.42b}$$

$$|\angle s_{13y} - \angle s_{13x}| = \frac{\pi}{2} + n\pi \tag{4.42c}$$

RF parameters for the E-rotator are plotted in Figure 4.18 as a function of frequency. As it can be seen, at the resonant frequency f_0, the component has an extremely good matching with an s_{11} of $-51\ dB$ and a perfect balance between s_{13x} and s_{13y}, both equal to $-3.01\ dB$.

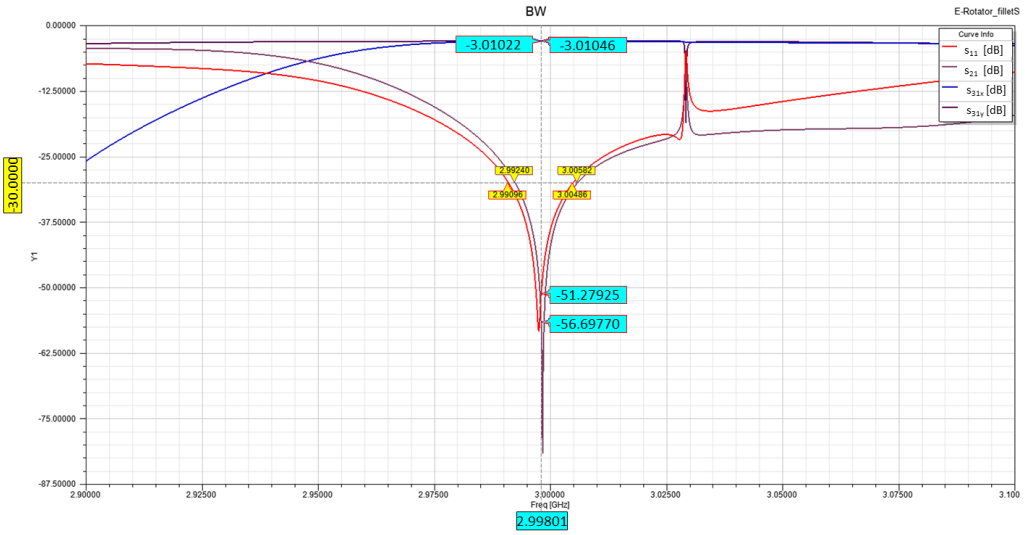

FIGURE 4.18: E-Rotator RF parameters

4.3.4.3 Spherical pulse compressor and sensitivity analysis

The E-rotator and the spherical resonant cavity can be connected together to get a high Q-factor, compact RF pulse compressor as illustrated in Figure 4.19.

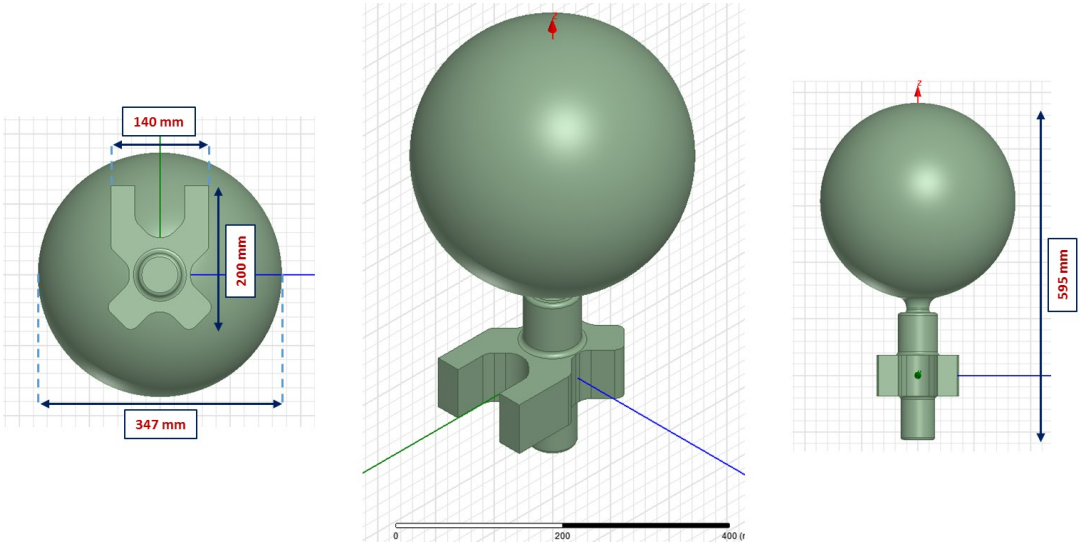

FIGURE 4.19: Geometry of the compact spherical pulse compressor

A high frequency simulation, with HFSS, was performed for the full assembly and the results, as functions of frequency, are plotted in Figure 4.20. The reflection parameter, $|s_{11}|$ is $-46\ dB$ at the nominal resonant frequency, $f_0 = 2998.01\ MHz$, while the transmission parameter $|s_{21}|$ is $-2.45\ dB$, corresponding to the desired coupling factor β. Furthermore, it is clear that there are no other resonant modes close to the nominal operating frequency: the first mode is in fact approximately $30\ MHz$ higher in frequency.

Since efficient pulse compression requires the cavity to be tuned exactly on frequency, before proceeding with the mechanical design it was necessary to analyze the frequency shift induced by mechanical errors in order to specify the required mechanical tolerances and the tuning system eventually needed.

Parametric analysis was performed varying the radius of the coupling aperture and the radius of the spherical cavity, in order to verify the impact of each parameter on the resonant frequency.

Mechanical errors in the range $\pm 10\ \mu m$ were considered and, for each value, a frequency sweep was performed. In Figure 4.22 the different resonant frequencies are plotted versus the error on the radius of the coupling aperture. As expected, the frequency shift is small,

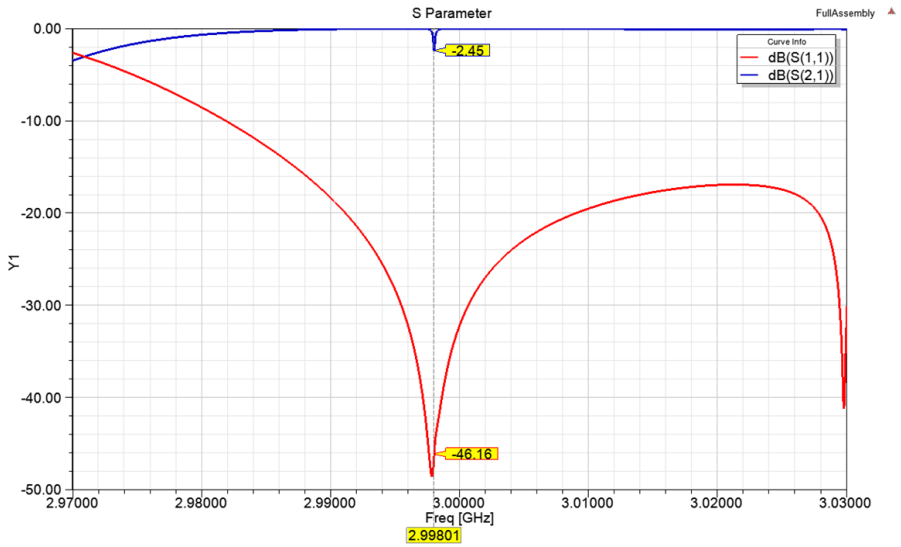

FIGURE 4.20: RF parameters for the compact spherical pulse compressor. The transmission parameter $s_{21} = -2.45\ dB$ corresponds to the optimal coupling factor β of 7.3

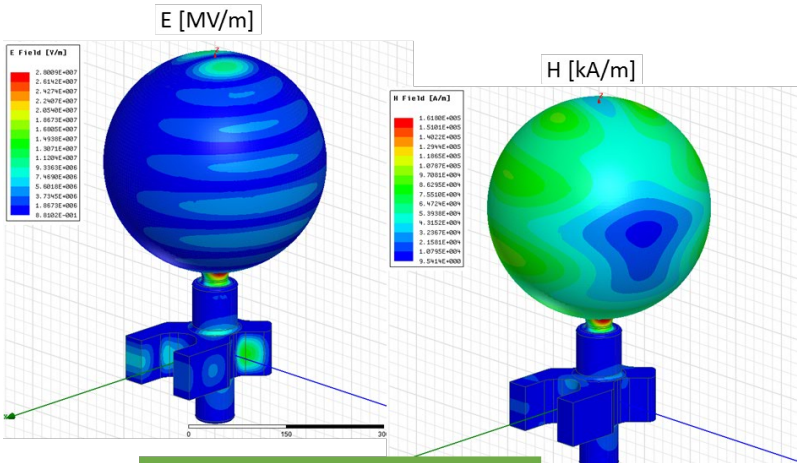

	Field value @ 45 MW	Units
Emax	28	MV/m
Hmax	162	kA/m
Scmax	2e+11	W/m^2

FIGURE 4.21: Electric and magnetic surface fields for the spherical pulse compressor

in the order of $-0.3\ kHz/\mu m$, so mechanical tolerances of $\pm 10\ \mu m$ will be sufficient to get the required performances.

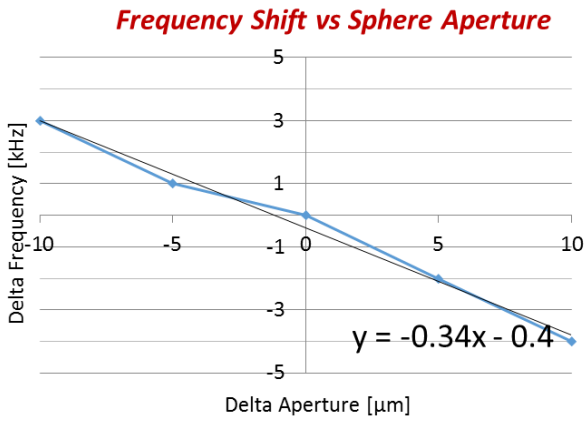

FIGURE 4.22: Resonant frequency shift of the spherical pulse compressor for different errors on the radius of the coupling aperture

While the impact of the coupling aperture on the pulse compressor resonant frequency is very limited, it was worth verifying the change in the coupling factor for the same mechanical errors. As it is evident from Figure 4.23, even this change is quite small so, if we define mechanical tolerances of $\pm 10\ \mu m$ on the radius of the coupling aperture, the RF performances of the pulse compressor will be preserved.

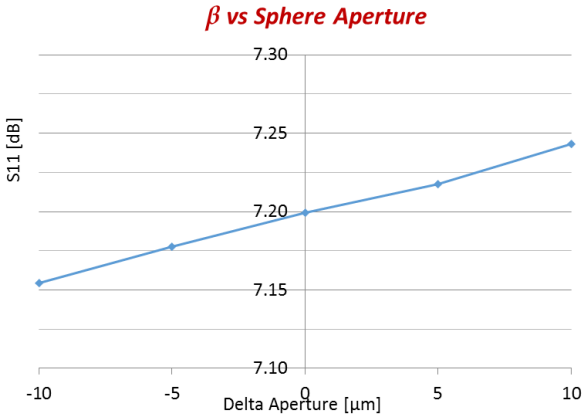

FIGURE 4.23: Coupling factor β as a function of the mechanical error in the radius of the coupling aperture

On the other side, as expected, the frequency shift for errors in the radius of the spherical cavity is in the order of $-17\ kHz/\mu m$ (see Figure 4.24).

Despite of this frequency shift, it was decided to not equip the pulse compressor with an embedded tuning system. Specifying a mechanical tolerance of $\pm 5\ \mu m$, the frequency

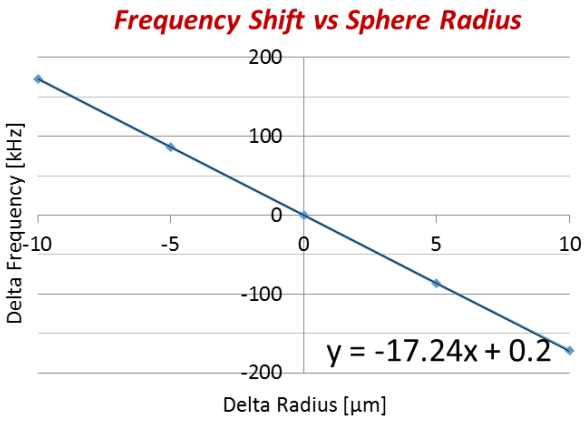

FIGURE 4.24: Resonant frequency shift of the spherical pulse compressor for different errors on the radius of the spherical cavity

shift will be limited to $\pm 85\ kHz$ and could be easily compensated by tuning the temperature of the cooling water. In fact, for an S-band cavity, the frequency detuning as a function of temperature is nearly $-50\ kHz/degree$. So, a cooling system with a fine temperature regulation in a range of $\pm 5\ \mathrm{deg}$ will guarantee the necessary tuning capability.

5 Conclusion

5.1 The FERMI Linac upgrade proposal

FERMI is the seeded Free Electron Laser (FEL), operating in the VUV to soft X-rays range, located at the Elettra laboratory in Trieste, Italy. Since FERMI has already demonstrated successful operation in the wavelength range from 100 nm down to 4 nm, an upgrade strategy to improve the FEL performances pushing towards shorter wavelengths is currently under evaluation.

As explained in Chapter 1, the fundamental wavelength emitted in a FEL is proportional to λ_u/γ^2, where λ_u is the undulator period, and γ the relativistic Lorentz factor, proportional to the electron beam energy. Based on this consideration, increasing the actual electron beam energy is essential for improving the FEL performances.

As shown in Figure 5.1, a possible solution could be that of replacing each of the seven backward-wave traveling structures (BTW), installed in the high energy part of the Linac, with a new accelerating module suitable for higher gradient operation. Given the RF power currently available, with the new modules a gradient of up to $30\ MV/m$ will be achievable and a final energy of $1.8\ GeV$ can be attainable.

A feasibility study, finalized to prove the reliability of operating at higher gradient, and with a final energy of nearly $1.8\ GeV$, has been started.

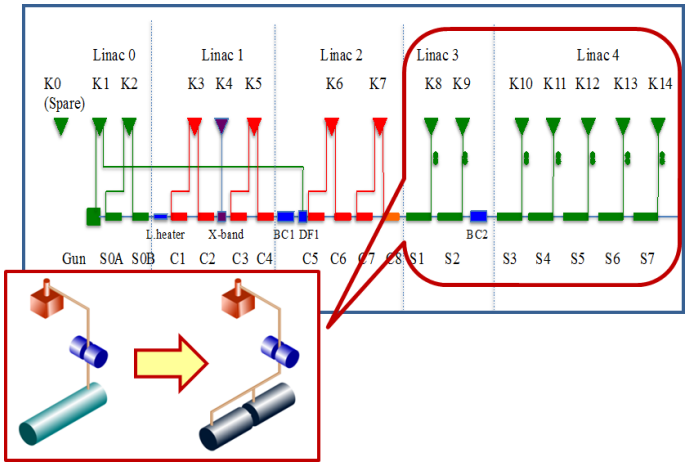

FIGURE 5.1: Proposed layout for the Linac upgrade

5.2 Novel accelerating structures and first prototype

Systematic studies, where the structure accelerating gradient was conditioned to the limit imposed by the rf breakdown and where relevant parameters were measured, can be widely found in literature [19].

For the gradient versus BDR dependence at a fixed pulse length, the exponential scaling law

$$\frac{E_a^{30}}{BDR} = const, \tag{5.1}$$

where E_a denotes the gradient at a fixed pulse length t_p, has been used extensively. It should be underlined that the choice of 30 for the power exponent is based on the analysis of the available experimental data only [19], and no assumption was made about the underlying physical mechanism.

Also, the dependence of the gradient on the pulse length at a fixed BDR has a well established scaling law [19] which has been observed in many experiments. The two laws can be combined into a single scaling law:

$$\frac{E_a^{30} t_p^5}{BDR} = const \tag{5.2}$$

Equation 5.2 states that, for a given structure, the ratio between the accelerating gradient, to the power of 30, and the BDR is a constant if the pulse length remains fixed. This

TABLE 5.1: Summary of RF parameters for both Electric Coupled and Magnetic Coupled RF couplers. All the field values are calculated for 65 MW of input power

	E_{surf} $[MV/m]$	H_{surf} $[kA/m]$	S_c $[MW/mm^2]$	BDR $[bpp/m]$	k_q $[V/ms]$	Pros	Cons
MC Couplers	93	175	0.7	$1E-15$	582	Lower residual quadrupole field components Acceleration efficiency	High magnetic field at the coupling slot
EC Couplers	81	78	0.57	$1E-16$	1973	Very low surface magnetic field Easy to machine Cost reduction	Higher residual quadrupole field components Sligthly reduced acceleration efficiency

means that increasing the structure accelerating gradient, the number of breakdown will increase accordingly.

As we have discussed in Chapter 1 and 2, the FERMI BTW structures present a high breakdown rate when operated at $24MV/m$. In order to get an electron beam energy of $1.8\ GeV$ at the end of the Linac, it would be sufficient to operate the last part of the Linac (i.e. the seven BTW structures) at a gradient of $30\ MV/m$. But, according to equation 5.2, this would increase the breakdown rate of a factor 800. Of course, this solution is neither reliable nor acceptable.

For the above mentioned reason, a new accelerating module, optimized for high gradient operation, was designed. Each accelerating module consists of two, 3 meter long, accelerating structures.

During the design phase particular care was devoted to the coupling cells, investigating and comparing two different solutions (ref. Chapter 2).

One way of coupling the power to the accelerator is, in fact, that of using iris apertures located between the end wall of the rectangular waveguides and the coupling cell. Such magnetic-coupled RF coupler (MC-coupler) presents high surface magnetic fields in the proximity of the coupling slots that can represent a bottleneck for high gradient operation. To overcome this limitation a different geometry was proposed using a direct electric coupling (EC-coupler) into a matching cell through a circular iris in the waveguide broad wall.

Table 5.1 summarizes and compares the performances of EC and MC couplers. The EC-coupler shows a lower value for the modified Pointing vector S_c and, consequently, a

lower breakdown rate. This coupler also shows a significant reduction of the magnetic surface fields and therefore no limitation will arise due to field enhancement or RF pulse heating effects. Based on these considerations, the electric-coupled solution was adopted.

For the accelerating structure a constant-gradient solution was adopted in order to maximize the accelerator energy gain while keeping surface electromagnetic fields to an acceptable level. Cells iris and disk thickness were carefully optimized to guarantee the required shunt impedance R_{sh} and the optimal filling time τ for efficient pulse compression (all relevant parameters are reported in Table 5.2). Furthermore, wakefields analysis and beam dynamics simulations were performed to study the impact of the upgrade on the quality of the beam. Results revealed that both longitudinal and transverse beam dynamics will clearly benefit from the upgrade, since bigger iris radii will mitigate the wakefields effects.

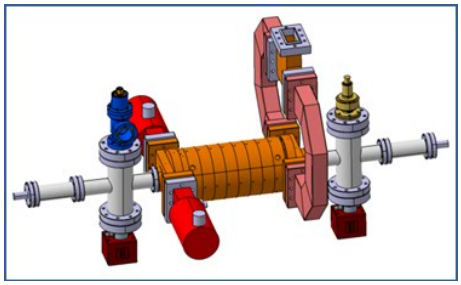

FIGURE 5.2: Mechanical design of the first, short prototype

Even if all the studies demonstrated the feasibility of operating at higher gradient, it was decided to build a first, short prototype to be high power tested in Trieste. For the construction of the prototype, a *Collaboration Agreement* was signed between Elettra and the Paul Scherrer Insitut (PSI), in Zurich, with the aim of consolidating the know-how developed for the construction of the SwissFEL Linac, and prove that the present technological processes can guarantee reliable operation even if high gradient are needed.

This prototype will be made of two EC-couplers, and seven regular cells for an overall length of approximately 0.5 meter. The raw material (Oxigen Free, High Conductivity copper) has been received and both couplers and cells are being machined. As for the SwissFEL structures, the prototype will be a *tuning-free* structure, so ultra high precision milling and turning will be performed since mechanical tolerances are very tight. The full prototype will be brazed at the PSI workshop in January and will be ready by February 2018.

5.3 Test Facility upgrade and prototype testing

In order to prove the reliability of operating the new accelerating structures at gradients up to $30\ MV/m$, it was decided to upgrade the existing FERMI Cavity Test Facility (CTF) making it facility suitable for very high power testing. The waveguide layout was completely modified and an RF pulse compressor (on loan from CERN) was installed in the line to increase the peak power available from the RF source.

For $30\ MV/m$ operation, a peak power of $65\ MW$ is required at the input of the accelerating structure. With the new CTF configuration, the input power could be up to $150\ MW$ and a gradient up to $50\ MV/m$ can be achieved. This will give us the chance to prove the reliability at the desired gradient, but also to push the system further to the limit imposed by the RF breakdown.

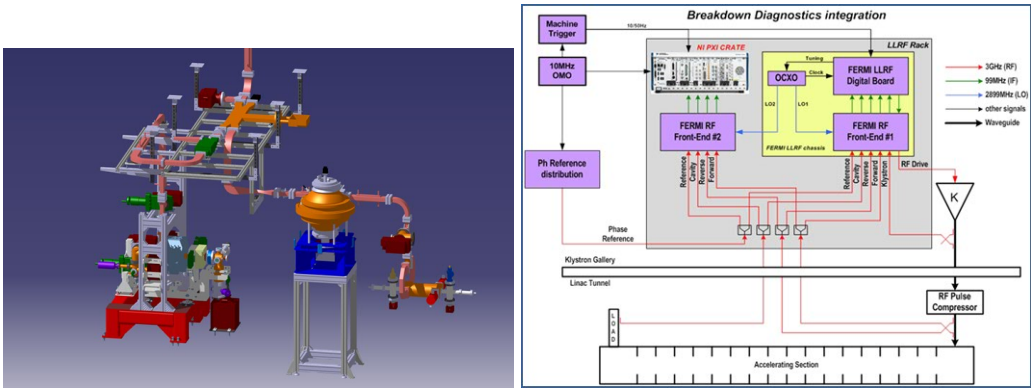

(a) (b)

FIGURE 5.3: Layout and LLRF of the FERMI Test Facility

Furthermore, for a better understanding of the high power RF conditioning and operation, the CTF is being equipped with a dedicated diagnostic for BDR measurement and breakdown localization. One important indicator of the health of a structure during operation is, in fact, the distribution of breakdowns along the length of the structure and, for a constant gradient structure, the breakdowns should be distributed evenly. The location of a breakdown in the structure can be pinpointed by looking at the time delays between the RF signals emanating from the structure during a breakdown [60]. The breakdown event causes a build-up of plasma in the structure which acts as a short circuit. This stops the transmitted wave and causes the reflected signal to increase to $70 - 90\%$ of the input power, as shown in Figure 5.5.

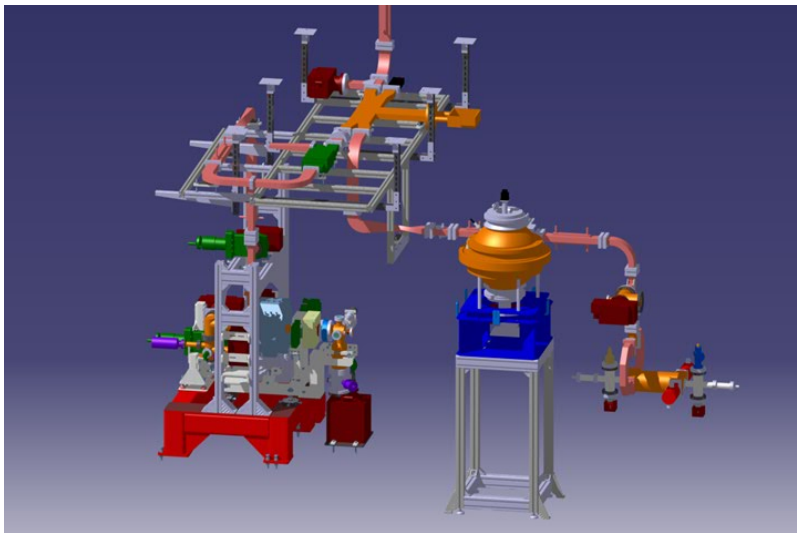

FIGURE 5.4: Layout of the FERMI Test Facility

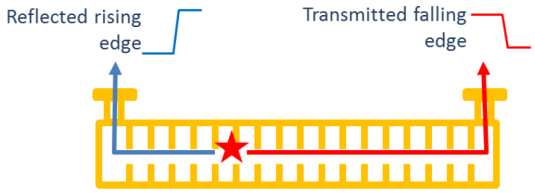

FIGURE 5.5: Diagram of a breakdown in the structure and the accompanying RF signals. The reflected signal is in blue and the transmitted signal is in red

National Instruments diagnostic hardware has been bought and is being integrated with the FERMI LLRF hardware as shown in Figure 5.4, and diagnostic software tools are being currently developed in collaboration with the CLIC (Compact LInear Collider) group at CERN.

In order to prove the feasibility of the proposed Linac upgrade plan, a budget of nearly 360.000 euro has been already allocated (a summary of the principal costs is reported in Figure 5.6). So far, the CTF is ready for high power operation while the first, short prototype will be delivered by PSI in February 2018. The prototype installation is currently scheduled in April 2018, during the long Easter shutdown and the high power testing will start on May 2018.

R&D BUDGET		
I - Prototype		
	1. Structure	€ 50,000
II - CTF		
	1. Waveguide System	€ 90,000
	2. Pulse Compressor	€ 70,000
	3. Vacuum System	€ 34,000
	4. Cooling System	€ 62,000
III - Diagnostic		
	1. National Instruments Hardware	€ 55,000
	TOTALE	**€ 361,000**

FIGURE 5.6: Budget for the first prototype and the CTF upgrade

TABLE 5.2: RF parameters of the accelerating structure

f_0	2998.01	MHz
$Mode$	$2\pi/3$	
$L_{structure}$	3175	mm
L_{cell}	33.332	mm
N_{cell}	90	
$a\ (iris)$	$11.38 \rightarrow 8.98$	mm
$b\ (cell\ outer\ radius)$	$41.61 \rightarrow 41.11$	mm
$t\ (disk\ thickness)$	2.5	mm
$or\ (outer\ bending\ radius)$	13	mm
R_{sh}	$71 \rightarrow 80$	$M\Omega/m$
Q_0	≈ 15850	
v_g/c	$2.21 \rightarrow 1.04$	
t_f	645	ns
τ	0.38	$Neper$

Bibliography

[1] J.M.J. Madey. "Stimulated emission of bremsstrahlung in a periodic magnetic field". In: *Journal of Applied Physics, 42, 1906* (1971).

[2] C. Pellegrini. "Progress toward a soft X-ray FEL". In: *Nuclear Instruments & Methods* A272 (1988), p. 364.

[3] C. Pellegrini and et al. "X-ray free-electron lasers - principles, properties and applications". In: *Nuclear Instruments & Methods* A500 (2003), p. 33.

[4] Brian W. J. McNeil and Neil R. Thompson. "X-ray free-electron lasers". In: *Nature Photonics* 4 (2010), p. 814.

[5] P. Schmuser and et al. *Free-Electron Lasers in the ultraviolet and X-ray regime*. Ed. by G. Hohler. ISBN 978-3-319-04080-6. Karlsruhe, Germany: Springer, 2014.

[6] *FERMI@Elettra Conceptual Design Report*. 2007.

[7] E. Allaria and et al. "Control of the Polarization of a Vacuum-Ultraviolet High-Gain Free-Electron-Laser". In: *Phs. Rev. X* 4.041040 (2014).

[8] C. Serpico and et al. "Design, manufacturing and installation of two dual-feed accelerating structures for the FERMI injector". In: *Proceedings of LINAC16*. East Lansing, USA, 2016.

[9] P. Girault. "The 3pi/4 Backward TW Structure for the ELETTRA 1.5 GeV Electron Injector". In: *Proc. of the Particle Accelerator Conference*. 1991, p. 3005.

[10] G. D'Auria and et al. *RF Measurements on the First BTW Section of the Trieste 2 Linac*. Technical Note. Sincrotrone Trieste, 1991.

[11] C. Nantista. *Radio-frequency pulse compression for Linear Accelerators*. SLAC-R-95-455. SLAC, 1995.

[12] C. Serpico and et al. "The Backward TW Structure for the FERMIELETTRA Linac". In: *Proceedings of PAC09*. Vancouver, Canada, 2009, p. 2042.

[13] C. Serpico and et al. "Phase-Modulation SLED Operation Mode at Elettra". In: *Proceedings of IPAC2011*. San Sebastian, Spain, 2011, p. 83.

[14] S. Orfanidis. *Electromagnetic Waves and Antennas*. ECE Department, Rutgers University, 2008.

[15] M. Weiss. *Introduction to RF linear acceleratators*. Tech. rep. CERN.

[16] F. Gerigk. *Cavity types*. Tech. rep. CERN.

[17] T. P. Wangler. *RF Linear Accelerator. 2nd, completely revised and enlarged edition*. Ed. by Wiley-VCH. 2008. ISBN: 978-3-527-40680-7.

[18] CLIC-Note-764. CERN, 2008.

[19] A. Grudiev and et al. "New local field quantity describing the high gradient limit of accelerating structures". In: *Physical Review Special Topics - Accelerators and Beams* 12, 102001 (2009).

[20] V. A. Dolgashev. "High magnetic fields in couplers of X-band accelerating structures". In: *Proc. of the Particle Accelerator Conference*. Vol. 2. 2003, p. 1267.

[21] V. A. Dolgashev and et al. *Effect of RF parameters on breakdown limits in high-vacuum x-band structures*. SLAC-PUB-10175. SLAC, 2003.

[22] S. Dobert and et al. *Coupler Studies for CLIC Accelerating Structures*. CLIC-Note-517. CERN, 2002.

[23] C. Nantista and et al. "Low-field accelerator structure couplers and design technique". In: *Physical Review Special Topics - Accelerators and Beams* 7, 072001 (2004).

[24] P. K. Ambattu and et al. "Coupler induced monopole component and its minimization in deflecting cavities". In: *Physical Review Special Topics - Accelerators and Beams* 16, 062001 (2013).

[25] L. Zenghai and et al. *On the importance of symmetrizing RF coupler fields for low emittance beams*. SLAC-PUB-14436. SLAC, 2011.

[26] A. Grudiev. "Radio frequency quadrupole for Landau damping in accelerators". In: *Physical Review Special Topics - Accelerators and Beams* 17, 011001 (2014).

[27] G. Barranco and et al. "Study of mutipolar RF kicks from the main deflecting mode in compact Crab cavities for LHC". In: *Proc. of IPAC2012*. New Orleans, Louisiana, 2012, p. 1873.

[28] C. Serpico and et al. "Analysis and comparison between electric and magnetic power couplers for accelerators in Free Electron Lasers (FEL)". In: *Nuclear Instruments and Methods in Physics Research A* 833 (2016), pp. 8–14.

[29] D. Alesini. *Power Coupling*. CERN Accelerator School. 2010.

[30] L. Xiao and et al. "Dual feed RF gun design for the LCLS". In: *Proc. of the Particle Accelerator Conference*. Knoxville, Tennessee, 2005, p. 3432.

[31] L. Zenghai and et al. "Coupler design for the LCLS injector S-band structures". In: *Contributed to the Particle Accelerator Conference*. Knoxville, Tennessee, 2005, p. 2176.

[32] *ANSYS HFSS, High Frequency Electromagnetic Field Simulation*. 2016.

[33] C. Serpico and et al. "High gradient, high reliability, and low wakefield accelerating structures for the FERMI FEL". In: *Review of Scientific Instruments* 88 (2017).

[34] R. B. Neal, ed. *The Stanford Two-mile Accelerator*. W.A. Benjamin, Inc., 1968.

[35] J.Y. Raguin and et al. "The Swiss FEL C-band Accelerating Structure: RF Design and Thermal Analysis". In: *Proceedings of LINAC12*. Tel-Aviv, Israel, 2012.

[36] *http://laacg.lanl.gov/*.

[37] B. W. Zotter and et al. *Impedances and Wakes in High-Energy Particle Accelerators*. Ed. by Bruno W. Zotter. World Scientific, 1998.

[38] L. Palumbo and et al. *Wake Fields and Impedance*. LNF-94/041. 1994.

[39] K. Bane and et al. "Wakefields and Wakefield Acceleration". In: *SLAC-PUB-3528*. 1984.

[40] *Gdfidl code, http://www.gdfidl.de/*.

[41] *ABCI Mannual, http://abci.kek.jp/*.

[42] *CST Code, http://www.cst.com*.

[43] E. Jensen. "Numerical Methods". In: *CERN Accelerator School*. 2010.

[44] O. Napoly and et al. "A Generalized Method for Calculating Wake Potentials". In: *Nuclear Instruments & Methods* A334 (1993), p. 255.

[45] A. Novokhatsk. "A New Green's Function for the Wake Potential Calculation for the Slac S-band Constant Gradient Accelerting Section". In: *SLAC-PUB-14536* (2011).

[46] *http://www.mathworks.com/*.

[47] N. Shafqat, C. Serpico, and et al. "Design study of high gradient, low impedance accelerating structures for the FERMI free electron laser linac upgrade". In: *Nuclear Instruments & Methods* A867 (2017), pp. 78–87.

[48] S. Dordevic. "Study of wake fields for short electron bunches using CST Particle Studio". In: *CST EUC*. 2013.

[49] M. Elashmawy and et al. *The short range wakefileds of the travelling wave and standing wave X-band linearixer of FERMI: a comparative Study*. Tech. rep. Sincrotrone Trieste, 2009.

[50] C. Serpico and et al. "Proc. of 28th Intern. LINAC Conf." In: *MOPLR004*. East lansing, MI, USA, 2016.

[51] P. Craievich and et al. "The short-range wakefields in the BTW accelerating structure of the ELETTRA LINAC". In: *Nucl. Instrum. Phys. Research A558 (2006) 58-61* (2006).

[52] A. W. Chao. *The Pysics of Collective Beam Instabilities in High Energy Accelerators*. Ed. by Mel Month. ISBN 0471551848. New York, NY, USA: John Wiley and Sons, Inc, 1993.

[53] T. O. Raubenheimer. "Estimates of emittance dilution and stability in high-energy linear accelerators". In: *Phs. Rev. Special Topics Accel. Beams 3, 121002 2000* (2000).

[54] S. Di Mitri and et al. "Merit function for the linac optics design for colliders and light sources". In: *Nucl. Instrum. Phys. Research A 735 (2014) 60-65* (2014).

[55] S. Di Mitri and et al. "Electron beam brightness in linac drivers for free-electron-lasers". In: *Phys. Reports* 539 (2014), pp. 1–48.

[56] C. Farkas and et al. "SLED: a method of doubling SLAC's energy". In: *presented at the 9th International Conference on High Energy Accelerators*. California, USA, 1974.

[57] Z. Li and et al. "RF design of a C-band compact spherical RF pulse compressor". In: *Nuclear Instruments & Methods* A863 (2017), pp. 7–14.

[58] S. Ramo and et al. *Fields and waves in communication electronics*. ISBN 0471871303. John Wiley & Sons, 1984.

[59] A. Grudiev. *Design of compact high power RF components at X-band*. CLIC-Note-1016. CERN, 2016.

[60] B. Woolley. *High Power X-band RF Test Stand Development and High Power Testing of the CLIC Crab Cavity*. 2015.